Title	Propagation of Optical Coherence and Interferometric Imaging
Author(s)	Arimoto, Hidenobu
Citation	大阪大学, 2000, 博士論文
Version Type	VoR
URL	https://doi.org/10.11501/3169442
rights	
Note	

Contents

Chapter 1

Introductory remarks

The spatial coherence of optical fields with a narrow spectral bandwidth such as a laser is ordinarily represented by the mutual coherence function in the space-time domain.[1] However, the spectral coherence function is indispensable when we discuss the spatial correlation of the fields with the wide spectral bandwidth. The correlation function of the Fourier spectra of the wavefields is called the cross-spectral density, and the spectral degree of coherence is defined as the normalized formula of the cross-spectral density. It was 1976 that E. Wolf and L. Mandel first proposed the concept of the spectral degree of coherence.[2]

One of the most interesting studies in which the spectral coherence plays a central role may be the correlation-induced spectral changes that are also known as the Wolf effect.[3] In 1986, E. Wolf pointed out that the spectrum of the light, which is propagating from the spatially, partially coherent source with the wide spectral bandwidth, can change depending upon the source correlation. Wolf also suggested that the spectrum is invariant through the propagation in the case where the spectral degree of coherence across the source obeys the Wolf's scaling law. It has long been known that the spectrum of the light changes because of the dispersive diffraction and the Doppler effect. However, the physics of the spectral changes which take place even if the light propagates through free space is indeed different from the dispersive diffraction or the Doppler effect. The age of the universe is estimated at twelve to fifteen billion years according to the latest study, and this value was mainly calculated from observed redshifts of the spectra of stellar objects. Therefore, much attention has been paid from an astrophysical point of view to the correlation-induced spectral changes, which imply the possibility of spectral change through the free propagation. However, it should be noted that the frequency does not shift in the Wolf effect unlike the frequency shift of a line spectrum seen in the Doppler effect.

Although many studies have been published since Wolf first pointed out this phenomenon,[4 – 9] most of the investigations are theoretical [3, 10 – 48] and the reports with the experimental verifications or the demonstrations are minor.[49 – 65] The main reason that makes laboratory experiments difficult may be hardness to separate two causes of the spectral changes, namely, the dispersive diffraction and the correlation-induced spectral changes. Nevertheless, experimental verification for the theoretical properties and establishing reliable techniques for these experiments are strongly required. Such experimental results and the reliable techniques will greatly help not only to justify the existing theoretical analyses but also to prompt the novel discoveries.

In contrast to the correlation-induced spectral changes that come from the problem of the forward propagation of the spatial coherence,[66 – 69] the interferometric imaging technique is based on the inverse propagation of the spatial coherence. The interferometric imaging techniques have long been used in practical measurements such as radio astronomy.[70] Although the resolving power of an ideal optical image-forming system is determined by ratio of a wavelength to an aperture size, inhomogeneities of the earth's atmosphere reduce the real resolving power. To overcome the effect of the earth's atmosphere, Fizeau first suggested in 1868 that Young's two-beam interference principle enabled one to measure the angular size of the stellar objects. The experiment for this idea was first conducted by Stephan. With the 1 m telescope of the Marseille Observatory, he succeeded in measuring the visibility of the interference fringes though the fringes were fluctuated owing to the turbulent atmosphere. Michelson also tried and succeeded in determining the angular diameter of a Jupiter's satellite.

One of the recent developments in the interferometric imaging technique was made by James.[71] James' technique is based on the new principle that is called the "space-frequency equivalence theorem" which was proposed by himself. The measurement system that uses this theorem enables us to determine the angular size of the source without changing the separation of the double aperture. The experimental demonstrations conducted by using the white light were reported by Kandpal.[72] The experimental results well agreed with the theory, and usefulness of this technique was confirmed. In the late 1990's, a principle of interferometric imaging for three-dimensional (3-D) source distribution was proposed by Rosen.[73 – 75] Their technique is based on the modified van Cittert-Zernike theorem. The experimental demonstration was also reported by themselves. Marks also presented their own principle for 3-D imaging in the latest publication.[76]

As stated above, there are increasing demands for 3-D imaging techniques. However, 3-D imaging techniques are still immature although 2-D imaging techniques have been sophisticated in both the theoretical analyses and the practical measurement systems. In other words, interferometric 3-D imaging is at the dawn. The methods recently proposed for 3-D imaging are based on the complex principles, and they need some fundamental restrictions for the state of the source correlation or locations of the sources because the basis of these new principles is originated from the van Cittert-Zernike theorem which holds for the spatial incoherent planer sources in the paraxial far field. As a result, new principles of interferometric 3-D imaging that can be applied under more general conditions are desired.

The fundamental concept through this work is the propagation of the spatial coherence. Although statistical optics which deals with the nature of the wave propagation in free space or scattering media has been considerably completed, there are much potentialities in the phenomena and the applications originated from or resting on these basic principles. From this background, the correlation-induced spectral changes and the interferometric imaging technique as the phenomenon and the application that are derived from the forward and the inverse propagation of the spatial coherence are studied theoretically and experimentally in this work. Studies on the correlation-induced spectral changes are devoted mainly on the experimental verification and the establishment of the reliable measurement method. Studies on the interferometric imaging techniques are, on the other hand, mainly on the proposal of new principles and concepts such as the 3-D imaging or the detection of the incoherent sources. Contents of chapters are listed with brief summaries in the followings.

In Chapter 2, the fundamental concepts of the second-order spatial coherence are reviewed. Definitions of the spatial coherence functions that are described in the space-time domain and the space-frequency domain, and their propagation law are introduced. The phenomenon of the correlation-induced spectral changes is also brought up.

In Chapter 3, the correlation-induced spectral changes are studied theoretically and experimentally. First, an experimental analysis of the spectral changes caused by the source correlation and the dispersive diffraction is presented. The spectral changes in a Gaussian-like spectrum that depend on ratio of the coherence area to the source area are investigated. Next, the spectral changes which are caused by only the source correlation are investigated. It is proven that the wavefront folding image-forming system is considerably reliable for observing the spectral changes released from the dispersive diffraction. Redshifts and blueshifts of the spectrum are experimentally observed depending on the source correlation and the observing location.

In Chapter 4, new principles for determining the two-dimensional source image are presented. One is a technique to determine not only the angular separation of two point sources but also their spectral profiles. The principle is based on measuring both the spectral degree of coherence and the uniform spectra across an observation area. The theoretical predictions are proven by an experimental demonstration with uncorrelated two point sources. The other one is for retrieving the cross-spectral density propagating in free space. The principle of the technique is based on the propagation law of the angular spectrum. Since this law holds without the paraxial approximation, the cross-spectral density across the off-axis reference plane can be retrieved. Results of an experiment demonstrating the retrieval of the cross-spectral density across any reference plane are also presented.

In Chapter 5, a novel interferometric 3-D imaging technique based on retrieving the sequential cross-spectral densities is presented. It is shown that the cross-spectral density propagating from the source enables us to retrieve the information of the second-order spatial coherence conveyed through the 3-D space. In addition to the 3-D imaging principle, a new concept to detect the spatially incoherent sources is presented. These principles make it possible to know the state of the spatial coherence across an arbitrary transverse plane and to find the incoherent sources even in the high background intensity. Full mathematical description and the analysis of the point spread function are also given.

In Chapter 6, an interferometric 3-D imaging technique that is based on retrieving the spatial distribution of the generalized radiance function is proposed. Although the technique that is presented in Chapter 5 requires the four-dimensional Fourier transform in the 3-D image retrieval, this imaging principle with the generalized radiance function enables us to retrieve the 3-D information by the two-dimensional Fourier transform. Consequently, the data processing time is much reduced. The point spread function of the system is derived and the spatial resolution is discussed.

In Chapter 7, noise-limitations of the interferometric imaging system described in Chapter 4 are studied in two limiting cases, namely the photon-noise-limit and the detector-noise-limit cases. The signal-to-noise ratio is theoretically derived and an experiments are conducted. The noise statistics obtained from the experimental results agree with the theoretical expectations.

In Chapter 8, concluding remarks about the entire dissertation are given.

Chapter 2

Introduction to second-order spatial coherence in scalar wavefields

2.1 Introduction

In this chapter, the definitions of the spatial coherence functions described in the space-time domain and the space-frequency domain are reviewed. The correlation of optical wavefields is closely related to the interference effects. The visibility of the interference fringe is determined by the modulus of the complex degree of coherence. When we discuss the correlation in the wavefields with the wide spectral bandwidth, the concept of the spectral coherence plays an important role. The efficiency of the spectral interference is determined by the spectral degree of coherence in a similar way as the spatial interference fringes.

The phenomenon of the spectral change owing to the source correlation, that is so called the correlation-induced spectral changes, has been actively studied since the 1980's. Studies on the correlation-induced spectral changes from both the theoretical and experimental points of view were reported. The basic concept of the correlation-induced spectral changes and the condition for the spectral invariance that was derived by Wolf[3] is briefly reviewed in the followings.

2.2 Second-order spatial coherence

First, let us consider the analytic signal $V(\boldsymbol{r}_1;t)$ and $V(\boldsymbol{r}_2;t)$ that fluctuate with time t at different two points $\boldsymbol{r}_1$ and $\boldsymbol{r}_2$, and the field is assumed to be stationary. Their cross-correlation function is defined by

$$\Gamma(\boldsymbol{r}_1,\boldsymbol{r}_2;\tau) = \langle V^*(\boldsymbol{r}_1;t)V(\boldsymbol{r}_2;t+\tau)\rangle \ , \tag{2.1}$$

where the angular bracket denotes the ensemble average, the asterisk denotes the complex conjugate, and τ is the time difference. This cross-correlation function is called the mutual coherence function in statistical optics. The mutual coherence function with $\tau = 0$ is named as the mutual intensity, and the definition is

$$J(\boldsymbol{r}_1,\boldsymbol{r}_2) = \Gamma(\boldsymbol{r}_1,\boldsymbol{r}_2,0). \tag{2.2}$$

The complex degree of coherence is defined as the normalized mutual coherence:

$$\gamma(\boldsymbol{r}_1,\boldsymbol{r}_2,\tau) = \frac{\Gamma(\boldsymbol{r}_1,\boldsymbol{r}_2;\tau)}{\sqrt{I(\boldsymbol{r}_1)I(\boldsymbol{r}_2)}} \ , \tag{2.3}$$

where

$$I(\boldsymbol{r}_j) = \Gamma(\boldsymbol{r}_j,\boldsymbol{r}_j;0) \ , \quad (j = 1 \text{ or } 2) \ . \tag{2.4}$$

The complex degree of coherence, which is defined by Eq. (2.3), is related to the visibility of the spatial interference fringes that appear in the two-beam interference of the light from $\boldsymbol{r}_1$ and $\boldsymbol{r}_2$. The relationship between the complex degree of coherence and the visibility V is represented by

$$V = \frac{I_{\max}(\boldsymbol{\rho}) - I_{\min}(\boldsymbol{\rho})}{I_{\max}(\boldsymbol{\rho}) + I_{\min}(\boldsymbol{\rho})} = |\gamma(\boldsymbol{r}_1,\boldsymbol{r}_2;\tau)| \ , \tag{2.5}$$

where $I_{\max}(\boldsymbol{\rho})$ and $I_{\min}(\boldsymbol{\rho})$ are the maximum and the minimum intensities that are seen around $\boldsymbol{\rho}$. While the modulus of the complex degree of coherence represents the visibility of the interference fringes, the argument of the complex degree of coherence is related to the location of the interference fringes. The complex degree of coherence describes the spatial correlation of the quasi-monochromatic wavefields in the space-time domain. On the other hand, the dependence of the correlation property on the optical frequency is essential in the case where the spectral bandwidth of the wavefields is broad. The cross-spectral density and the spectral degree of coherence play a critical role in this case.

The analytic signal $V(\boldsymbol{r};t)$ at $\boldsymbol{r}$ is a scalar variable if we consider one of the orthogonal components, and the analytic signal and the Fourier spectrum $U(\boldsymbol{r};\nu)$ that represents a particular frequency component are related by the Fourier transform pair:

$$V(\boldsymbol{r};t) = \int_0^{\infty} U(\boldsymbol{r};\nu)\exp(-2\pi i\nu t)d\nu\ , \tag{2.6}$$

and

$$U(\boldsymbol{r};\nu) = \int_{-\infty}^{\infty} V(\boldsymbol{r};t)\exp(2\pi i\nu t)dt\ . \tag{2.7}$$

Let us consider the ensemble average of the product of two Fourier spectra with different frequencies at two points $\boldsymbol{r}_1$ and $\boldsymbol{r}_2$:

$$\begin{aligned}&\langle U^*(\boldsymbol{r}_1;\nu)U(\boldsymbol{r}_2;\nu')\rangle\\&\quad= \iint_{-\infty}^{\infty}\langle V^*(\boldsymbol{r}_1;t)V(\boldsymbol{r}_2;t')\rangle\exp[2\pi i(\nu't'-\nu t)]dtdt'\\&\quad= \iint_{-\infty}^{\infty}\langle V^*(\boldsymbol{r}_1;t)V(\boldsymbol{r}_2;t+\tau)\rangle\exp[2\pi i(\nu'-\nu)t]\exp(2\pi i\nu'\tau)dtd\tau\ ,\end{aligned} \tag{2.8}$$

where $\tau = t'-t$. Substitution of Eq. (2.1) into Eq. (2.8) gives

$$\langle U^*(\boldsymbol{r}_1;\nu)U(\boldsymbol{r}_2;\nu')\rangle = W(\boldsymbol{r}_1,\boldsymbol{r}_2;\nu)\delta(\nu-\nu')\ , \tag{2.9}$$

where $W(\boldsymbol{r}_1, \boldsymbol{r}_2; \nu)$ is the cross-spectral density. The mutual coherence function and the cross-spectral density are also related by the Fourier transform pair:

$$W(\boldsymbol{r}_1, \boldsymbol{r}_2; \nu) = \int_{-\infty}^{\infty} \Gamma(\boldsymbol{r}_1, \boldsymbol{r}_2; \tau) \exp(2\pi i \nu \tau) d\tau \ , \tag{2.10}$$

and

$$\Gamma(\boldsymbol{r}_1, \boldsymbol{r}_2; \tau) = \int_{0}^{\infty} W(\boldsymbol{r}_1, \boldsymbol{r}_2; \nu) \exp(-2\pi i \nu \tau) d\nu \ . \tag{2.11}$$

Note that Eq. (2.9) implies that the Fourier spectra at different frequencies ν and ν' are uncorrelated. Therefore, the cross-spectral density represents the spatial correlation of the wavefields at a particular frequency.

As stated above, the complex degree of coherence is defined as the normalized mutual coherence function. The normalization of the cross-spectral density defines the spectral degree of coherence in a similar way:

$$\mu(\boldsymbol{r}_1, \boldsymbol{r}_2; \nu) = \frac{W(\boldsymbol{r}_1, \boldsymbol{r}_2; \nu)}{\sqrt{W(\boldsymbol{r}_1, \boldsymbol{r}_1; \nu) W(\boldsymbol{r}_2, \boldsymbol{r}_2; \nu)}} \ . \tag{2.12}$$

The modulus of the spectral degree of coherence is limited to the range $[0, 1]$, namely

$$0 \leq |\mu(\boldsymbol{r}_1, \boldsymbol{r}_2; \nu)| \leq 1 \ . \tag{2.13}$$

The modulus of the complex degree of coherence represents the visibility of the spatial interference fringes, and on the other hand the modulus of the spectral degree of coherence represents the interference efficiency of the spectral interference.

As described in Eqs. (2.10) and (2.11), the mutual coherence function and the cross-spectral density are related by the Fourier transform relationship. However, the relationship between their normalization forms, namely the complex degree of coherence and the spectral degree of coherence, is more complicated. Now, let us define the Fourier transform of the complex degree of coherence by

$$\beta(\boldsymbol{r}_1, \boldsymbol{r}_2; \nu) = \int_{-\infty}^{\infty} \gamma(\boldsymbol{r}_1, \boldsymbol{r}_2; \tau) \exp(2\pi i \nu \tau) d\tau \ . \tag{2.14}$$

As is obvious from Eq. (2.3), the representation of $\beta(\boldsymbol{r}_1, \boldsymbol{r}_2; \nu)$ with the cross-spectral density is

$$\beta(\boldsymbol{r}_1, \boldsymbol{r}_2; \nu) = \frac{W(\boldsymbol{r}_1, \boldsymbol{r}_2; \nu)}{\sqrt{I_1(\boldsymbol{r}_1) I_2(\boldsymbol{r}_2)}} \,. \tag{2.15}$$

Equation (2.15) can be rewritten when $\boldsymbol{r}_1 = \boldsymbol{r}_2$ as

$$\beta(\boldsymbol{r}_1, \boldsymbol{r}_1; \nu) = \frac{W(\boldsymbol{r}_1, \boldsymbol{r}_1; \nu)}{I(\boldsymbol{r})} \,, \tag{2.16}$$

and $I(\boldsymbol{r})$ can be also expressed by

$$I(\boldsymbol{r}) = \Gamma(\boldsymbol{r}, \boldsymbol{r}; 0) = \int_0^\infty W(\boldsymbol{r}, \boldsymbol{r}, \nu) d\nu \,. \tag{2.17}$$

Then the following equation holds:

$$\int_0^\infty \beta(\boldsymbol{r}_1, \boldsymbol{r}_2; \nu) d\nu = 1 \,. \tag{2.18}$$

Equations (2.12), (2.15), and (2.16) gives the representation of the spectral degree of coherence with $\beta(\boldsymbol{r}, \boldsymbol{r}; \nu)$ as

$$\mu(\boldsymbol{r}_1, \boldsymbol{r}_2; \nu) = \frac{\beta(\boldsymbol{r}_1, \boldsymbol{r}_2; \nu)}{\sqrt{\beta(\boldsymbol{r}_1, \boldsymbol{r}_1; \nu) \beta(\boldsymbol{r}_2, \boldsymbol{r}_2; \nu)}} \,. \tag{2.19}$$

Equation (2.19) means that the complex degree of coherence and the spectral degree of coherence are not related by the Fourier transform pair unlike the relationship between the mutual coherence function and the cross-spectral density.

2.3 Propagation of spectral coherence function

2.3.1 Van Cittert-Zernike theorem in space-frequency domain

The van Cittert-Zernike theorem describes the spatial coherence function that propagates from the spatially incoherent planer source. The optical system is shown in

Fig. 2.1. The mutual coherence function at the two points Q_1 and Q_2 on the observation plane is given by

$$J(Q_1, Q_2) = \left(\frac{\bar{\nu}}{cz}\right)^2 \exp(-i\psi) \iint_{-\infty}^{\infty} I_P(\boldsymbol{r}) \exp\left[\frac{2\pi i\bar{\nu}}{cz}(\boldsymbol{\rho}_1 - \boldsymbol{\rho}_2) \cdot \boldsymbol{r}\right] dr \,, \tag{2.20}$$

where $\bar{\nu}$ is the central frequency of the quasi-monochromatic source, $\psi = \pi\bar{\nu}(\rho_1^2 - \rho_2^2)$,

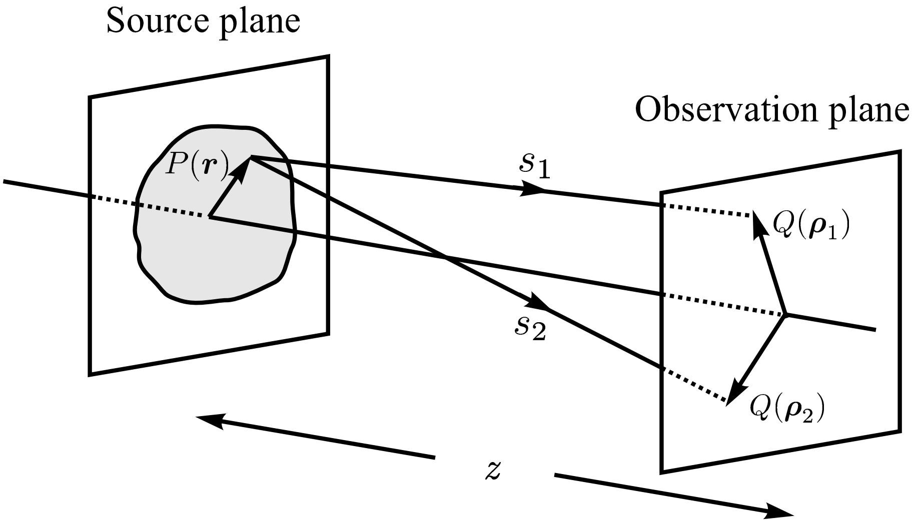

Fig. 2.1. Optical system considered.

and $I_P(\boldsymbol{r})$ is the intensity at $P(\boldsymbol{r})$ on the source plane. In this subsection, let us consider the relationship between the spectral density distribution and the spectral coherence in the paraxial far field. The paraxial far field implies the approximation $s_l \simeq z + |\boldsymbol{r} \cdot \boldsymbol{\rho}_l|/z$ $(l = 1, 2)$.[77]

With reference to Fig. 2.1, we assume that the spectrum of the source is broad, the spectral profile $S_P(\boldsymbol{r};\nu)$ depends on the position of the source plane, and the observation plane is located in the far field. The analytic signals $V_P(\boldsymbol{r};t)$ and $V_Q(\boldsymbol{\rho};t)$ at the source plane and the observation plane are expressed by the Fourier integral

$$V_P(\boldsymbol{r};t) = \int_0^{\infty} U_P(\boldsymbol{r};\nu) \exp(-2\pi i\nu t) d\nu \,, \tag{2.21}$$

$$V_Q(\boldsymbol{\rho};t) = \int_0^\infty U_Q(\boldsymbol{\rho};\nu)\exp(-2\pi i\nu t)d\nu\ . \tag{2.22}$$

By using the impulse response $h(\boldsymbol{r},\boldsymbol{\rho};t)$ from $P(\boldsymbol{r})$ to $Q(\boldsymbol{\rho})$, the analytic signal at $Q(\boldsymbol{\rho})$ is represented by the convolution integral

$$V_Q(\boldsymbol{\rho};t) = \iint_{-\infty}^{\infty} d^2r \int_{-\infty}^{\infty} h(\boldsymbol{r},\boldsymbol{\rho};t-t')V_P(\boldsymbol{\rho};t')dt'\ . \tag{2.23}$$

By introducing the transmission function $H(\boldsymbol{r},\boldsymbol{\rho};\nu)$ in the space-frequency domain, $h(\boldsymbol{r},\boldsymbol{\rho};t)$ and $H(\boldsymbol{r},\boldsymbol{\rho};\nu)$ are related by the Fourier transform relationship:

$$h(\boldsymbol{r},\boldsymbol{\rho};t) = \int_0^\infty H(\boldsymbol{r},\boldsymbol{\rho};\nu)\exp(-2\pi i\nu t)d\nu\ . \tag{2.24}$$

Under the paraxial approximation, $H(\boldsymbol{r},\boldsymbol{\rho};\nu)$ can be represented by

$$H(\boldsymbol{r},\boldsymbol{\rho};\nu) = -\frac{i\nu}{cs_l}\exp\left(\frac{2\pi i\nu s_l}{c}\right) \qquad (l=1,2)\ . \tag{2.25}$$

Substituting Eqs. (2.21) and (2.24) into Eq. (2.23) gives

$$V_Q(\boldsymbol{\rho};t) = \iint_{-\infty}^{\infty} d^2r \int_0^\infty H(\boldsymbol{r},\boldsymbol{\rho};\nu)U_P(\boldsymbol{r};\nu)\exp(-2\pi i\nu t)d\nu\ . \tag{2.26}$$

Next, let us consider the mutual coherence function defined by

$$\Gamma_Q(\boldsymbol{\rho}_1,\boldsymbol{\rho}_2;\tau) = \langle V_Q^*(\boldsymbol{\rho};t)V_Q(\boldsymbol{\rho}_2;t+\tau)\rangle\ . \tag{2.27}$$

By using Eq. (2.26) and the cross-spectral density across the source plane

$$W_P(\boldsymbol{r}',\boldsymbol{r};\nu) = \langle U_P^*(\boldsymbol{r}',\nu)U_P(\boldsymbol{r};\nu)\rangle\ , \tag{2.28}$$

we obtain

$$\begin{aligned}\Gamma_Q(\boldsymbol{\rho}_1,\boldsymbol{\rho}_2;\tau) \qquad &= \iiiint_{-\infty}^{\infty} d^2r d^2r' \\ \times \int_0^\infty W_P(\boldsymbol{r}',\boldsymbol{r};\nu)&H^*(\boldsymbol{r}',\boldsymbol{\rho}_1;\nu)H(\boldsymbol{r},\boldsymbol{\rho}_2;\nu)\exp(-2\pi i\nu\tau)d\nu\ . \end{aligned} \tag{2.29}$$

Note that Eq. (2.29) holds without any restriction on the source correlation. Let us then consider the spatially incoherent source in the following. The cross-spectral density is thus represented by using the spectral density of the source:

$$W_P(\boldsymbol{r}', \boldsymbol{r}; \nu) = S_P(\boldsymbol{r}; \nu)\delta(\boldsymbol{r} - \boldsymbol{r}') \, . \tag{2.30}$$

Substituting Eq. (2.30) into Eq. (2.29) gives

$$\Gamma_Q(\boldsymbol{\rho}_1, \boldsymbol{\rho}_2; \tau) = \iint_{-\infty}^{\infty} d^2r \int_0^{\infty} S_P(\boldsymbol{r}; \nu) H^*(\boldsymbol{r}, \boldsymbol{\rho}_1; \nu) H(\boldsymbol{r}', \boldsymbol{\rho}_2; \nu) \exp(-2\pi i \nu \tau) d\nu \, . \tag{2.31}$$

Then we obtain the mutual intensity across the observation plane by substituting $\tau = 0$ into Eq. (2.31) as

$$J_Q(\boldsymbol{\rho}_1, \boldsymbol{\rho}_2) = \iint_{-\infty}^{\infty} d^2r \int_0^{\infty} S_P(\boldsymbol{r}; \nu) H^*(\boldsymbol{r}, \boldsymbol{\rho}_1; \nu) H(\boldsymbol{r}', \boldsymbol{\rho}_2; \nu) d\nu \, . \tag{2.32}$$

Under the paraxial approximation with respect to the propagation distances s_1 and s_2 (see Fig. 2.1), namely,

$$s_1 - s_2 = \frac{\boldsymbol{\rho}_1^2 - \boldsymbol{\rho}_2^2}{2z} - \frac{(\boldsymbol{\rho}_1 - \boldsymbol{\rho}_2) \cdot \boldsymbol{r}}{z} \, , \tag{2.33}$$

substituting Eq. (2.25) into Eq. (2.32) gives

$$\begin{aligned} J_Q(Q_1, Q_2) &= \left(\frac{1}{cz}\right)^2 \iint_{-\infty}^{\infty} d^2r \int_0^{\infty} \nu^2 S_P(\boldsymbol{r}; \nu) \\ &\quad \times \exp\left[\frac{-i\pi\nu(\boldsymbol{\rho}_1^2 - \boldsymbol{\rho}_2^2)}{cz}\right] \exp\left[\frac{2\pi i \nu (\boldsymbol{\rho}_1 - \boldsymbol{\rho}_2) \cdot \boldsymbol{r}}{cz}\right] d\nu \, . \end{aligned} \tag{2.34}$$

Equation (2.34) holds for the mutual intensity of the wavefields that propagates from the source with an arbitrary spectral profile.

Next, let us consider the propagation of the cross-spectral density. The Fourier transform of Eq. (2.29) with respect to τ and Eq. (2.25) give the following equation:

$$W_Q(\boldsymbol{\rho}_1, \boldsymbol{\rho}_2; \nu) = \left(\frac{\nu}{cz}\right)^2 \iiiint_{-\infty}^{\infty} W_P(\boldsymbol{r}', \boldsymbol{r}; \nu) \exp\left[\frac{2\pi i \nu (s_1 - s_2)}{c}\right] d^2r d^2r' \, . \tag{2.35}$$

Since we assume that the source is spatially incoherent, substituting Eq. (2.30) into Eq. (2.35) gives

$$W_Q(\boldsymbol{\rho}_1, \boldsymbol{\rho}_2; \nu) = \left(\frac{\nu}{cz}\right)^2 \exp(-i\psi) \iint_{-\infty}^{\infty} S_P(\boldsymbol{r}; \nu) \exp\left[\frac{2\pi i\nu(\boldsymbol{\rho}_1 - \boldsymbol{\rho}_2) \cdot \boldsymbol{r}}{cz}\right] d^2r \, . \tag{2.36}$$

Equation (2.36) implies that the cross-spectral density at the far field is given by the two-dimensional Fourier transform of the spectral density across the spatially incoherent source. It should be noted that this relationship corresponds to the van Cittert-Zernike theorem described by Eq. (2.20).

2.3.2 Propagation of cross-spectral density

In this subsection, let us review the propagation law of the angular spectrum and the four-dimensional Fourier transform of the cross-spectral density. With reference to Fig. 2.2, we assume a planar, quasi-monochromatic light source on a source plane Σ_s at $z = 0$ and a wavefield propagating toward the right of the figure in free space. A reference plane Σ_r is located at $z = z_r$ parallel to Σ_s. Let a particular point P at a reference plane be specified by a three-dimensional position vector $\boldsymbol{r} = (x, y, z)$. The origin of the coordinate system is set on Σ_s.

For the wavefield propagation, the spectral amplitude $U(\boldsymbol{r}; \nu)$ at a particular point on Σ_r satisfies the Helmholtz equation

$$(\nabla^2 + k^2)U(\boldsymbol{r}; \nu) = 0 \, , \tag{2.37}$$

where $k = 2\pi\nu/c$ and c is the speed of light in free space. Since the z coordinate can be regarded as a parameter that expresses the location of each plane, we rewrite $\boldsymbol{r} = (\boldsymbol{r}_\perp, z)$. Thus the wavefield at Σ_r is also rewritten as $U(\boldsymbol{r}_\perp, z_r; \nu)$. At any location,

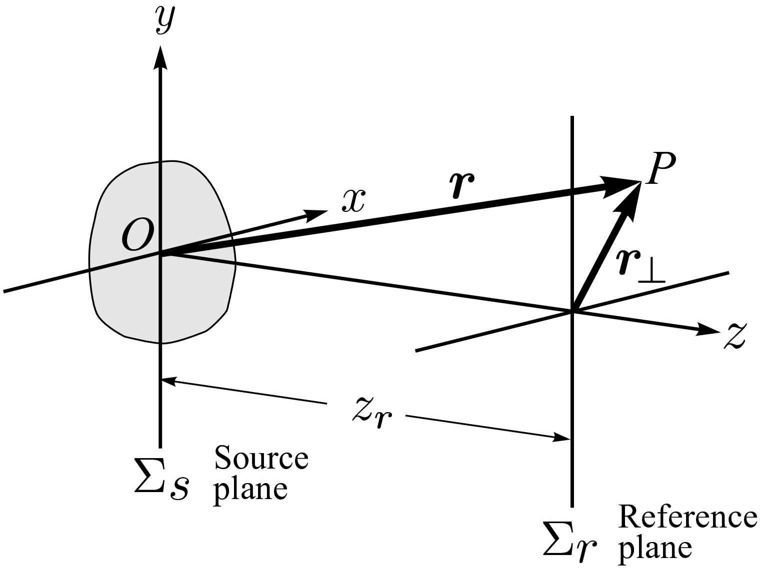

Fig. 2.2. Geometry of the optical system.

the field $U(\boldsymbol{r}_\perp, z_r; \nu)$ may be represented by a Fourier integral:

$$U(\boldsymbol{r}_\perp, z_r; \nu) = \frac{1}{2\pi} \iint_{-\infty}^{\infty} \tilde{U}(\boldsymbol{k}_\perp, z_r; \nu) \exp(i\boldsymbol{k}_\perp \cdot \boldsymbol{r}_\perp) d^2k_\perp \,, \tag{2.38}$$

and obviously the correspondence is

$$\tilde{U}(\boldsymbol{k}_\perp, z_r; \nu) = \frac{1}{2\pi} \iint_{-\infty}^{\infty} U(\boldsymbol{r}_\perp, z_r; \nu) \exp(-i\boldsymbol{k}_\perp \cdot \boldsymbol{r}_\perp) d^2r_\perp \,, \tag{2.39}$$

where $\boldsymbol{k} = (\boldsymbol{k}_\perp, k_z) = (k_x, k_y, k_z)$. Substitution of Eq. (2.38) into Eq. (2.37) gives a differential equation in $\tilde{U}(\boldsymbol{k}_\perp, z_r; \nu)$:

$$\left(\frac{\partial^2}{\partial z_r^2} + k_z^2 \right) \tilde{U}(\boldsymbol{k}_\perp, z_r; \nu) = 0 \,, \tag{2.40}$$

where

$$k_z = \begin{cases} [k^2 - \boldsymbol{k}_\perp^2]^{1/2} & (k_\perp \le k) \\ i[\boldsymbol{k}_\perp^2 - k^2]^{1/2} & (k_\perp \ge k) \end{cases} \,. \tag{2.41}$$

Although it is seen from Eq. (2.41) that the optical waves with $k_\perp \geq k$ are evanescent, we will take only the propagating wave into account. A propagation law of the field traveling from Σ_s to Σ_r in the positive direction of z is obtained as a solution of Eq. (2.40)[78, 79]:

$$\tilde{U}(\boldsymbol{k}_\perp, z_r; \nu) = \exp(ik_z z_r)\tilde{U}(\boldsymbol{k}_\perp, 0; \nu)\,. \tag{2.42}$$

The cross-spectral density across Σ_r is represented by a cross correlation of wavefields at two points $P(\boldsymbol{r}_\perp, z_r)$ and $P(\boldsymbol{r}'_\perp, z_r)$[1]:

$$W^{(z_r)}(\boldsymbol{r}'_\perp, \boldsymbol{r}_\perp; \nu) = \langle U^*(\boldsymbol{r}'_\perp, z_r; \nu)U(\boldsymbol{r}_\perp, z_r; \nu)\rangle\,. \tag{2.43}$$

The z coordinate in parentheses will be attached to W and $\tilde{W}$ to specify the plane considered in the following formulas. The four-dimensional Fourier transform of Eq. (2.43) gives a definition of the cross-spectral density in the $\boldsymbol{k}_\perp$ domain[79]:

$$\begin{aligned}&\tilde{W}^{(z_r)}(\boldsymbol{k}'_\perp, \boldsymbol{k}_\perp; \nu)\\ &\quad= \left(\frac{1}{2\pi}\right)^2 \iiiint_{-\infty}^{\infty} W^{(z_r)}(\boldsymbol{r}'_\perp, \boldsymbol{r}_\perp; \nu)\exp[-i(\boldsymbol{k}_\perp \cdot \boldsymbol{r}_\perp - \boldsymbol{k}'_\perp \cdot \boldsymbol{r}'_\perp)]d^2r_\perp d^2r'_\perp\,.\end{aligned} \tag{2.44}$$

From Eqs. (2.39), (2.43) and (2.44), $\tilde{W}^{(z_r)}(\boldsymbol{k}'_\perp, \boldsymbol{k}_\perp; \nu)$ can also be represented by

$$\tilde{W}^{(z_r)}(\boldsymbol{k}'_\perp, \boldsymbol{k}_\perp; \nu) = \langle \tilde{U}^*(\boldsymbol{k}'_\perp, z_r; \nu)\tilde{U}(\boldsymbol{k}_\perp, z_r; \nu)\rangle\,. \tag{2.45}$$

Substitution of Eq. (2.42) into Eq. (2.45) leads to the propagation law of the cross-spectral density in the Fourier domain from Σ_s to Σ_r[78, 79]:

$$\tilde{W}^{(z_r)}(\boldsymbol{k}'_\perp, \boldsymbol{k}_\perp; \nu) = \exp[i(k_z - k'_z)z_r]\tilde{W}^{(0)}(\boldsymbol{k}'_\perp, \boldsymbol{k}_\perp; \nu). \tag{2.46}$$

This expression for the propagation law of the cross-spectral density is simple and enables us to treat the propagation of the spatial coherence easily. In addition, it should be mentioned that the derivation of Eq. (2.46) does not require any paraxial approximations nor any assumptions on the state of coherence.

2.4 Correlation-induced spectral changes

In 1996, E. Wolf pointed out that the spectrum propagates from the spatially, partially coherent source is not invariant even though the light propagates through free space. In this section, let us briefly review the fundamental concept of the correlation-induced spectral changes.

First, we assume the following conditions:

1. Sources are planar and quasi-homogeneous.
2. Spectral profile is uniform across the source.

The quasi-homogeneous sources are characterized by the following conditions:

1. Source is large enough compared with the effective correlation length,
2. Intensity is almost uniform within the effective correlation length,
3. Spatial coherence function is space invariant.

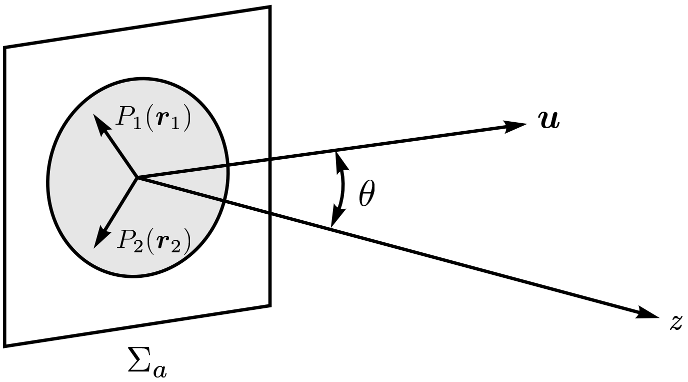

Fig. 2.3. Optical system considered.

With reference to Fig. 2.3, we consider a spatially, partially coherent source, two particular points $P_1(\boldsymbol{r}_1)$ and $P_2(\boldsymbol{r}_2)$ on the source plane, and the unit vector $\boldsymbol{u}$. If the source is quasi-homogeneous, the spectral degree of coherence across the source plane is represented by

$$\mu(\boldsymbol{r}_1, \boldsymbol{r}_2; \nu) = \mu(\boldsymbol{r}_1 - \boldsymbol{r}_2; \nu) \, . \tag{2.47}$$

In addition, if the spectral profile is uniform over the source area, the cross-spectral density across the source plane is represented by

$$W(\boldsymbol{r}_1, \boldsymbol{r}_1; \nu) = W(\boldsymbol{r}_2, \boldsymbol{r}_2; \nu) = S_p(\nu) \, , \tag{2.48}$$

and

$$W(\boldsymbol{r}_1, \boldsymbol{r}_2; \nu) = \epsilon(\boldsymbol{r}_1)\epsilon(\boldsymbol{r}_2) S_P(\nu) \mu(\boldsymbol{r}_1 - \boldsymbol{r}_2; \nu) \, , \tag{2.49}$$

where $\epsilon(\boldsymbol{r}_1)$ and $\epsilon(\boldsymbol{r}_2)$ are 1 within the source area and 0 outside the source area.

The radiant intensity $J_\nu(\boldsymbol{u})$ is proportional to the Fourier transform of the spectral degree of coherence across the source plane and $\cos^2\theta$, namely,

$$J_\nu(\boldsymbol{r}) = k^2 A S_P(\nu) \tilde{\mu}(k\boldsymbol{u}_\perp; \nu) \cos^2\theta \, , \tag{2.50}$$

where A is the area of the source and $\boldsymbol{u}_\perp = (u_x, u_y)$. By using the equation

$$\tilde{\mu}(\boldsymbol{f}; \nu) = \frac{1}{(2\pi)^2} \int_{-\infty}^{\infty} \mu(\boldsymbol{r}'; \nu) \exp(-i\boldsymbol{f} \cdot \boldsymbol{r}') d^2\boldsymbol{r}' \quad (\boldsymbol{r}' = \boldsymbol{r}_2 - \boldsymbol{r}_1) \, , \tag{2.51}$$

the normalized spectra in the far field is represented by

$$S_o(\boldsymbol{u}; \nu) = \frac{J_\nu(\boldsymbol{u})}{\displaystyle\int_0^\infty J_\nu(\boldsymbol{u}) d\nu} = \frac{k^2 S_P(\nu) \tilde{\mu}(k\boldsymbol{u}_\perp; \nu)}{\displaystyle\int_0^\infty k^2 S_P(\nu) \tilde{\mu}(k\boldsymbol{u}_\perp, \nu) d\nu} \tag{2.52}$$

Equation (2.52) implies that the normalized spectrum depends on $\boldsymbol{u}$, namely, the spectral profile depends on the location of the observation point. When the Fourier transform of the spectral degree of coherence is represented by a function of the product of the spatial-frequency and $\boldsymbol{u}_\perp$:

$$\tilde{\mu}(k\boldsymbol{u}_\perp; \nu) = F(\nu) \tilde{H}(\boldsymbol{u}_\perp) \, , \tag{2.53}$$

then Eq. (2.52) can be rewritten to the form

$$S_o(\boldsymbol{u};\nu) = \frac{k^2 S_P(\nu) F(\nu) \tilde{H}(\boldsymbol{u}_\perp)}{\displaystyle\int_0^\infty k^2 S_P(\nu) \tilde{H}(\boldsymbol{u}_\perp) d\nu} = \frac{k^2 S_P(\nu) F(\nu)}{\displaystyle\int_0^\infty k^2 S_P(\nu) F(\nu) d\nu} \, . \tag{2.54}$$

In contrast to Eq. (2.52), Eq. (2.54) implies that the spectrum is independent of $\boldsymbol{u}_\perp$. Taking the Fourier transform of Eq. (2.53) gives

$$\begin{aligned} \mu(\boldsymbol{r}';\nu) &= F(\nu) \int_{-\infty}^{\infty} \tilde{H}(\boldsymbol{u}_\perp) \exp(ik\boldsymbol{u}_\perp \cdot \boldsymbol{r}') d^2(k\boldsymbol{u}_\perp) \\ &= k^2 F(\nu) H(k\boldsymbol{r}') \, . \end{aligned} \tag{2.55}$$

If $\mu(\boldsymbol{r}';\nu)$ is 0 only when $\boldsymbol{r}' = \boldsymbol{r}_1 - \boldsymbol{r}_2$, $\mu(0;\nu) = 1$ for all frequencies, and the following equations hold with the help of Eq. (2.55)

$$\left. \begin{aligned} &\mu(0;\nu) = k^2 F(\nu) H(0) = 1 \\ &k^2 F(\nu) = \{H(0)\}^{-1} \end{aligned} \right\} . \tag{2.56}$$

Since both sides of Eq. (2.56) must be a constant, let the constant be α, and

$$F(\nu) = \frac{\alpha}{k^2} \, . \tag{2.57}$$

We obtain the following equation by substituting Eq. (2.57) into Eq. (2.54):

$$S_o(\boldsymbol{u};\nu) = S_o(\nu) = \frac{S_P(\nu)}{\displaystyle\int_0^\infty S_P(\nu) d\nu} \, . \tag{2.58}$$

Equation (2.58) means that the observed spectral profile is

1. independent of the observation location

and

2. same as that of the source spectrum.

Moreover, substituting Eq. (2.57) into Eq. (2.55), and rewriting $\boldsymbol{r}' = \boldsymbol{r}_1 - \boldsymbol{r}_2$ and $\alpha H = h$ gives

$$\mu(\boldsymbol{r}_2 - \boldsymbol{r}_1;\nu) = h[k(\boldsymbol{r}_2 - \boldsymbol{r}_1)] = h\left[\frac{2\pi\nu}{c}(\boldsymbol{r}_2 - \boldsymbol{r}_1)\right] \, . \tag{2.59}$$

Equation (2.59) is called the scaling law and this means that the propagated spectrum is invariant if the spectral degree of coherence across the source takes the form of Eq. (2.59). In other words, the propagated spectrum changes if the spectral degree of coherence across the source does not obey the scaling law.

2.5 Conclusion

We reviewed the basic concepts of the second-order spatial coherence functions described in the space-time domain and the space-frequency domain. While the spatial coherence function in the space-time domain such as the mutual coherence function describes the spatial correlation of the quasi-monochromatic wavefields, the coherence function in the space-frequency domain such as the cross-spectral density plays an important role in describing the spatial correlation of the wavefields with the wide spectral bandwidth. The introduction of the correlation-induced spectral changes was also reviewed. The condition for the spectral invariance was derived.

Chapter 3

Observations of correlation-induced spectral changes

3.1 Introduction

It is difficult to distinguish the correlation induced spectral changes from the spectral changes due to dispersive diffraction. Young's interference experiments with double pinholes are frequently referred to explain the correlation-induced spectral changes.[80] However, the dispersive diffraction caused by the definite size of the double pinholes is inevitable when one measures the spectral changes and the spectral coherence function. Most of the papers that reported the experiments to measure the correlation-induced spectral changes neglected the effect of the dispersive diffraction. To investigate more quantitatively the relationship between the spatial coherence across the source and the correlation-induced spectral changes, it is important to know how both the dispersive diffraction and the spatial coherence property across the source effect on the spectral profile that is observed at the far field. In addition, it is also essential to establish reliable techniques to measure the correlation-induced spectral changes released from the dispersive diffraction.

From this background, two types of measurements of the spectral changes are presented in this chapter, namely the measurement of the spectral change that is caused by both the dispersive diffraction and the spatial coherence property, and the measurement of the spectral change that is caused by only the source correlation. The former one is conducted by using the aperture that is regarded as a secondary source. The spatial coherence property across the secondary source depends on the linear dimension and the intensity distribution of the primary source. The coherence area characterizes the spatial coherence across the secondary source plane, and the peak shift of the observed spectrum is evaluated by the ratio of the coherence area to the secondary source area. On the other hand, the latter one is conducted with the wavefront folding interferometer[81] that enables us to measure the spectral changes that depend on only the source correlation. We introduce the spectral modulation factor for discussing the relationship between the change in observed spectra and the source correlation.

3.2 Correlation-induced spectral changes and dispersive diffraction

3.2.1 Formulation of problem

Wolf showed[3] (refer to Fig. 3.1) that the spectral density $S_Q(l\boldsymbol{u};\nu)$ observed at Q in the far field is associated with the uniform source spectral density $S(\nu)$ as follows:

$$S_Q(l\boldsymbol{u};\nu) \propto S(\nu)\tilde{\mu}(k\boldsymbol{u};\nu)\,, \tag{3.1}$$

where

$$\tilde{\mu}(k\boldsymbol{u};\nu) = \frac{1}{(2\pi)^2}\iint \mu_G(\boldsymbol{r}_1-\boldsymbol{r}_2;\nu)\exp[-k\boldsymbol{u}\cdot(\boldsymbol{r}_1-\boldsymbol{r}_2)]d^2(r_1-r_2)\,. \tag{3.2}$$

Here, $\boldsymbol{u}$ is the unit vector directed from a source point to an observer separated by a distance l, and $\tilde{\mu}(k\boldsymbol{u};\nu)$ represents the two-dimensional Fourier transform of the spectral degree of coherence $\mu_G(\boldsymbol{r}_1 - \boldsymbol{r}_2;\nu)$ with respect to the difference vector $(\boldsymbol{r}_1 - \boldsymbol{r}_2)$. As readily understood from Eqs.(3.1) and (3.2), the spectrum of the light emanating from the source changes on propagation in free space, depending upon the source correlation that is characterized by the spectral degree of coherence.

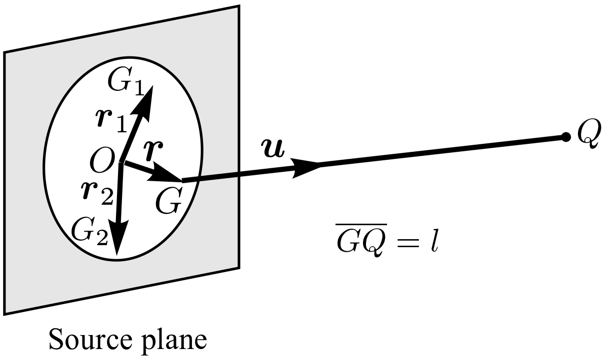

Fig. 3.1. Coordinate system explaining Eqs.(3.1) and (3.2).

Let us now introduce a spatially, partially coherent secondary source that is produced by a spatially incoherent source in the Fresnel region. This secondary source is conveniently characterized in terms of the coherence area A_c; any paired beams of the light emitted from inside the area can interfere with each other, but from outside the area interference is almost impossible. Let a circular aperture be put in the secondary source plane, and introduce the ratio of A_c to the area of aperture A_a for quantitative discussion. We assume two limiting cases, namely the aperture is regarded as a spatially coherent or incoherent source according to whether the area of the aperture is much larger or smaller than A_c. It will be demonstrated in the following how the ratio of A_c to A_a determines the spectral changes.

We consider a change in optical spectrum that is observed in the far field from

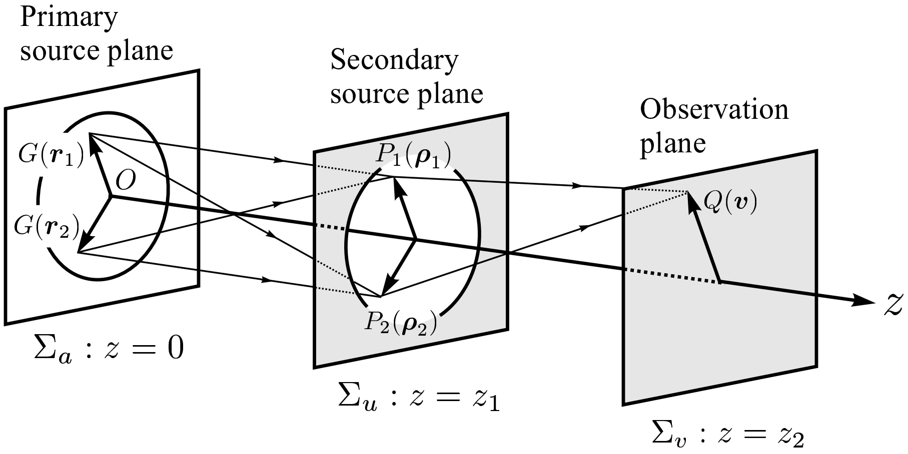

Fig. 3.2. Optical system considered.

the secondary source, referring to Fig. 3.2. Here, Σ_a denotes a planar primary source plane specified by two-dimensional vector $\boldsymbol{r}$ over which the primary source is spatially incoherent, and Σ_u a plane of the secondary source that is specified by two-dimensional vector $\boldsymbol{\rho}$ over which the secondary source is spatially, partially coherent. As stated in the van Cittert-Zernike theorem[82], the optical wavefields propagated from the primary incoherent source become spatially, partially coherent in the Fresnel region. Note that Σ_u consists of the input and output planes Σ_u^- and Σ_u^+; just before and behind Σ_u. The optical wavefields propagates from the secondary source to an observation plane Σ_v that is located in the far field, which is specified by two-dimensional vector $\boldsymbol{v}$. The objective of this subsection is to derive the expressions for the normalized spectra, $S_u^-(z_1;\nu)$ and $S_v(z_2;\nu)$ at Σ_u^- and Σ_v, and to examine how the two spectra differ from each other. Let $t(\boldsymbol{\rho},\nu)$ be the complex amplitude transmittance from Σ_u^- to Σ_u^+, and the expression for the propagation law of the cross-spectral density[83] from Σ_u to Σ_v is

$$W_v(\boldsymbol{v}_1, \boldsymbol{v}_2, z_2; \nu,) = \iiiint_{\Sigma_u} W_u^-(\boldsymbol{\rho}_1, \boldsymbol{\rho}_2, z_1; \nu) \langle t^*(\boldsymbol{\rho}_1; \nu) t(\boldsymbol{\rho}_2; \nu) \rangle \times K^*(\boldsymbol{\rho}_1, \boldsymbol{v}_1, z'; \nu) K(\boldsymbol{\rho}_2, \boldsymbol{v}_2, z'; \nu) d^2\rho_1 d^2\rho_2 \,. \tag{3.3}$$

Here

$$\left.\begin{array}{lcl} W_v(\boldsymbol{v}_1, \boldsymbol{v}_2, z_2; \nu) & = & \langle U_v^*(\boldsymbol{v}_1, z_2; \nu) U_v(\boldsymbol{v}_2, z_2; \nu) \rangle \\ W_u^-(\boldsymbol{\rho}_1, \boldsymbol{\rho}_2, z_1; \nu) & = & \langle U_u^{-*}(\boldsymbol{\rho}_1, z_2; \nu) U_u^-(\boldsymbol{\rho}_2, z_2; \nu) \rangle \end{array}\right\} \tag{3.4}$$

are, respectively, the cross-spectral densities in Σ_v and Σ_u^-. U_u and U_v are the fields at Σ_u^- and Σ_v, and $K(\boldsymbol{\rho}, \boldsymbol{v}, z'; \nu)$ is the impulse response from Σ_u^- to Σ_v with $z' = z_2 - z_1$. The spectral degree of coherence[3] is given by

$$\mu^-(\boldsymbol{\rho}_1, \boldsymbol{\rho}_2, z_1; \nu) = \frac{W_u^-(\boldsymbol{\rho}_1, \boldsymbol{\rho}_2, z_1; \nu)}{S_u^-(z_1; \nu)} \,. \tag{3.5}$$

Hence Eq. (3.3) readily leads to the optical spectrum at a point $Q(\boldsymbol{v})$ in Σ_v by putting $\boldsymbol{v}_1 = \boldsymbol{v}_2 = \boldsymbol{v}$,[83]

$$\begin{array}{rcl} S(\boldsymbol{v}, z_2; \nu) & = & W(\boldsymbol{v}, \boldsymbol{v}, z_2; \nu) \\ & = & S_u^-(z_1, \nu) \iiiint_{\Sigma_v} \mu^-(\boldsymbol{\rho}_1, \boldsymbol{\rho}_2, z_1; \nu) \langle t^*(\boldsymbol{\rho}_1; \nu) t(\boldsymbol{\rho}_2; \nu) \rangle \\ & \times & K^*(\boldsymbol{\rho}_1, \boldsymbol{v}, z'; \nu) K(\boldsymbol{\rho}_2, \boldsymbol{v}, z'; \nu) d^2\rho_1 d^2\rho_2 \,. \end{array} \tag{3.6}$$

In the framework of the paraxial approximation to the impulse response, Eq. (3.6) reduces to

$$S(\boldsymbol{v}, z_2; \nu) = \left(\frac{\nu}{cz'}\right)^2 S_u^-(z_1; \nu) \iiiint_{\Sigma_u} |\mu^-(\boldsymbol{\rho}_1, \boldsymbol{\rho}_2, z_1; \nu)| \langle t^*(\boldsymbol{\rho}_1; \nu) t(\boldsymbol{\rho}_2; \nu) \rangle \times \exp\left\{ i \left[-\frac{2\pi\nu}{cz'} (\boldsymbol{\rho}_1 - \boldsymbol{\rho}_2) \cdot \boldsymbol{v} + \arg \mu^-(\boldsymbol{\rho}_1, \boldsymbol{\rho}_2, z_1; \nu) \right] \right\} d^2\rho_1 d^2\rho_2 \,. \tag{3.7}$$

It should be noted that $t(\boldsymbol{\rho}; \nu) = 1$ or 0 according to whether the point $P(\boldsymbol{\rho})$ is located inside or outside the aperture. This equation implies that the spectrum propagating from Σ_u^- to the far field depends on $\mu(\boldsymbol{\rho}_1, \boldsymbol{\rho}_2, z_2; \nu)$.

We intend to characterize the secondary source at Σ_u^- in terms of the coherence area produced by the primary source. The coherence area is defined[82] as,

$$A_c = \iint_{\Sigma_u} |\mu^-(\boldsymbol{\rho}', z_1; \nu)|^2 d^2\rho' \,, \quad (\boldsymbol{\rho}' = \boldsymbol{\rho}_1 - \boldsymbol{\rho}_2) \,. \tag{3.8}$$

The ratio of A_c to the aperture is readily given by

$$A_c/\pi\rho^2 = \frac{\displaystyle\iint_{\Sigma_u} |\mu^-(\boldsymbol{\rho}_1, \boldsymbol{\rho}_2, z_1; \nu)|^2 d^2\rho'}{\pi\rho^2} \,. \tag{3.9}$$

As can be seen from Eqs. (3.7) and (3.9), which are commonly associated with each other through $|\mu^-|$, $S(\boldsymbol{v}, z_2; \nu)$ and $A_c/\pi\rho^2$ are uniquely determined if μ^- is given in advance. As a result, spectrum $S(\boldsymbol{v}, z_2; \nu)$ to be observed at a point $P(\boldsymbol{v})$ in Σ_v changes as a function of $A_c/\pi\rho^2$. Remember that the aperture located in Σ_u is almost spatially coherent or incoherent according to whether it is much smaller or larger than A_c. With reference to the van Cittert-Zernike theorem[82], the spectral degree of coherence in Σ_u^- is given by normalizing the two-dimensional Fourier transform of the intensity distribution of the primary source,

$$\mu^-(\boldsymbol{\rho}_1, \boldsymbol{\rho}_2, z_1; \nu) = \frac{\exp(-i\psi) \displaystyle\iint_{\Sigma_a} I(\boldsymbol{r}) \exp\left[\frac{2\pi i\nu}{cz'}(\boldsymbol{\rho}_1 - \boldsymbol{\rho}_2) \cdot \boldsymbol{r}\right] d^2r}{\displaystyle\iint_{\Sigma_a} I(\boldsymbol{r}) d^2r} \,, \tag{3.10}$$

where

$$\psi = \frac{\pi\nu}{cz_1}(|\boldsymbol{\rho}_1|^2 - |\boldsymbol{\rho}_2|^2) \,. \tag{3.11}$$

On substitution from Eq. (3.10) into Eq. (3.9), we can obtain the ratio,

$$A_c/\pi\rho^2 = \pi \left(\frac{cz'}{\pi\nu\rho}\right)^2 \frac{\displaystyle\iint_{\Sigma_a} [I(\boldsymbol{r})]^2 d^2r}{\left[\displaystyle\iint_{\Sigma_a} I(\boldsymbol{r}) d^2r\right]^2} \,. \tag{3.12}$$

3.2.2 Coherence area

We consider the coherence area A_c associated with the intensity distribution of a primary circular source that is spatially incoherent. Let it have the center symmetric intensity and the spatially uniform spectrum $S(\nu)$. This expression takes the form,

$$I(r, \alpha, \nu) = \left(1 - \frac{r}{R}\right)^{\alpha} S(\nu) \,, \tag{3.13}$$

where r denotes the radial coordinate from the center of the circular source with radius R, and α is a variable parameter. For the limiting case $\alpha = 0$, the primary source is flat in intensity, while the source reduces to a point source for $\alpha \to \infty$. On substitution of Eq. (3.13) into Eq. (3.12), we have

$$A_c/\pi\rho^2 = \frac{c^2}{4\pi\nu^2\rho^2} \frac{(\alpha+2)^2(\alpha+1)}{\Delta\Omega(2\alpha+1)} \,, \tag{3.14}$$

where

$$\Delta\Omega = \pi \left(\frac{R}{z_1}\right)^2 \tag{3.15}$$

is the solid angle seen from Σ_u to Σ_a. It should be noted that $A_c/\pi\rho^2$ significantly varies depending upon the two parameters α and $\Delta\Omega$. For convenience sake in the experiment, however, let us confine ourselves to the case where the secondary source is formed in the far field from the primary source, which can be simply achieved by inserting a Fourier transforming lens with focal length f between Σ_a and Σ_u.

The solid angle is thereby rewritten as,

$$\Delta\Omega = \pi \left(\frac{R}{f}\right)^2 \,. \tag{3.16}$$

It is readily understood that variations of spatial coherence over the aperture is realized by controlling $A_c/\pi\rho^2$. Since A_c varies as a function of α and $\Delta\Omega$, the following two cases are considered: one is that where the primary source is flat ($\alpha = 0$) in

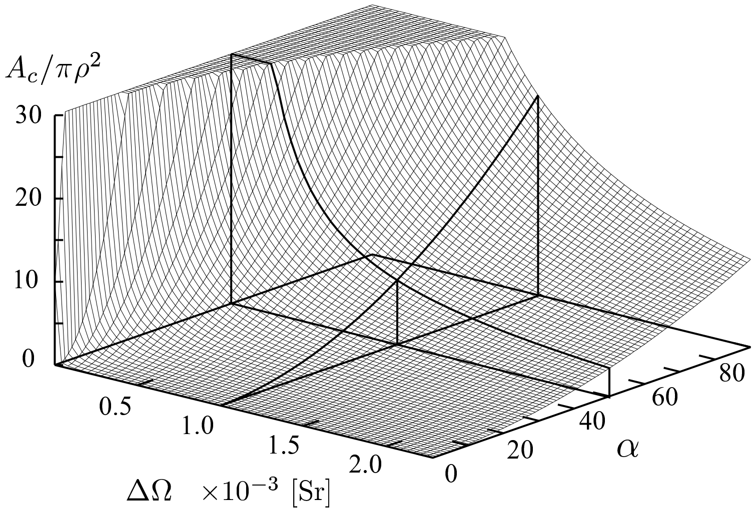

Fig. 3.3. Theoretically calculated coherence area divided by circular area as a function of two parameters, $\Delta\Omega$ and α.

intensity distribution but the solid angle $\Delta\Omega$ is made variable, and the other is where the intensity distribution is made variable for constant $\Delta\Omega$. The numerical calculation for $A_c/\pi\rho^2$ was made as shown in Fig. 3.3. The larger α is and the smaller $\Delta\Omega$ is, the more $A_c/\pi\rho^2$ approaches the spatially coherent state. In contrast, the smaller α is and the larger $\Delta\Omega$ is, the more $A_c/\pi\rho^2$ approaches the spatially incoherent state. Evidently $A_c/\pi\rho^2$ can be uniquely determined if the values of $\Delta\Omega$ and α are given. The value of $A_c/\pi\rho^2$ is indicated, for example, at the transection of the two curves plotted using the typical values of $\Delta\Omega = 0.001$ Sr and $\alpha = 50$. Since the secondary source truncated by the circular aperture is almost coherent for $A_c/\pi\rho^2 \gg 1$, the cause of the peak shift of the observed spectrum would be dispersive diffraction alone by the aperture itself. In contrast, for the case $A_c/\pi\rho^2 \ll 1$, no peak shift would take place because the secondary source is almost spatially incoherent. In general, however, the secondary source is spatially, partially coherent for $A_c/\pi\rho^2 \sim 1$, and thus the cause of the peak shift would be due to both factors, source correlation and dispersive diffraction. We confine ourselves to the peak shift of the Gaussian-like spectrum which will be observed at a particular point in Σ_v.

3.2.3 Experiments and numerical calculation

The experiment was conducted by scanning optical frequency by a spectrum analyzer with spectral resolution of 0.1 nm. The aperture put on Σ_u was 200 μm in diameter. The optical setup is shown in Fig. 3.4. The primary source was the superluminescent diode (SLD), and its spectral profile measured at a point in Σ_u^- is shown in Fig. 3.5. The peak frequency and the full width at half maximum are $\nu_c = 3.56 \times 10^{14}$ Hz and $\Delta\nu = 8.74 \times 10^{12}$ Hz, respectively. The spectrum $S^-(\boldsymbol{u}, z_1; \nu)$ at Σ_u^- had a Gaussian-like spectral profile similar to the primary source and was confirmed to be the same everywhere in Σ_u^-. The tip of SLD used worked as a point source emitting a spherical wave. This was confirmed by scanning an Airy pattern in the far field at the central frequency of the spectrum; this means that the secondary source plane Σ_u^- was illuminated spatially coherently.

It is essential for the present experiment that the coherence area A_c can be controlled in Σ_u^-. This requirement is fulfilled equivalently by moving the tip of SLD stepwise over Σ_a by means of computer-aided processing. The sum of all the luminous obtained by stepwise moving points gives rise equivalently to an extended spatially incoherent source. In other words, superposition of all the spectra that is produced by every stepwise moving point source over Σ_a, results in the spectrum $S(\boldsymbol{v}, z_2; \nu)$.

A series of optical spectra were measured at four locations $v = 0$, $v = 0.5$, 1.0, and 2.0 mm from the origin $v = 0$ by use of a 150 μm diameter fiber-probe linked to a spectrum analyzer. Peak shifts in the spectrum are shown in Fig. 3.6. Figure

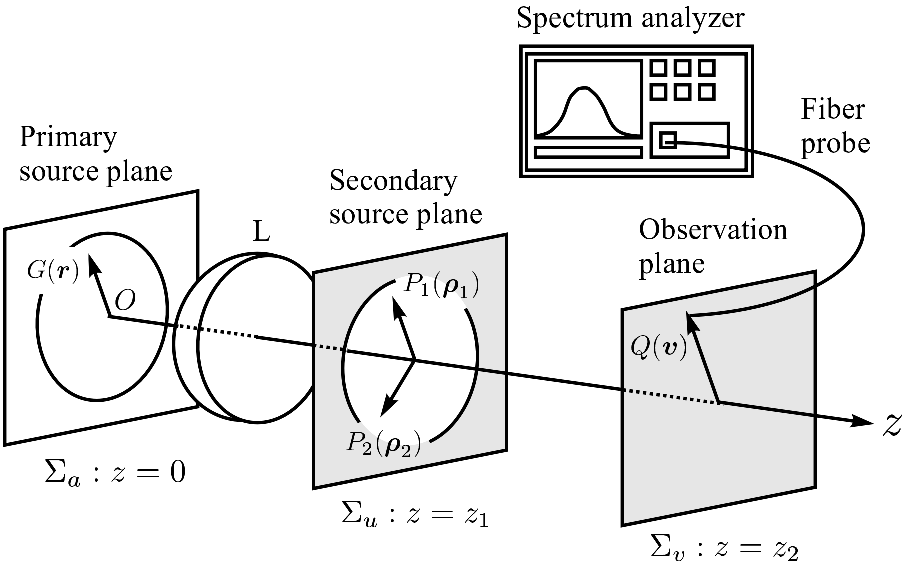

Fig. 3.4. Experimental arrangements.

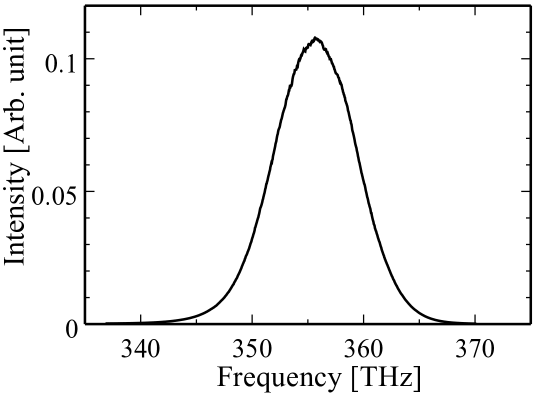

Fig. 3.5. Spectral profile of the SLD used.

(a) denotes the case where the solid angle $\Delta\Omega$ is made variable for the flat intensity ($\alpha = 0$) of the primary source, and (b) the case where the intensity distribution is made variable ($\alpha \neq 0$) for a constant of $\Delta\Omega$. The peak shifts were determined by the Gaussian fitting of the measured spectral profiles.

The measured and numerically computational results are represented by three

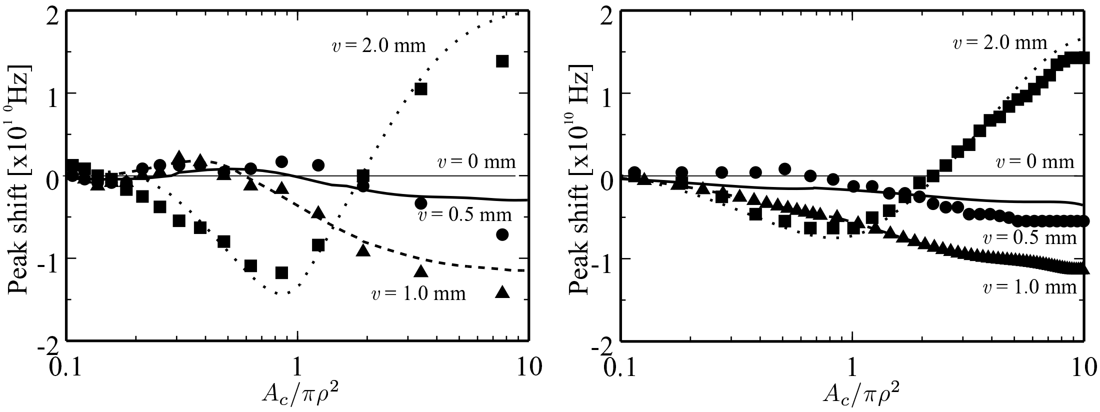

(a) (b)

Fig. 3.6. Experimental and theoretical results of the spectral peak shift as a function of $A_c/\pi\rho^2$.

kinds of plotted and smooth curves, respectively. Fairly good agreement can be seen between the two results. The four locations denoted by v's are indicated in the figure. As can be seen, the peak shift in the spectrum does not occur at the incoherent limit ($A_c/\pi\rho^2 \to 0$), whereas the redshift or blueshift takes place as $A_c/\pi\rho^2$ increases in value depending upon the observed locations in Σ_v, and is expected to reach the maximum at the coherent limit ($A_c/\pi\rho^2 \to \infty$). Each peak shift in (a) almost resembles each in (b), but the red shift in (a) at $A_c/\pi\rho^2 \sim 0.5$ for $v = 2.0$ mm is apparently larger than that in (b). In this experiment, the spatial coherence over the secondary source plane was characterized simply by the coherence area. However, more complex structure of the coherence function effects on the spectral changes, and the difference between Figs. 3.6 (a) and (b) comes from this fact.

3.3 Observations of spectral changes with wavefront folding interferometer

3.3.1 Spectral coherence formed by uncorrelated two point sources

In this section, we study the spectral changes caused by only the source correlation from both the theoretical and experimental points of view. With reference to Fig. 3.7 (a), let us examine the spectral degree of coherence formulated across the secondary source plane in the Fresnel diffraction region from an opaque primary source plane with two point sources. As will be described below, a change in spectrum is observed by use of a wavefront folding image-forming system arranged just after the secondary source plane. The primary and secondary source planes are specified, respectively, by one dimensional axes ζ and ξ. The two point sources, which do not have the same spectrum and whose wavefields are spatially, mutually uncorrelated, are located at ζ_1 and ζ_2 on the ζ axis. The optical wavefields of the primary source is represented by an analytic signal $V(\zeta;t)$ varying with time t. Since the analytic signal $V(\zeta;t)$ is composed of all the realizable frequency components $U(\zeta;\nu)$, $V(\zeta;t)$ and $U(\zeta;\nu)$ are related to each other by the Fourier transform pair:

$$V(\zeta;t) = \frac{1}{2\pi}\int_0^\infty U(\zeta;\nu)\exp(-2\pi i\nu t)d\nu\,, \tag{3.17}$$

and

$$U(\zeta;\nu) = \int_{-\infty}^\infty V(\zeta;t)\exp(2\pi i\nu t)dt\,. \tag{3.18}$$

Similarly, the analytic signal and its Fourier spectrum in the secondary source plane can be expressed in the paired form

$$V(\xi;t) = \frac{1}{2\pi}\int_0^\infty U(\xi;\nu)\exp(-2\pi i\nu t)d\nu\,, \tag{3.19}$$

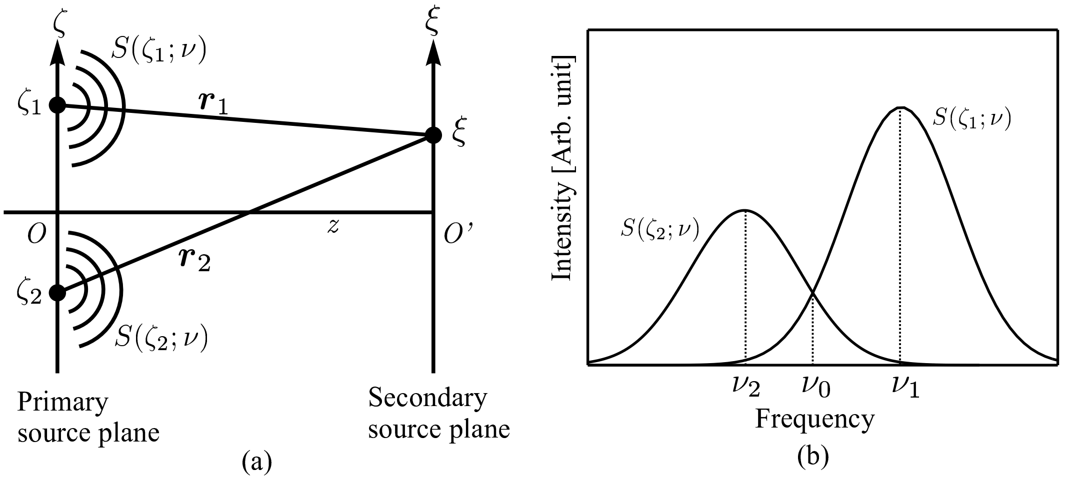

Fig. 3.7. (a) Optical system for illustration. (b) Two Gaussian-like spectra $S(\zeta_1;\nu)$ and $S(\zeta_2;\nu)$.

$$U(\xi;\nu) = \int_{-\infty}^{\infty} V(\xi;t)\exp(2\pi i\nu t)dt\,. \tag{3.20}$$

In the present situation, when we consider that the primary two point sources are located at ζ_1 and ζ_2 on the ζ axis, the analytic signal in the ζ axis can be expressed in the form,

$$V(\zeta;t) = V'(\zeta;t)[\delta(\zeta-\zeta_1)+\delta(\zeta-\zeta_2)]\,, \tag{3.21}$$

where $V'(\zeta;t)$ is the analytic signal existing on the left plane of the opaque screen in the primary source plane, and $\delta(\zeta-\zeta_1)$ and $\delta(\zeta-\zeta_2)$ are the Dirac delta functions that represent the two points at ζ_1 and ζ_2. On substitution from Eq. (3.21) into Eq. (3.18), we readily obtain

$$U(\zeta;\nu) = U'(\zeta;\nu)\delta(\zeta-\zeta_1) + U'(\zeta;\nu)\delta(\zeta-\zeta_2)\,, \tag{3.22}$$

with

$$U'(\zeta;\nu) = \int_{-\infty}^{\infty} V'(\zeta;t)\exp(2\pi i\nu t)dt\,. \tag{3.23}$$

Taking into account all the contributions of the wavefields of the primary source, we now consider the propagation of the wavefields from the primary source to the secondary source plane. As long as the linear relationship is between the primary source plane and the secondary source plane in the framework of the paraxial approximation, $V(\xi;t)$ is simply associated with $V(\zeta;t)$ by the convolution integral with respect to time t:

$$V(\xi;t) = \iint_{-\infty}^{\infty} h(\zeta,\xi;t-t')V(\zeta;t')d\zeta dt' \,, \tag{3.24}$$

where $h(\zeta,\xi;t)$ is the impulse in the time domain from a point $P(\zeta)$ on the primary source to a point $Q(\xi)$ on the secondary source plane. The corresponding transmission function in the frequency domain is represented[84] by

$$H(\zeta,\xi;\nu) = \frac{i\nu \exp(-2\pi i\nu r/c)}{cr} \,, \tag{3.25}$$

since $r = [z^2 + (\zeta-\xi)^2]^{1/2} \simeq z - \zeta\xi/z$ is the far-field distance from $P(\zeta)$ to $Q(\xi)$, with z being the distance between the primary and the secondary source planes. Also, it is evident from the definition

$$H(\zeta,\xi;\nu) = \int_{-\infty}^{\infty} h(\zeta,\xi;t)\exp(-i\nu t)dt \,. \tag{3.26}$$

Substitution of Eq. (3.24) into Eq. (3.20) leads us to take a Fourier transform of the convolution integral, which reduces Eq. (3.20) with the help of Eqs. (3.25) and (3.26) to

$$\begin{aligned} U(\xi;\nu) &= \int_{-\infty}^{\infty} H(\zeta,\xi;\nu)U(\zeta;\nu)d\zeta \\ &= \frac{i\nu}{cz}\int_{-\infty}^{\infty} U(\zeta;\nu)\exp\left[-\frac{2\pi i\nu}{c}\left(z-\frac{\zeta\xi}{z}\right)\right]d\zeta \,, \end{aligned} \tag{3.27}$$

under the paraxial approximation $r \simeq z$. We are now in a position to formulate the cross-spectral density across the ξ axis defined by

$$W(\xi_1,\xi_2;\nu) = \langle U^*(\xi_1;\nu)U(\xi_2;\nu)\rangle \,. \tag{3.28}$$

On substituting of Eq. (3.27) into Eq. (3.28), the cross-spectral density is given by

$$W(\xi_1, \xi_2; \nu) = \left(\frac{\nu}{cz}\right)^2 \exp\left[\frac{2\pi i\nu\zeta}{cz}(\xi_1 - \xi_2)\right] \iint_{-\infty}^{\infty} \langle U^*(\zeta; \nu)U(\zeta'; \nu)\rangle d\zeta d\zeta' \, . \qquad (3.29)$$

Remember that not only are the optical wavefields from the two point sources uncorrelated with each other, but the two optical wavefields with different frequency components are also uncorrelated with each other, as illuminated, respectively, by

$$\left.\begin{array}{l} \langle U'^*(\zeta_2; \nu)U'(\zeta_1; \nu)\rangle = \langle U'^*(\zeta_1; \nu)U'(\zeta_2; \nu)\rangle = 0 \quad (\zeta_1 \neq \zeta_2) \\ \langle U'^*(\zeta_1; \nu')U'(\zeta_1; \nu)\rangle = \langle U'^*(\zeta_2; \nu')U'(\zeta_2; \nu)\rangle = 0 \quad (\nu \neq \nu') \end{array}\right\} . \qquad (3.30)$$

With reference to relations (3.22) and (3.30), the integral part of Eq. (3.29) is rearranged into

$$\begin{aligned} &\iint_{-\infty}^{\infty} \langle U^*(\zeta'; \nu)U(\zeta; \nu)\rangle d\zeta d\zeta' \\ &\qquad = \int_{-\infty}^{\infty} d\zeta_1' \int_0^{\infty} \langle U'^*(\zeta_1'; \nu')U'(\zeta_1; \nu)\rangle \delta(\nu - \nu')\delta(\zeta_1 - \zeta_1')d\nu' \\ &\qquad + \int_{-\infty}^{\infty} d\zeta_2' \int_0^{\infty} \langle U'^*(\zeta_2'; \nu')U'(\zeta_2; \nu)\rangle \delta(\nu - \nu')\delta(\zeta_2 - \zeta_2')d\nu' \\ &\qquad = S(\zeta_1; \nu) + S(\zeta_2; \nu) \, , \qquad (3.31) \end{aligned}$$

where

$$\left.\begin{array}{ll} S(\zeta_1; \nu) & = \langle |U'(\zeta_1; \nu)|^2\rangle \\ S(\zeta_2; \nu) & = \langle |U'(\zeta_2; \nu)|^2\rangle \end{array}\right\} \qquad (3.32)$$

stand for the respective spectra of the two primary sources.

Hence, we obtain

$$W(\xi_1, \xi_2; \nu) = \left(\frac{\nu}{cz}\right)^2 \left[S(\zeta_1; \nu) \exp\left(\frac{2\pi i\nu}{cz}\zeta_1\Delta\xi\right) + S(\zeta_2; \nu) \exp\left(\frac{2\pi i\nu}{cz}\zeta_2\Delta\xi\right)\right] , (3.33)$$

where $\Delta\xi = \xi_1 - \xi_2$. This cross-spectral density gives the spectral degree of coherence defined by

$$\mu(\xi_1, \xi_2; \nu) = \mu(\Delta\xi; \nu)$$

$$
\begin{aligned}
&= \frac{W(\xi_1, \xi_2; \nu)}{[W(\xi_1, \xi_1; \nu) W(\xi_2, \xi_2; \nu)]^{1/2}} \\
&= \frac{S_1(\nu)}{S_1(\nu) + S_2(\nu)} \exp\left(\frac{i\nu}{cz}\zeta_1 \Delta\xi\right) + \frac{S_2(\nu)}{S_1(\nu) + S_2(\nu)} \exp\left(\frac{i\nu}{cz}\zeta_2 \Delta\xi\right) \,, \quad (3.34)
\end{aligned}
$$

where the two spectra are expressed as $S_1(\nu) = S(\zeta_1; \nu)$ and $S_2(\nu) = S(\zeta_2; \nu)$ for brevity.

We proceed to the next stage to investigate how $\mu(\Delta\xi; \nu)$ depends on the two uncorrelated spectra as well as on the two point source locations. For this purpose, it is convenient to write for μ by the polar coordinate system,

$$
\mu(\Delta\xi; \nu) = |\mu| \exp(i \arg \mu) \,, \tag{3.35}
$$

where

$$
\begin{aligned}
|\mu(\Delta\xi; \nu)| = {} & \frac{1}{S_1(\nu) + S_2(\nu)} \\
& \times \left\{ S_1(\nu)^2 + S_2(\nu)^2 + 2 S_1(\nu) S_2(\nu) \cos\left[\frac{2\pi\nu\Delta\xi}{cz}(\zeta_1 - \zeta_2)\right] \right\}^{1/2} , \quad (3.36)
\end{aligned}
$$

$$
\arg \mu(\Delta\xi; \nu) = \tan^{-1} \left[\frac{S_1(\nu) \sin\left(\dfrac{2\pi\nu\Delta\xi\zeta_1}{cz}\right) + S_2(\nu) \sin\left(\dfrac{2\pi\nu\Delta\xi\zeta_2}{cz}\right)}{S_1(\nu) \cos\left(\dfrac{2\pi\nu\Delta\xi\zeta_1}{cz}\right) + S_2(\nu) \cos\left(\dfrac{2\pi\nu\Delta\xi\zeta_2}{cz}\right)} \right] . \tag{3.37}
$$

It is recognized that $|\mu(\Delta\xi; \nu)|$ is space invariant with respect to the two point source locations, but $\arg \mu(\Delta\xi; \nu)$ is not, as is evident from Eqs. (3.36) and (3.37). The space variant nature of $\arg \mu(\Delta\xi; \nu)$ with respect to ζ arises from the asymmetric arrangement of the two point sources across the ζ axis.

To explore μ more quantitatively, the following parameters are introduced under the assumption that the spectrum is Gaussian at each point source:

$$
\zeta_o \equiv \frac{\zeta_1 + \zeta_2}{2} \,, \tag{3.38}
$$

$$\Delta\zeta \equiv \zeta_1 - \zeta_2 \,, \tag{3.39}$$

$$\Delta\nu \equiv \nu_1 - \nu_2 \,, \tag{3.40}$$

$$R(\nu_1, \nu_2) = \frac{S_1(\nu_1)}{S_2(\nu_2)} \,, \tag{3.41}$$

where ν_1 and ν_2 are, respectively, the central frequencies giving the peaks of the respective Gaussian spectra (see Fig. 3.7 (b)). It should be kept in mind that ζ_o and $\Delta\zeta$ represent, respectively, the central location and the separation of the two point sources. Note that the two point source arrangement asymmetric to the optical axis is simply implemented by making $\zeta_o \neq 0$. The results of $|\mu(\Delta\xi;\nu)|$ and $\arg\mu(\Delta\xi;\nu)$, computed with Eqs. (3.36) and (3.37) are shown in Fig. 3.8: Figs. 3.8(a)-3.8(g) and 3.8(b)-3.8(h) represent $|\mu|$ and $\arg\mu$. Each horizontal pair of the figures, for example 3.8(a) and 3.8(b), is depicted with the same parameters. The central frequencies ν_1 and ν_2 for Figs. 3.8(a)-(d) are 355.5 and 352.5 THz, but $S_1(\nu)$ and $S_2(\nu)$ have a common spectral width given by the full width 8.6 THz at half-maximum. Figures 3.8(a) and 3.8(b) are plotted for three different ζ_o under the condition that $\Delta\zeta = 0.04$ mm, $\Delta\nu = 3.0$ THz and $R(\nu_1, \nu_2) = 0.5$. Since the distance between the two point sources $\Delta\zeta$ is fixed, no change in $|\mu|$ results, as mentioned above, whereas $\arg\mu$ shifts upward, as a whole, along the vertical axis as ζ_o takes larger values, thus keeping the two point sources at a constant separation distance. Figures 3.8(c) and 3.8(d) are plotted for the situation in which the two point source separation $\Delta\zeta$ takes three values for the fixed parameters $\zeta_o = 0$ mm, $\Delta\nu = 3.0$ THz, and $R(\nu_1, \nu_2) = 0.5$. An appreciable change in $|\mu|$ appears, and the three curves of $\arg\mu$ cross at $\nu_o = 352$ THz, which gives us $S_1(\nu_o) = S_2(\nu_o)$. As can be seen from Figs. 3.8(c) and 3.8(d), $\nu_o = 352$ THz also always gives the minimum of $|\mu|$. Apart from Fig. 3.8(c), it can be recognized that the minimum of $|\mu|$ at 352 THz varies periodically between 0 and

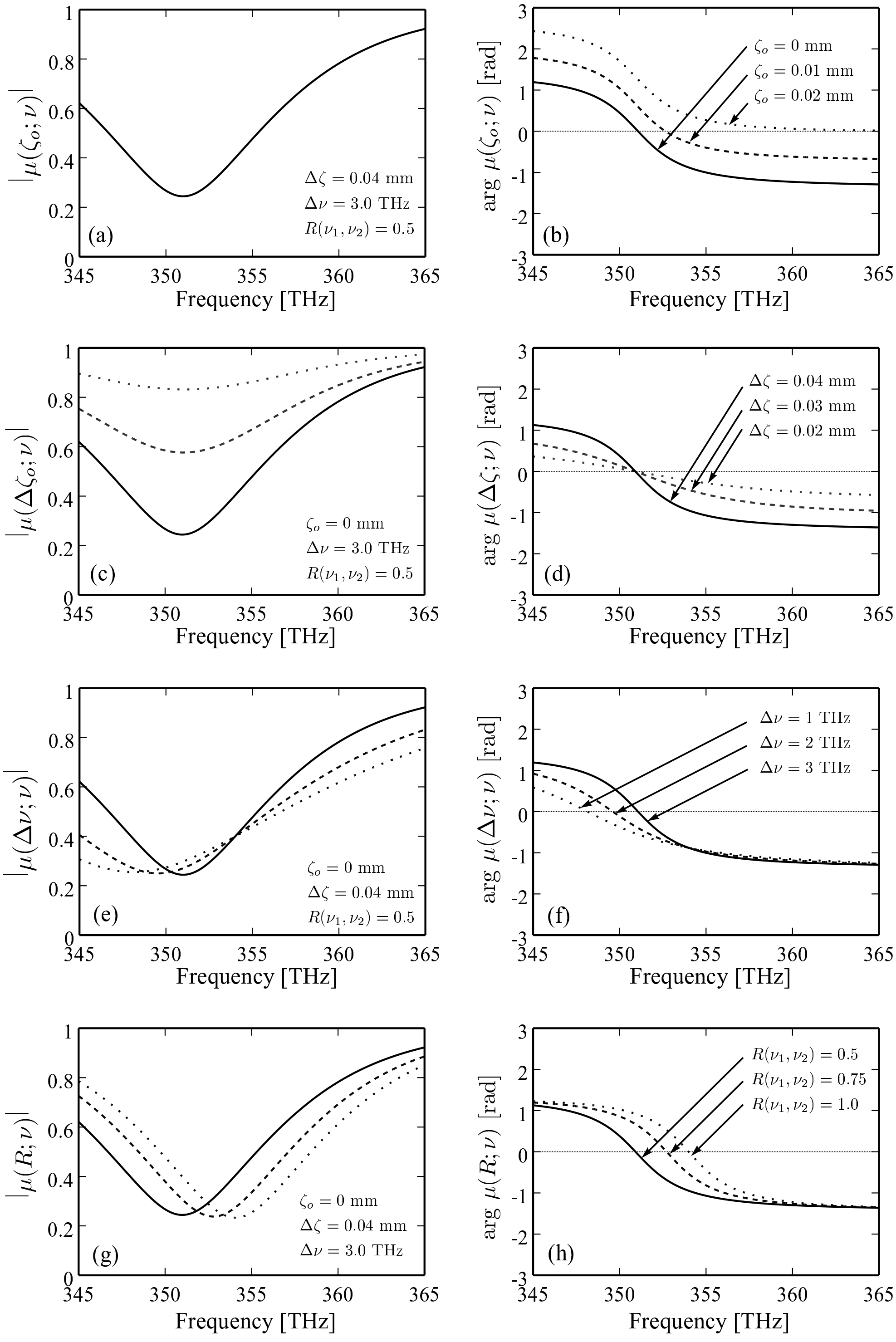

Fig. 3.8. Numerically computed results of $|\mu(\Delta\xi;\nu)|$ and $\arg\mu(\Delta\xi;\nu)$. The numerical values for the parameters ζ_o, $\Delta\zeta$, $\Delta\nu$ and $R(\nu_1,\nu_2)$ are denoted in each figure. A set of three parameters fixed for computing is given in each of the left-hand figures.

1 as $\Delta\zeta$ increases in separation. In Figs. 3.8(e)-(h), the location of the two point sources is fixed symmetrically by setting $\zeta_o = 0$ mm and $\Delta\zeta = 0.04$ mm, but their spectral peaks are situated at different frequencies, characterized by the two factors $\Delta\nu = \nu_1 - \nu_2$ and $R(\nu_1, \nu_2) = S_1(\nu_1)/S_2(\nu_2)$. Figures 3.8(e) and 3.8(f) show the case in which $\Delta\nu$ takes three different values at the fixed parameters $\zeta_o = 0$ mm, $\Delta\zeta = 0.04$ mm and $R(\nu_1, \nu_2) = 0.5$. The minimum of $|\mu|$ still remains unchanged for the three different values of $\Delta\nu$, but a particular frequency ν_o that results in the minimum of $|\mu|$ decreases as $\Delta\nu$ becomes larger. Note that each of the frequencies $\nu_o = 352$, 349 and 346 THz in Fig. 3.8(e), which gives the minima of $|\mu|$ satisfies $S_1(\nu_o) = S_2(\nu_o)$. Also, each ν_o has a different value in Fig. 3.8(e), corresponding to the three values of $\Delta\nu$. Alternatively, all the curves of $\arg\mu$ approach the definite value -0.9 around the midfrequency $(\nu_1 + \nu_2)/2 = 354$ THz. For three different ratios $R(\nu_1, \nu_2) = 0.5$, 0.75 and 1.0, $|\mu|$ and $\arg\mu$ are shown in Figs. 3.8(g) and 3.8(h). As in Fig. 3.8(e), the minimum of $|\mu|$ in 3.8(g) remains unchanged for three values of $R(\nu_1, \nu_2)$ but increases as $R(\nu_1, \nu_2)$ takes larger values; however, $|\mu|$ itself is apparently different from what is was in Fig. 3.8(e). The three curves of $\arg\mu$ in Fig. 3.8(h) changes from 1.3 to -1.3 symmetrically to the line of $\arg\mu = 0$ as ν increases in the frequency range used. The numerical results shown in Fig. 3.8 tell us that μ across the secondary source plane depends strongly not only on the location but also on the spectral difference of the two point primary sources. Accordingly, it may be that any state of μ across the secondary source plane is created in the framework of adjusting the location of the primary two point sources with variant spectra. Such μ thereby enables us to investigate experimentally and theoretically the correlation-induced spectral changes that are due to two-beam interference in the space-frequency domain.

3.3.2 Measurements of spectral coherence

First, the method to measure the spectral degree of coherence $\mu(\Delta\xi;\nu)$ is presented. The experimental setup for the measurement is shown in Fig. 3.9. The straight line $\overline{OO'A}$ denotes the optical axis. The tip of the SLD used as a primary source was so small that it could be regarded as a point source. Two SLDs are located as uncorrelated sources at ζ_1 and ζ_2, which were generally asymmetric to the optical axis. The wavefields from ξ_1 and ξ_2, $(\xi_2 = -\xi_1)$, propagated through a Kösters prism, are folded to form a superposed image at $P(x)$ in the image plane by use of an image-forming lens with a magnification factor of 1. A thin uniform phase plate inserted in the front of half the base of the Kösters prism supplies the carrier frequency to the interference term of the observed spectrum. This carrier frequency, yielding a channeled spectrum, greatly helps us to obtain $\arg\mu(\Delta\xi;\nu)$. The channeled spectrum is received by an optical fiber probe linked to a spectrum analyzer. The two point separation $\Delta\xi = \xi_1 - \xi_2$ across the secondary source is simply varied by setting the fiber probe at a required location along the x axis. The emitted spectra of the two SLDs are shown in Fig. 3.10: $S_1(\nu)$ and $S_2(\nu)$ differ from each other but have almost the same Gaussian spectrum, and their peak frequencies are $\nu_1 = 355.5$ THz for $S_1(\nu)$ and $\nu_2 = 352.5$ THz for $S_2(\nu)$. That is, $\Delta\nu = 3.0$ THz.

The spectrum taken at $P(x)$ can be written in the form[81]

$$\begin{aligned} S(x;\nu) &= S^+(x;\nu) + S^-(x;\nu) + 2|\mu(\Delta\xi;\nu)||\mu_T(\Delta\xi;\nu)|[S^+(x;\nu)S^-(x;\nu)]^{1/2} \\ &\times \cos[\nu\tau + \arg\mu(\Delta\xi;\nu) + \arg\mu_T(\Delta\xi;\nu)]\,, \end{aligned} \tag{3.42}$$

where $S^+(x;\nu)$ and $S^-(x;\nu)$ are the spectra obtained from the location ξ_1 and ξ_2; $\mu_T(\Delta\xi;\nu)$ represents a normalized cross-spectral transmittance caused by all effects in the interferometer; and τ is a time delay introduced by the thin phase plate between

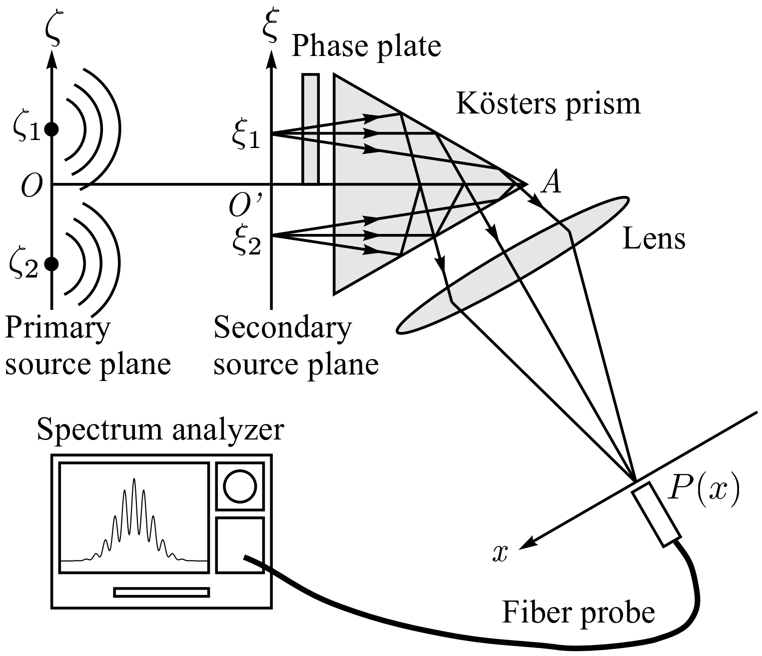

Fig. 3.9. Schematic of the measurement system of μ.

the two interfering beams. Once $|\mu_T(\Delta\xi;\nu)|$ and $\arg\mu_T(\Delta\xi;\nu)$ are determined from an *a priori* calibration made by setting only one SLD at the origin $\zeta = 0$, μ can be obtained from the following equations:

$$|\mu(\Delta\xi;\nu)| = \mathrm{env}[V(x;\nu)]\,, \tag{3.43}$$

$$\arg\mu(\Delta\xi;\nu) = \cos^{-1}\left[\frac{V(x;\nu)}{|\mu|}\right] - \cos^{-1}\left[\frac{V_T(x;\nu)}{|\mu_T|}\right]\,, \tag{3.44}$$

where env means the envelope of the function and

$$V(x;\nu) = \frac{S(x;\nu) - [S^+(x;\nu) + S^-(x;\nu)]}{2|\mu_T(\Delta\xi;\nu)|[S^+(x;\nu)S^-(x;\nu)]^{1/2}}, \tag{3.45}$$

$$V_T(x;\nu) = \frac{S(x;\nu) - [S^+(x;\nu) + S^-(x;\nu)]}{2[S^+(x;\nu)S^-(x;\nu)]^{1/2}}. \tag{3.46}$$

The spectra $S(x;\nu)$, $S^+(x;\nu)$ and $S^-(x;\nu)$ taken at $P(x)$ are shown together in Fig. 3.11.

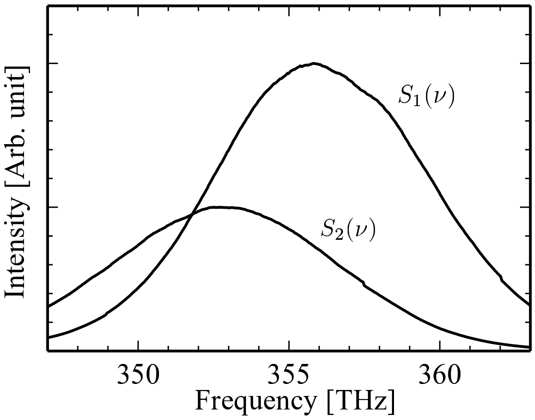

Fig. 3.10. Two SLDs spectra show $S_1(\nu)$ and $S_2(\nu)$ used in the primary source. Their profiles are almost Gaussian.

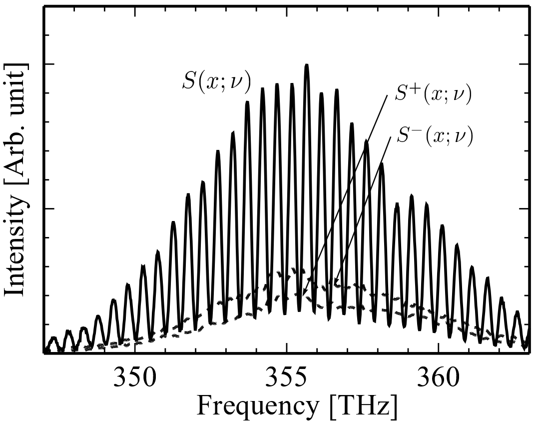

Fig. 3.11. Three spectra $S(x;\nu)$, $S^+(x;\nu)$ and $S^-(x;\nu)$ measured at $P(x)$.

With reference to Eq. (3.45), three measured spectra $S(x;\nu)$, $S^+(x;\nu)$ and $S^-(x;\nu)$ allow us to obtain $V(x;\nu)$ after the calibration. For example, $V(x;\nu)$ at $x = \Delta\xi = 0.4$ mm is shown in Fig. 3.12. With the help of Eqs. (3.43) and (3.44), the curves of $|\mu(\Delta\xi;\nu)|$ and $\arg\mu(\Delta\xi;\nu)$ computed with three values of ζ_o are shown, respectively, in Figs. 3.13(a) and 3.13(b). The values of the parameters used, except for $\Delta\zeta$, were $\zeta_o = 0$ mm, $\Delta\nu = 3.0$ THz and $R(\nu_1,\nu_2) = 0.5$. As mentioned in Figs. 3.8(c)

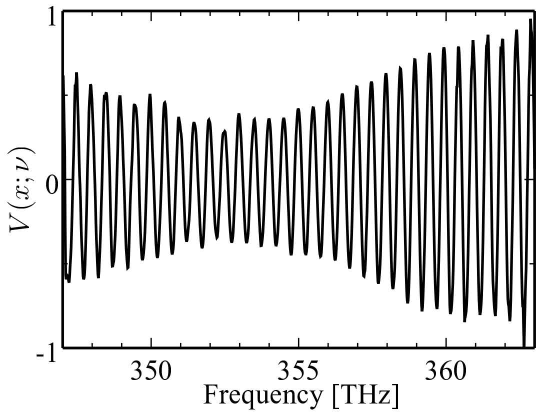

Fig. 3.12. $V(x;\nu)$ obtained from three measured $S(x;\nu)$, $S^{+}(x;\nu)$ and $S^{-}(x;\nu)$.

and 3.8(d), the minima of three $|\mu|$'s are almost the same at $\nu_o = 352$ THz, and three $\arg\mu$'s cross also at 352 THz. It should be kept in mind that this 352 THz is in agreement with the frequency ν_o at which the profile of $S_1(\nu)$ crosses that of $S_2(\nu)$, as shown in Fig. 3.10. In general, ν_o does not coincide with the mid-frequency $(\nu_1+\nu_2)/2$ because the peak values of $S_1(\nu_1)$ and $S_2(\nu_2)$ are different from each other, but ν_o becomes equal to $(\nu_1+\nu_2)/2$ only when $S_1(\nu_1) = S_2(\nu_2)$.

Let the spectrum in the secondary source plane be expressed as $S_S(\nu)$, that is, spatially uniform across the ξ axis because the illumination by the two SLDs are spatially uniform. As a result, putting $\Delta\xi = 0$ in Eq. (3.33) readily leads us to

$$W(\Delta\xi = 0;\nu) = S_S(\nu) = \left(\frac{\nu}{cz}\right)^2 [S_1(\nu) + S_2(\nu)] \ . \tag{3.47}$$

With reference to Eq. (3.36), we restrict ourselves to a situation in which $|\mu(\Delta\xi;\nu')|$ changes periodically as a function of $\Delta\xi$ at a particular frequency ν', depending on the respective spectral densities of the two point sources at the frequency ν'. In Figs. 3.14(a) and 3.14(b) $|\mu(\Delta\xi;\nu')|$ and $\arg\mu(\Delta\xi;\nu')$ are shown with $\Delta\zeta = 0.04$ mm at two frequencies $\nu' = 352$ and 356 THz. Remember that the profile of $S_1(\nu)$ crosses

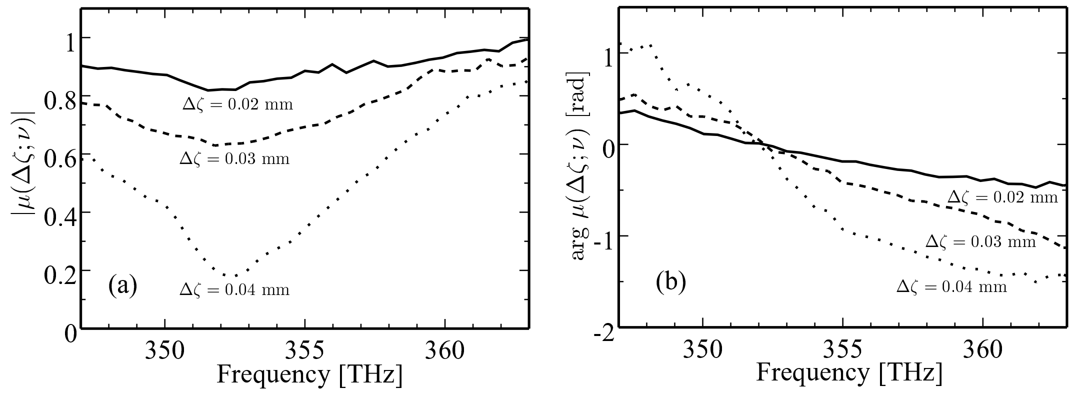

Fig. 3.13. (a) Measured and computed $|\mu(\Delta\xi;\nu)|$ for three values of $\Delta\zeta$. (b) Measured and computed $\arg\mu(\Delta\xi;\nu)$ for the same values of $\Delta\zeta$'s as in (a).

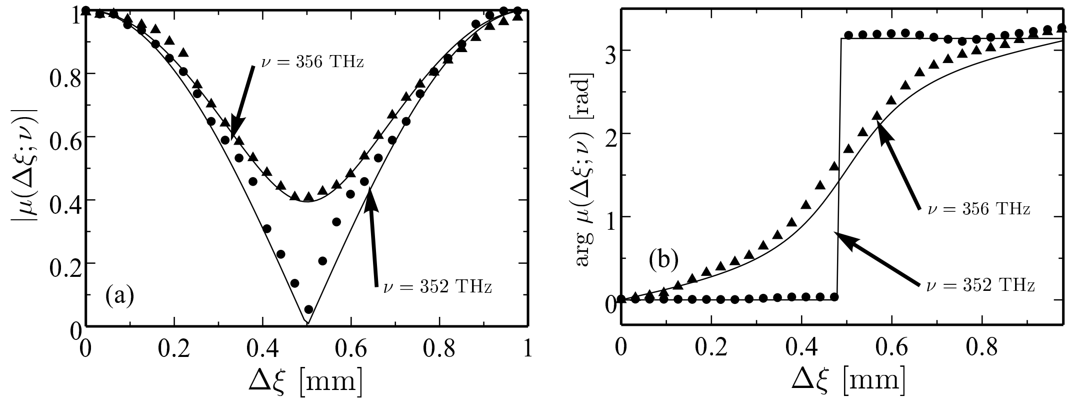

Fig. 3.14. Dependence of μ on $\Delta\xi$. $|\mu|$ and $\arg\mu$ are plotted in (a) and (b), respectively, for $\nu = 352$ and 356 THz with fixed parameters $\zeta_o = 0$ mm, $\Delta\zeta = 0.04$ mm, $\Delta\nu = 3.0$ THz and $R(\nu_1,\nu_2) = 0.5$.

that of $S_2(\nu)$ at 352 THz in Fig. 3.10. If $\Delta\xi$ is extended beyond $\Delta\xi = 1$ mm in Fig.3.10(a), the curves of $|\mu|$ will change periodically as pointed out above. It should be noted that the minimum values of two $|\mu|$'s are 0 and 0.4 for $\nu' = 352$ and 356 THz, respectively, and the minimum value of $|\mu|$ can be determined uniquely by the ratio $S_1(\nu')/S_2(\nu')$ as understood from Eq. (3.36).

As pointed out theoretically in Subsection 3.3.1, it has been proven experimentally that a wide variety of μ can be created across the secondary source plane as a function of frequency by adjusting the location and separation of the primary two point sources with variant Gaussian-like spectra.

3.3.3 Observations of correlation-induced spectral changes

We showed in Subsection 3.3.2 that μ can be successfully measured by introducing the carrier frequency into the interference term. The measured μ enables us to explore the correlation-induced spectral changes that are due to two-beam interference in the space-frequency domain by removing the phase plate from the interferometer. After making an *a priori* calibration to determine $|\mu_T|$ and $\arg \mu_T$, we can write the spectrum measured at $P(x)$ on the imaging axis, referring to Eq. (3.42), in the form,

$$\begin{aligned} S(x;\nu) &= S^+(x;\nu) + S^-(x;\nu) \\ &+ 2|\mu(\Delta\xi;\nu)|[S^+(x;\nu)S^-(x;\nu)]^{1/2}\cos[\arg\mu(\Delta\xi;\nu)] \, . \end{aligned} \tag{3.48}$$

As mentioned above, the spatial uniformity of the spectrum must be guaranteed across the secondary source plane, and the wavefront folding imaging system is, in addition, assumed to be so lossless that the uniform spectrum across the secondary source plane, given by $S_S(\nu) = S^+(x;\nu) + S^-(x;\nu)$, is independent of x. Note that $S_S(\nu)$ is experimentally obtainable because $S^+(x;\nu)$ and $S^-(x;\nu)$ can be separately measured by closing in turn each of the two beams arriving at $P(x)$.

The experiments to observe the spectral changes were done with reference to the parameters used to represent Figs. 3.8(a)-(h). The measured results are given in Fig. 3.15. Figure 3.15(a) shows $S_S(\nu)$ and $S(x;\nu)$; the spectral profiles of $S(x;\nu)$ are traced in such a way that $\mu(\Delta\xi;\nu)$ depends only on the parameter ζ_o, correspond-

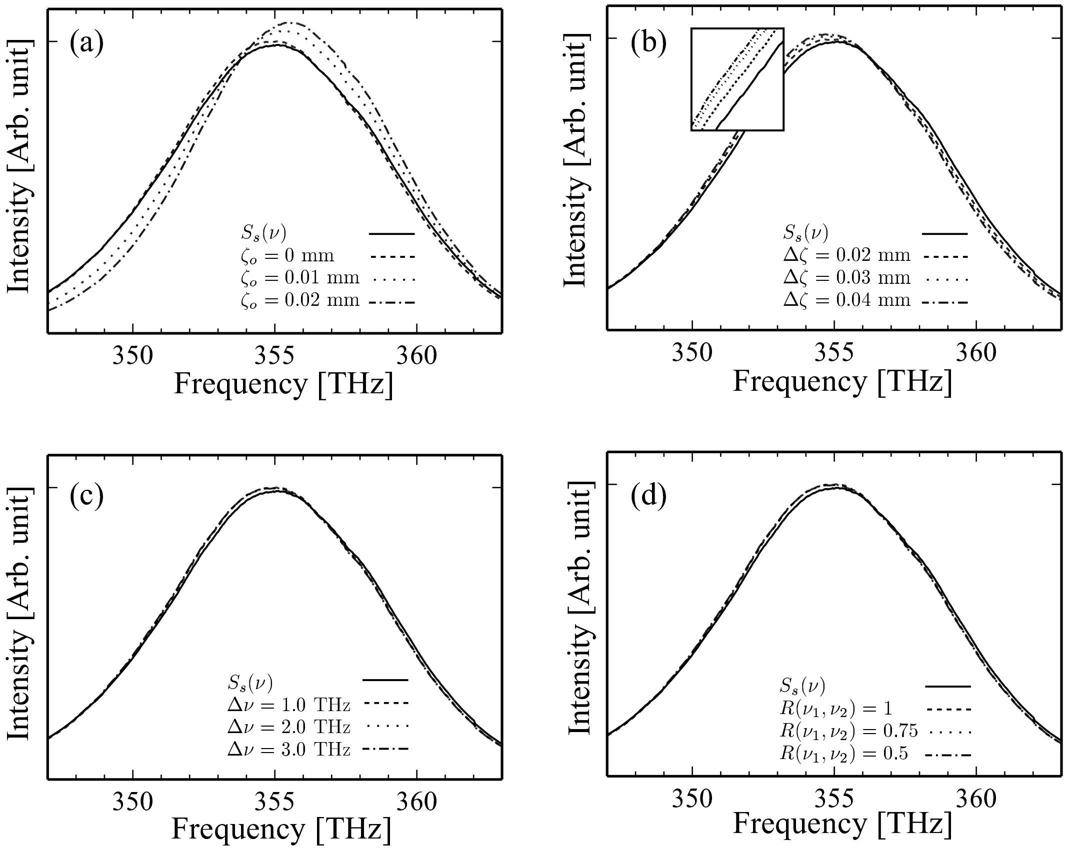

Fig. 3.15. Observed spectra $S_S(\nu)$ and $S(x;\nu)$. The solid curves represents $S_S(\nu)$, and the three kinds of dotted curves represent $S(x;\nu)$. The fixed parameters for the measurements are (a) $\Delta\zeta = 0.04$ mm, $\Delta\nu = 3.0$ THz and $R(\nu_1,\nu_2) = 0.5$ (b) $\zeta_o = 0$ mm, $\Delta\nu = 3.0$ THz and $R(\nu_1,\nu_2) = 0.5$ (c) $\zeta_o = 0$ mm, $\Delta\zeta = 0.04$ mm and $R(\nu_1,\nu_2) = 0.5$ (d) $\zeta_o = 0$ mm, $\Delta\zeta = 0.04$ mm and $\Delta\nu = 3.0$ THz.

ing to Figs. 3.8(a) and 3.8(b). Remember that ζ_o is the midpoint of the two point sources in the primary source plane. As can be seen from Fig. 3.15(a), the profiles of observed spectra shift toward the higher frequency (blueshift). The spectral profiles of Figs. 3.15(b)-(d) are traced, respectively, by use of the parameters $\Delta\zeta$, $\Delta\nu$ and $R(\nu_1,\nu_2)$, and are compared with $S_S(\nu)$. Every parameter takes three different values against the other fixed parameters. Evidently, the spectral changes in Figs. 3.15(b)-(d) are appreciably less than in Fig. 3.15(a).

3.3.4 discussion

In order to discuss more quantitatively how the spectrum $S(x;\nu)$ observed at the image plane differs from the spectrum $S_S(\nu)$ in the secondary source plane, we introduce the spectral modulation factor M, and rewrite Eq. (3.48) into the form

$$S(x;\nu) = S_S(\nu)\,[1 + M(x,\Delta\xi;\nu)] \ , \tag{3.49}$$

where

$$M(x,\Delta\xi;\nu) = \frac{2[S^{+}(x;\nu)S^{-}(x;\nu)]^{1/2}}{S_S(\nu)} |\mu(\Delta\xi;\nu)| \cos[\arg\mu(\Delta\xi;\nu)] \,. \tag{3.50}$$

It is understood from Eq. (3.49) that the spectral change that is due to two-beam interference always occurs as long as M has an appreciable frequency dependence over the frequency range of concern. In other words, the correlation-induced spectral changes are dependent primarily of $M(x,\Delta\xi;\nu)$, which is represented by the product of $|\mu|$, $\cos(\arg\mu)$ and $[S^{+}(x;\nu)S^{-}(x;\nu)]^{1/2}/S_S(\nu)$.

Figure 3.16 shows the curves of M computed with the same values of the parameters as used in Fig. 3.15; The three curves in Fig. 3.16(a) correspond to those in Fig. 3.15(a). The curve for $\zeta_o = 0$ is almost flat in the frequency range used, but the other two curves for $\zeta_o = 0.01$ and 0.02 mm increase as a function of frequency. This variation induces the asymmetric spectral changes in Fig. 3.15(a). These curves for M at three different $\Delta\zeta$'s at $\zeta_o = 0$ mm are shown in Fig. 3.16(b). Three curves are almost flat but quite separated from one another. As may be seen from Fig. 3.16(b), the fact that M is almost independent of frequency in this case does not cause any

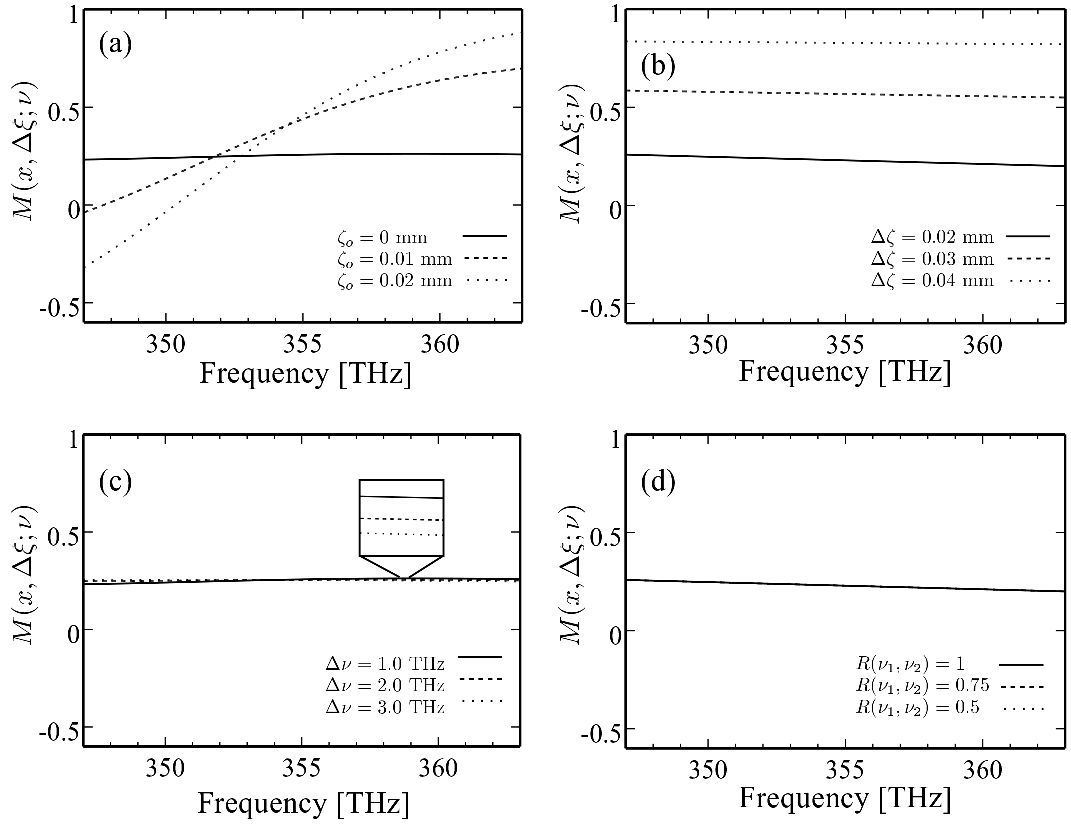

Fig. 3.16. Spectral modulation factors $M(x, \Delta\xi; \nu)$ with the same parameters as in Fig. 3.15.

asymmetric spectral change, as is evident from Eq. (3.49). Unlike Figs. 3.16(a) and 3.16(b), an appreciable small change occurs in Figs. 3.16(c) and 3.16(d). This means that the spectral change does not depend appreciably on M. In fact, no spectral change appears in the case in that $\Delta\nu$, and $R(\nu_1, \nu_2)$ take different values, as shown in Figs. 3.15(c) and 3.15(d). As mentioned in Subsection 3.3.2, the asymmetric spectral changes are fairly dependent on the frequency-dependent behavior of arg μ. Still more generally, however, the frequency dependence of M plays a critical role in inducing the spectral change, as represented in Figs. 3.16(a)-(d) in association with the corresponding parts Fig. 3.15. In particular, the asymmetric change in M versus the central frequency of $S_S(\nu)$ is the major cause of the spectral change. Note carefully that since all the computed and measured values of $\arg\mu$ in Figs. 3.8 and 3.13(b) are considerably smaller than $\pm\pi$, the interference term $\cos(\arg\mu)$ does not exhibit a periodic variation as a function of ν. That is why any sinusoidal variation has not appeared on $S(x;\nu)$.

3.4 Conclusion

The correlation-induced spectral changes were studied theoretically and experimentally in this chapter. In Section 3.2, the effects of both the source correlation and the dispersive diffraction on the spectral changes were investigated. The peak shifts in the Gaussian spectrum were observed dependent on the ratio of the coherence area to the source area. In the coherent limiting case, the spectral change was caused by the dispersive diffraction, whereas no spectral change was observed in the incoherent limiting case. When the source fields were spatially partially coherent, both the source correlation and the dispersive diffraction affected the change in spectrum. For measuring the spectral change that is caused by only the source correlation, the experiment with the wavefront folding interferometer was conducted, and the results and discussions were presented in Section 3.3. The location and the spectra of the uncorrelated two point sources realized the various spatial coherence properties over the secondary source plane. The relationship between the spectral changes and the source correlation was thus quantitatively investigated. The experimental results well agreed with the theoretical expectations.

Chapter 4

Retrieval of 2-D image and spectrum distribution

4.1 Introduction

While the nature of the correlation-induced spectral changes that was studied in Chapter 3 comes from the problem of the forward propagation of the spatial coherence, the interferometric imaging technique is closely related to the inverse propagation of the spatial coherence function. The interferometric imaging techniques have long been used in practical observations such as radio astronomy.[70]

In this chapter, new two-dimensional interferometric imaging techniques are presented. First, a new principle for determining an angular separation and spectra of uncorrelated two point sources is given. The principle is based on the van Cittert-Zernike theorem. Since the two-dimensional intensity distribution is retrieved from the measured mutual intensity of the quasi-monochromatic wavefields, source spectra can be determined from the spectral coherence function of the wavefields with the wide spectral bandwidth. The experimental demonstration is conducted using the wavefront folding image-forming system which was presented in Chapter 3. The second principle is based on the propagation law of the angular spectrum of the wavefield in free space. It is well known that the propagation law of the angular spectrum is represented by means of the simple transmission function as represented in Eq. (2.42). This implies that the plane wave propagates with varying only its phase but conserving the amplitude. This description of the wave propagation is obviously derived without the paraxial approximation. The propagation law of the cross-spectral density described in the spatial-frequency domain was also established a long time ago. However, no attempt was ever made to apply the propagation law to the interferometric imaging techniques. This may be because of the difficulty of measuring the field correlation for all pairs of points within an observation area, and the troublesome repetition of Fourier procedures. However, recent publications dealing with measuring and displaying the mutual intensity[67, 68] and developments in computing systems will facilitate employing the propagation law in the spatial-frequency domain. Full theoretical description and results of the experimental demonstration for this interferometric imaging technique are also presented.

4.2 Determination of angular separation and spectra of two point sources

4.2.1 Formulation of principle

We assume uncorrelated point sources that are not known in location and spectral profile, but are assumed to lie far enough from an observer. Under these circumstances, the objective of this section is to give a principle that enables us to determine not only the angular separation but also spectral profiles of the two point sources. The first step is to derive an expression for the cross-spectral density propagating from the sources to an area around the observer. The second step is taking the Fourier inversion of the spectral degree of coherence μ, which provides the theoretical foundation for the experiments.

We now begin with the illustration of the geometrical system involving the two point sources and the observer. With reference to Fig. 4.1, the location where the observer looks at the two point sources is designated to be the origin O of the Cartesian coordinates (x, y, z). On the assumption that the two point sources lie at $P_1(x_1, 0, z_1)$ and $P_2(x_2, 0, z_2)$, their separation angle of concern is $\theta = \angle P_1 O P_2$. Here it should be noted that the line pointing from P_1 to P_2 cannot be determined uniquely in advance, since the source locations P_1 and P_2 are unknown in generall. Therefore, the x axis through O cannot also be readily determined but must be searched for.

Here let us consider how to determine the direction of the x axis. According to Section 3.3, the wavefront folding interferometer with a Kösters prism is useful for measuring μ, as shown in Fig. 4.2. Go back to Fig. 4.1, and the base of the Kösters prism is put along the ξ axis passing through the common origin O, which forms the different Cartesian coordinates (ξ, η, z). The separation angle θ which will be determined from the measured μ takes a maximum when the ξ axis coincides with the x axis, as will be mentioned below. Thus some trials for arranging the Kösters prism make it possible to find the x axis correctly.

We proceed to formulate the cross-spectral density $W(\xi, -\xi; \nu)$ with respect to symmetric points $(\xi, -\xi)$ on the ξ axis. Let us assume that the x axis is turned by an angle ϕ from the ξ axis around the z axis, and the locations of the two point sources designated by the (ξ, η) coordinate system are denoted, respectively, by $P_1(\xi_1, \eta_1, z_1)$ and $P_2(\xi_2, \eta_2, z_2)$, where

$$\left.\begin{aligned} \xi_1 &= x_1 \cos\phi, & \eta_1 &= -x_1 \sin\phi \\ \xi_2 &= x_2 \cos\phi, & \eta_2 &= -x_2 \sin\phi \end{aligned}\right\} . \tag{4.1}$$

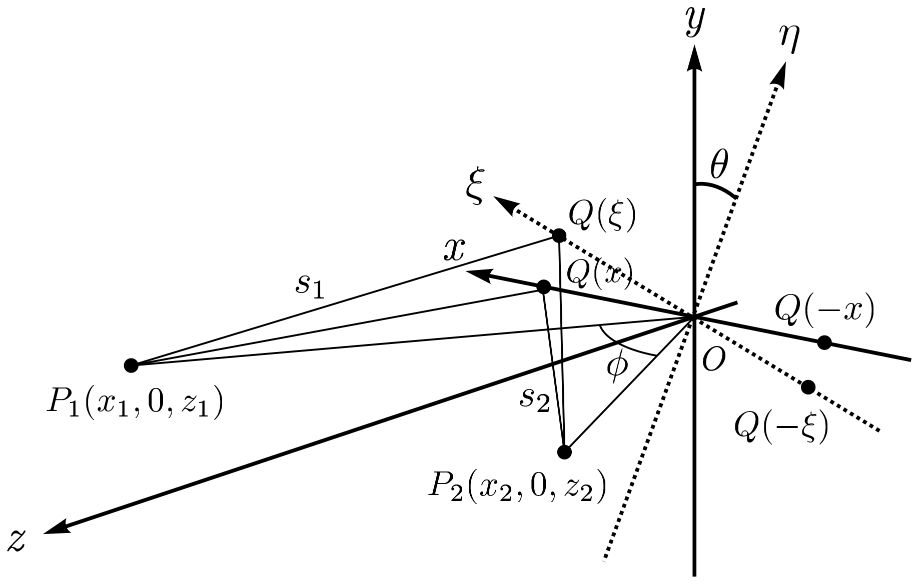

Fig. 4.1. Geometry for two point sources and an observer.

Consider a point $Q(\xi)$ on the ξ axis, and the transmission functions at a particular frequency ν from P_1 and P_2 to Q in the framework of paraxial approximation may be written, respectively, by

$$H(P_1, Q; \nu) = \frac{i\nu \exp(-2\pi i \nu s_1/c)}{cs_1}, \tag{4.2}$$

$$H(P_2, Q; \nu) = \frac{i\nu \exp(-2\pi i \nu s_2/c)}{cs_2}, \tag{4.3}$$

where s_1, s_2 are the distances from P_1 and P_2 to Q. The optical frequency components of the analytic signals at P_1 and P_2 are written, respectively, by $U_s(\xi_1, \eta_1, z_1; \nu)$ and $U_s(\xi_2, \eta_2, z_2; \nu)$ in terms of the (ξ, η, z) coordinate system.

Since there exist only the two point sources, the optical frequency component at $Q(\xi)$ may be written as

$$U_Q(\xi; \nu) \;=\; \iint_{-\infty}^{\infty} U_s(\xi, \eta, z; \nu)\delta(\xi - \xi_1, \eta - \eta_1)H(P_1, Q; \nu)d\xi d\eta$$

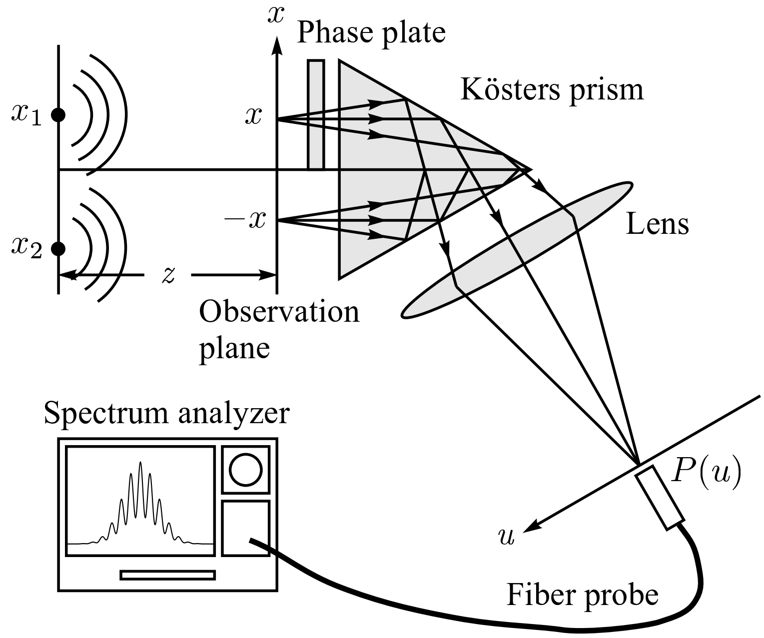

Fig. 4.2. Optical system for measuring μ.

$$
\begin{aligned}
&+ \iint_{-\infty}^{\infty} U_s(\xi,\eta,z;\nu)\delta(\xi-\xi_2,\eta-\eta_2)H(P_2,Q;\nu)d\xi d\eta \\
&= U_s(\xi_1,\eta_1,z_1;\nu)H(P_1,Q;\nu)+U_s(\xi_2,\eta_2,z_2;\nu)H(P_2,Q;\nu)\,. \qquad (4.4)
\end{aligned}
$$

Hence use of Eqs. (4.2)-(4.4) gives directly the cross-spectral density,

$$
\begin{aligned}
W(\xi,-\xi;\nu) &= \langle U_Q^*(\xi;\nu)U_Q(-\xi;\nu)\rangle \\
&= \left(\frac{\nu}{cz_1}\right)^2 S_{P1}(\nu)\exp\left(\frac{2\pi i\nu\xi_1\Delta\xi}{cz_1}\right)+\left(\frac{\nu}{cz_2}\right)^2 S_{P2}(\nu)\exp\left(\frac{2\pi i\nu\xi_2\Delta\xi}{cz_2}\right)\,, \qquad (4.5)
\end{aligned}
$$

where $\Delta\xi = \xi-(-\xi) = 2\xi$ is the distance between $Q(\xi)$ and $Q(-\xi)$ on the ξ axis. Here $S_{P1}(\nu)$, $S_{P2}(\nu)$ are the respective spectra of the two point sources defined by

$$
\left.\begin{aligned}
S_{P1}(\nu) &= \langle|U(\xi_1,\eta_1;\nu)|^2\rangle \\
S_{P2}(\nu) &= \langle|U(\xi_2,\eta_2;\nu)|^2\rangle
\end{aligned}\right\}\,. \qquad (4.6)
$$

The spectral degree of coherence is defined as

$$
\mu(\xi,-\xi;\nu) = \frac{W(\xi,-\xi;\nu)}{[W(\xi,\xi;\nu)W(-\xi,-\xi;\nu)]^{1/2}}
$$

$$= \frac{(\nu/c)^2}{S_o(\nu)} \left[\frac{S_{P1}(\nu)}{z_1^2} \exp\left(\frac{2\pi i\nu\xi_1\Delta\xi}{cz_1}\right) + \frac{S_{P2}(\nu)}{z_2^2} \exp\left(\frac{2\pi i\nu\xi_2\Delta\xi}{cz_2}\right)\right] , \tag{4.7}$$

where

$$S_o(\nu) = W(\xi,\xi;\nu) = W(-\xi,-\xi;\nu) = \left(\frac{\nu}{cz_1}\right)^2 S_{P1}(\nu) + \left(\frac{\nu}{cz_2}\right)^2 S_{P2}(\nu) , \tag{4.8}$$

is a uniform spectrum measurable on the ξ axis.

We now look for the direction of the x axis by turning the ξ axis around the z axis, which is implemented by making a stepwise rotation of the base of the Kösters prism around the z axis. The measurement of μ is made at every stepwise rotation. It is understood that we can obtain $\xi_1 = \xi_2 = 0$ if the ξ coordinates of the two point sources are located at $\phi = 90°$, as can be understood from Eq. (4.1). This situation implies that the x and ξ axes are arranged to be perpendicular with each other. In other words, the base of the Kösters prism crosses the x axis at right angles. This condition that $\xi_1 = \xi_2 = 0$ at $\phi = 90°$ always enables us to have $\mu = 1$ for any distance $\Delta\xi$, as understood from Eq. (4.7). Such a completely coherent condition results in the maximum visibility over the channeled spectrum measured by scanning optical frequency in a spectrometer. It follows that the rotation of the ξ axis by 90° from that situation gives rise to the exact x axis.

Finally, we obtain at two points $Q(x)$ and $Q(-x)$ by making the ξ axis align with the x axis,

$$\mu(x,-x;\nu) = \frac{(\nu/c)^2}{S_o(\nu)} \left[\frac{S_{P1}(\nu)}{z_1^2} \exp\left(\frac{2\pi i\nu x_1\Delta x}{cz_1}\right) + \frac{S_{P2}(\nu)}{z_2^2} \exp\left(\frac{2\pi i\nu x_2\Delta x}{cz_2}\right)\right]. \tag{4.9}$$

This is the theoretical foundation for measuring μ. Now we are in a position to derive the principle to determine not only the angular separation of the two point sources but also each spectral profile from both measured μ and $S_o(\nu)$. The inverse Fourier transform of Eq. (4.9) with respect to Δx at a particular frequency ν_p is

$$\begin{aligned}
&\int_{-\infty}^{\infty} \mu(x,-x;\nu)\exp(2\pi i\nu x\Delta x/cz)d(\Delta x)\\
&\quad= \frac{(\nu_p/cz_1)S_{P1}(\nu_p)}{S_o(\nu_p)}\int_{-\infty}^{\infty}\exp\left(\frac{2\pi i\nu_p x_1\Delta x}{cz_1}\right)\exp\left(\frac{2\pi i\nu_p x\Delta x}{cz_1}\right)d(\Delta x)\\
&\quad+\frac{(\nu_p/cz_2)S_{P1}(\nu_p)}{S_o(\nu_p)}\int_{-\infty}^{\infty}\exp\left(\frac{2\pi i\nu_p x_2\Delta x}{cz_2}\right)\exp\left(\frac{2\pi i\nu_p x\Delta x}{cz_2}\right)d(\Delta x)\\
&\quad= R_1(\nu_p)\delta\left(\frac{x-x_1}{z_1}\right)+R_2(\nu_p)\delta\left(\frac{x-x_2}{z_2}\right)\ , \qquad (4.10)
\end{aligned}$$

where

$$\left.\begin{aligned}
R_1(\nu_p) &= \frac{(\nu_p/cz_1)^2 S_{P1}(\nu_p)}{S_o(\nu_p)}\\
R_2(\nu_p) &= \frac{(\nu_p/cz_2)^2 S_{P2}(\nu_p)}{S_o(\nu_p)}
\end{aligned}\right\} . \qquad (4.11)$$

Note that x_1/z_1 and x_2/z_2 are, respectively, the angles between the z axis and lines from P_1 and P_2 to O, and the angular separation of P_1 and P_2 seen from the observer is thereby given by $\theta_p = |x_1/z_1 - x_2/z_2|$ at ν_p. The statistical processing of all the measured values of θ_p $(p = 1, 2, 3, ...)$ will result in more reliable θ. Use of the separation angle obtained allows us to determine each of spectral densities $S_{P1}(\nu_p)$ and $S_{P2}(\nu_p)$ with the help of the following modified expressions of Eq. (4.11):

$$\left.\begin{aligned}
S_{P1}(\nu_p) &= \left(\frac{cz_1}{\nu_p}\right)^2 S_o(\nu_p)R_1(\nu_p)\\
S_{P2}(\nu_p) &= \left(\frac{cz_2}{\nu_p}\right)^2 S_o(\nu_p)R_2(\nu_p)
\end{aligned}\right\} . \qquad (4.12)$$

Since the distances z_1 and z_2 are unknown in general, the ratio of $S_{P1}(\nu_p)$ with $S_{P2}(\nu_p)$ remains undetermined as long as $z_1 \neq z_2$, whereas if $z_1 = z_2$ is satisfied, the ratio takes a constant at every frequency. The successive Fourier inversions with respect to Δx at ν_p $(p = 1, 2, 3, ...)$ give a series of $R_1(\nu_p)$ and $R_2(\nu_p)$, and plotting of them at every ν_p $(p = 1, 2, 3, ...)$ finally allows us to obtain each spectral profile of $S_{P1}(\nu)$ and $S_{P2}(\nu)$.

4.2.2 Experiment and discussion

Here a simple geometrical arrangement is assumed for simplicity; the base of the Kösters prism coincide with the x axis under the condition that $z_1 = z_2 = z$. This assumption leads us to the simplified expression derived from Eqs. (4.8) and (4.9) by putting $z_1 = z_2 = z$. The two point sources are spatially incoherent, i.e., the two point sources located, respectively, at (x_1, z) and (x_2, z) illuminate independently the base of the Kösters prism. The experimental arrangement shown in Fig. 4.2 is aimed at measuring $\mu(x, -x; \nu)$ just in front of the Kösters prism. The measurement of μ is conducted based on the principle and the procedure that were described in Section 3.3.

The two point sources were simulated by incorporating two SLDs. These possessed Gaussian-like spectra with full width at half maximum of 3.0 THz, and their central frequencies were at 355.5 and 352.5 THz, respectively. The intensity ratio at the maxima was 1:2. The two SLDs were located at $x_1 = 30$ μm and $x_2 = -20$ μm at a distance $z = 50$ mm in front of the Kösters prism. The measured $|\mu(\Delta x; \nu)|$ and $\arg \mu(\Delta x; \nu)$ are shown at two particular frequencies in Figs. 4.3 (a) and (b). As mentioned above, the Fourier inversion of μ with respect to Δx at ν_p gives the angular separation $\theta = |x_1 - x_2|/z$. With reference to Eq. (4.11), R_1 and R_2 are plotted in Figs. 4.4(a) and 4.4(b). As has been expected, the same angular separation $\theta = 1.0 \times 10^{-3}$ rad is obtained from both Figs. 4.4(a) and 4.4(b). Going back to Fig. 4.3(a), it is simply understood that θ is inversely proportional to the period of $|\mu|$ when varied in Δx. This means that the minimum θ is limited to a length of the base of the Kösters prism.

A base length of 3 cm was used for the measurements, which produces approxi-

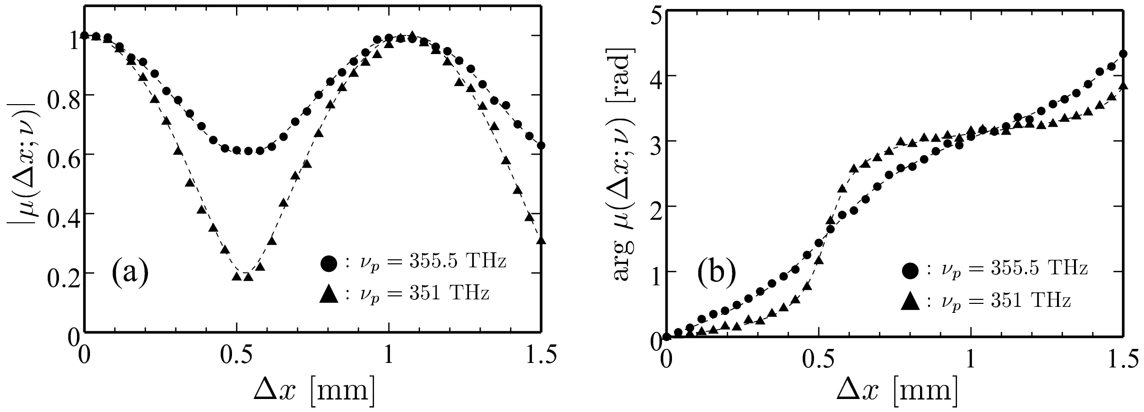

Fig. 4.3. Measured μ at two frequencies as a function of Δx. Their absolute values and arguments are plotted in (a) and (b), respectively.

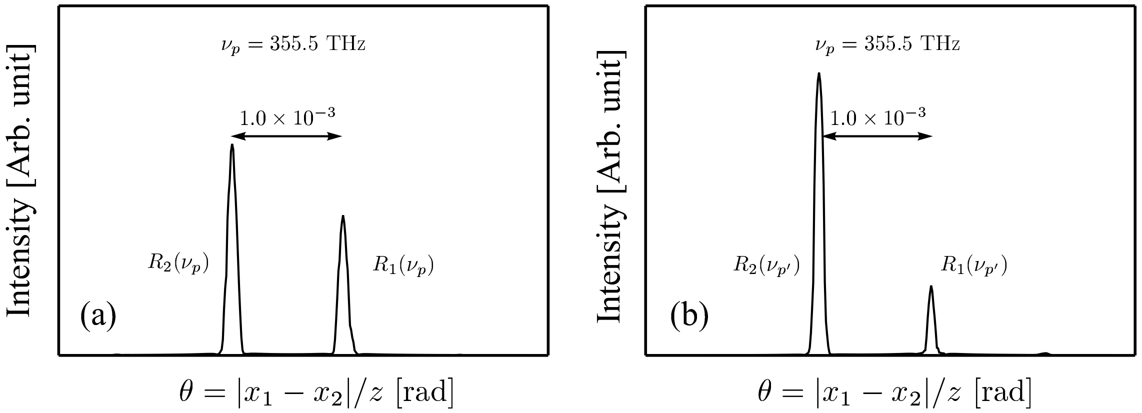

Fig. 4.4. Fourier inversions of μ at two different frequencies.

mately the minimum $\theta = 2.86 \times 10^{-5}$ rad. The Fourier inversion of μ measured at every frequency ν_p $(p = 1, 2, 3, \cdots)$ was successively made with respect to Δx, and the summation of all the Fourier inversions finally represent $R_1(\nu) = \sum_p R_1(\nu_p)$ and $R_2(\nu) = \sum_p R_2(\nu_p)$. Use of $R_1(\nu)$, $R_2(\nu)$ and $S_o(\nu)$ measured across the observation plane readily recovers each spectral profile of the two point sources (see Eq. (4.12)) as shown in Fig. 4.5. It is recognized that both smoothed profiles obtained from the

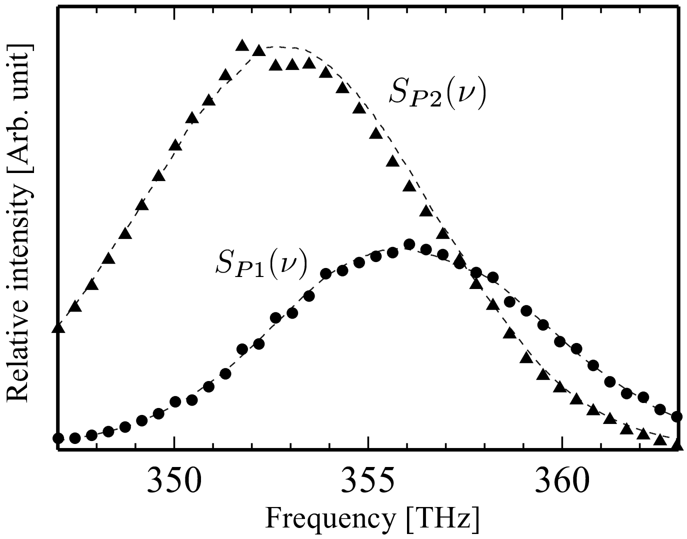

Fig. 4.5. Comparison of the recovered spectral profiles with the original ones. The plotted crosses show the spectra recovered from the measured μ, and the dotted curves represent the original spectra.

measured μ reflects well the original profiles of the two SLD spectra. Note that the ratio of the two spectral profiles takes a constant value over the frequency axis, since the distances of the two point sources from the observer were identical for the present measurements, as mentioned in Subsection 4.2.1.

4.3 Retrieval of cross-spectral density propagating in free space

4.3.1 Propagation and retrieval of cross-spectral density

In this section, a new principle of interferometric imaging based on the propagation of the angular spectra is presented. With reference to Fig. 4.6, we assume a planar, quasi-monochromatic light source on a source plane Σ_s at $z = z_s > 0$ and a wavefield propagating toward the right of the figure in free space. An observation plane Σ_o is located at $z = 0$ parallel to Σ_s. Let a particular point P at a reference plane Σ_r, which is located at $z = z_r$ in a slab geometry parallel to Σ_s and Σ_o, be specified by a three-dimensional position vector $\boldsymbol{r} = (x, y, z)$. The origin of the coordinate system is set on Σ_o. In the present case the positive direction of the z axis is opposite to the direction of the propagating light because our interest is in the inverse propagation of the cross-spectral density, and the distance from an observer to the source is, in general, assumed to be unknown.

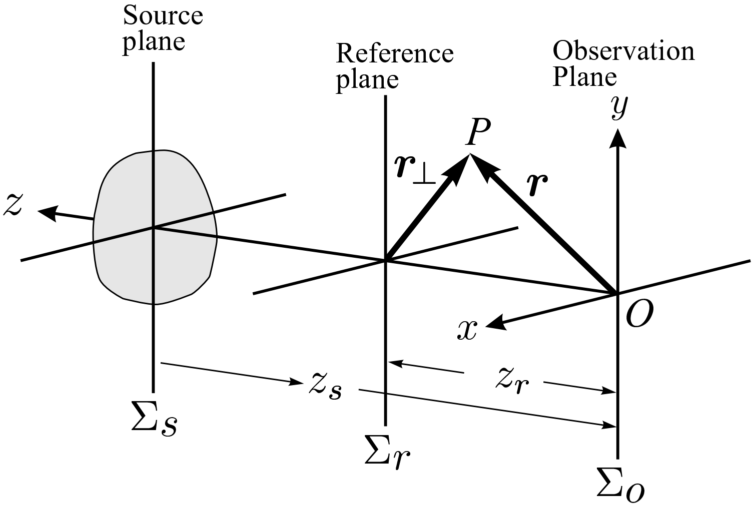

Fig. 4.6. Geometry of the optical system for the general theorem.

According to Eq. (2.46), the propagation law of the four-dimensional Fourier transform of the cross-spectral density is represented by

$$\tilde{W}^{(0)}(\boldsymbol{k}'_\perp, \boldsymbol{k}_\perp; \nu) = \exp[i(k_z - k'_z)z_r]\tilde{W}^{(z_r)}(\boldsymbol{k}'_\perp, \boldsymbol{k}_\perp; \nu). \tag{4.13}$$

For the sake of convenience, we call the Fourier transform of the cross-spectral density the *angular cross-spectral density*. From Eq. (4.13) we can readily retrieve the angular cross-spectral density across Σ_r from that across Σ_o by

$$\tilde{W}^{(z_r)}(\boldsymbol{k}'_\perp, \boldsymbol{k}_\perp; \nu) = \exp[-i(k_z - k'_z)z_r]\tilde{W}^{(0)}(\boldsymbol{k}'_\perp, \boldsymbol{k}_\perp; \nu) \, . \tag{4.14}$$

This means that the angular cross-spectral density $\tilde{W}^{(z_r)}(\boldsymbol{k}'_\perp, \boldsymbol{k}_\perp; \nu)$ across Σ_r can be reconstructed if $\tilde{W}^{(0)}(\boldsymbol{k}'_\perp, \boldsymbol{k}_\perp; \nu)$ is known or measurable across Σ_o. By using the transmission term $\exp[-i(k_z - k'_z)z_r]$ and the four-dimensional inverse Fourier transform, we can obtain the cross-spectral density across the reference plane

$$\begin{aligned} W^{(z_r)}(\boldsymbol{r}'_\perp, \boldsymbol{r}_\perp; \nu) = & \iiiint_{-\infty}^{\infty} \exp[-i(k_z - k'_z)z_r + i(\boldsymbol{k}_\perp \cdot \boldsymbol{r}_\perp - \boldsymbol{k}'_\perp \cdot \boldsymbol{r}'_\perp)] \\ & \times \tilde{W}^{(0)}(\boldsymbol{k}'_\perp, \boldsymbol{k}_\perp; \nu) d^2k_\perp d^2k'_\perp \, . \end{aligned} \tag{4.15}$$

Once $W^{(z_r)}(\boldsymbol{r}'_\perp, \boldsymbol{r}_\perp; \nu)$ across Σ_r is determined with Eq. (4.15), we can retrieve the spatial distribution of the spectral density, namely, an image at a particular frequency within the spectral range of the field, by simply setting $\boldsymbol{r}_\perp = \boldsymbol{r}'_\perp$:

$$S(\boldsymbol{r}_\perp, z_r; \nu) = W^{(z_r)}(\boldsymbol{r}_\perp, \boldsymbol{r}_\perp; \nu) \, . \tag{4.16}$$

The principle to retrieve the cross-spectral density and the spatial distribution of the spectral density across an arbitrary reference plane was presented above. Obviously, it is possible to retrieve them across the source plane by giving the distance z_s instead of z_r. The principle for retrieving the cross-spectral density described in this subsection is based on the simple, already established theorem. However, it was pointed out that using the principle inversely enables us to obtain, by measuring the cross-spectral density across the observation area, the cross-spectral density and the image without requirements for the paraxial approximation and the state of the spatial incoherence over the source.

4.3.2 Numerical calculation

Based on the theory stated in Subsection 4.3.1, the numerical calculation of the cross-spectral density across planes in the diffraction field is demonstrated in this section. For simplicity of calculation, let the source be one dimensional. It is also assumed that the field of the source is spatially incoherent and that the spectral density $S^{(z_s)}(x;\nu)$ is uniform within the source area; i.e.,

$$S^{(z_s)}(x;\nu) = s^{(z_s)}(\nu)\mathrm{rect}\left(\frac{x}{D}\right) \ , \tag{4.17}$$

where z_s is the distance between the source plane and the observation planes, $s^{(z_s)}(\nu)$ is a space-independent constant, and D is the width of the source. The geometry of the optical system assumed for the calculation is shown in Fig. 4.7. The optical axis is in the center of the source, and the origin of the coordinate system is on the observation plane Σ_o. Under these circumstances, the cross-spectral density $W^{(z_s)}(x',x;\nu)$ across the source plane is represented by means of $S^{(z_s)}(x;\nu)$:

$$W^{(z_s)}(x',x;\nu) = [S^{(z_s)}(x;\nu)S^{(z_s)}(x';\nu)]^{1/2}\delta(x-x') \ . \tag{4.18}$$

The forward propagation of the cross-spectral density from the source to a particular plane Σ_r at z_r is represented by

$$\begin{aligned} W^{(z_r)}(x',x;\nu) = \iint_{-\infty}^{\infty} & \exp[i(k_z - k_z')(z_s - z_r) + i(k_x x - k_x' x')] \\ & \times \tilde{W}^{(z_s)}(k_x', k_x;\nu)dk_x dk_x' \ , \end{aligned} \tag{4.19}$$

where $\tilde{W}^{(z_s)}(k_x', k_x;\nu)$ is the two-dimensional Fourier transform of $W^{(z_s)}(x',x;\nu)$ with respect to x and x', and Eq. (4.19) is derived in a similar manner for Eq.(4.15). The cross-spectral densities across Σ_r and Σ_o are calculated with this Fourier-transform-based algorithm. Parameters used in the calculation are $z_r = 40$ mm, $z_s = 75$ mm,

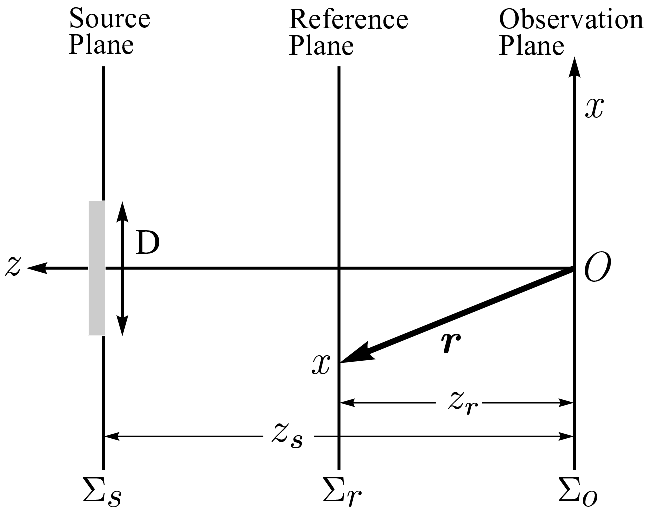

Fig. 4.7. Geometry of the optical system assumed for the numerical simulations.

$s^{(z)}(\nu) = 1$, and $D = 100\ \mu$m. Obtained real and imaginary parts of the cross-spectral densities across Σ_r and Σ_o are shown in Fig. 4.8(a)-4.8(d) as gray-level images. Since gray levels are normalized by maxima and minima of each cross-spectral density, zero levels are different in each figure as shown in linear scales inserted in figures. Starting from the assumption of $W^{(z_s)}(x', x; \nu)$ across the source, $W(x', x; \nu)$'s at Σ_r and Σ_o that are equivalent to the exact solution of the Fresnel-Kirchhoff diffraction formula are obtained with the propagation law of the angular cross-spectral density stated in Subsection 4.3.2

Turning now to the procedure for retrieving the cross-spectral density, results shown above tell us that the cross-spectral densities at the reference plane and the source plane can be retrieved with Eq. (4.19) inversely, namely, Eq. (4.15), if the cross-spectral density at the observation plane is measured. With this method, the exact distance from the observation plane to the source plane must be given to retrieve the cross-spectral density or the spatial distribution of the spectral density across the

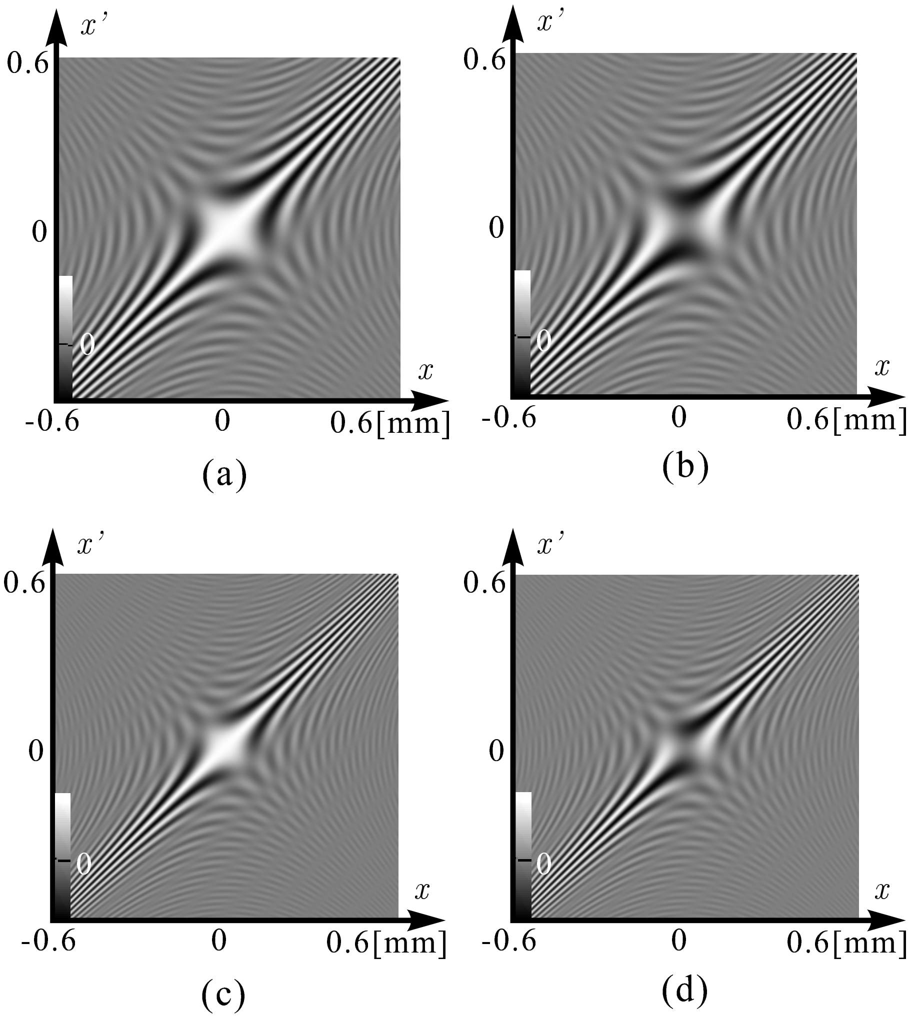

Fig. 4.8. Calculated cross-spectral density across reference planes: (a) real and (b) imaginary parts at Σ_r, (c) real and (d) imaginary parts at Σ_o.

source plane, although, in general, the distance may be unknown. However, as long as the field of the source is spatially incoherent, we can detect the existence of the source by giving appropriate values of distance stepwise into Eq. (4.15), since the effective correlation length of the field is known from the retrieved cross-spectral density. The cross sections along diagonal lines from the top right to the bottom left of Figs. 4.8(a)

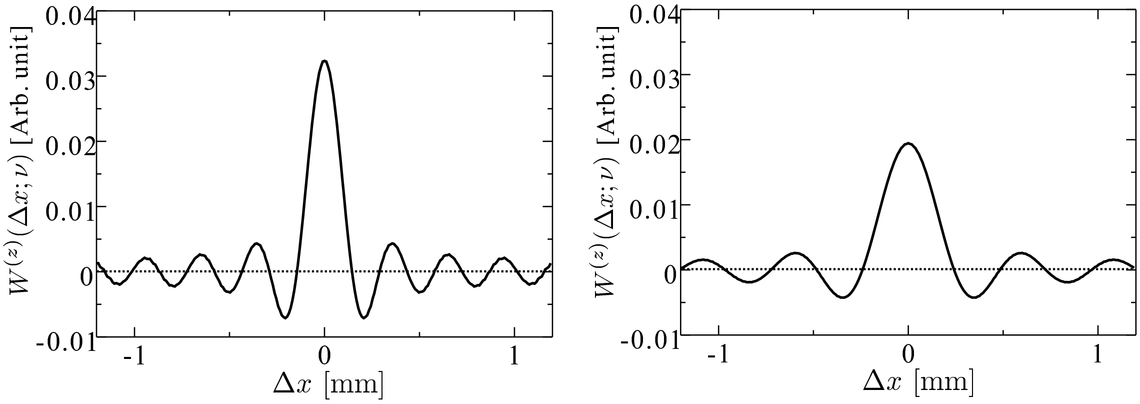

(a)

(b)

Fig. 4.9. Cross sections of the real part of the cross-spectral densities. (a) and (b) correspond to Figs. 4.8(a) and 4.8(c).

and 4.8(c) are plotted in Figs. 4.9(a) and 4.8(b). These are the real parts of cross-spectral densities at the reference plane Σ_r and the observation plane Σ_o as functions of $\Delta x = x - x'$ for the fixed average coordinate $\hat{x} = (x + x')/2 = 0$. Slowly varying curves in Figs. 4.9(a) and 4.9(b) imply that the field is spatially, partially coherent and that no incoherent source is on the plane. In contrast, it is easily understood from Eq. (4.18) that the profile of the cross-spectral density across the source plane as a function of Δx has a sharp peak at $\Delta x = 0$, since the field of the source is spatially incoherent. This results from the fact that the propagating wavefields from the incoherent source are spatially partially coherent.

4.3.3 Experimental demonstration

In this subsection we show results of the experiment for measuring and retrieving the cross-spectral density by using a wavefront folding interferometer. For simplicity, a two-dimensional cross-spectral density across the observation area was formed by

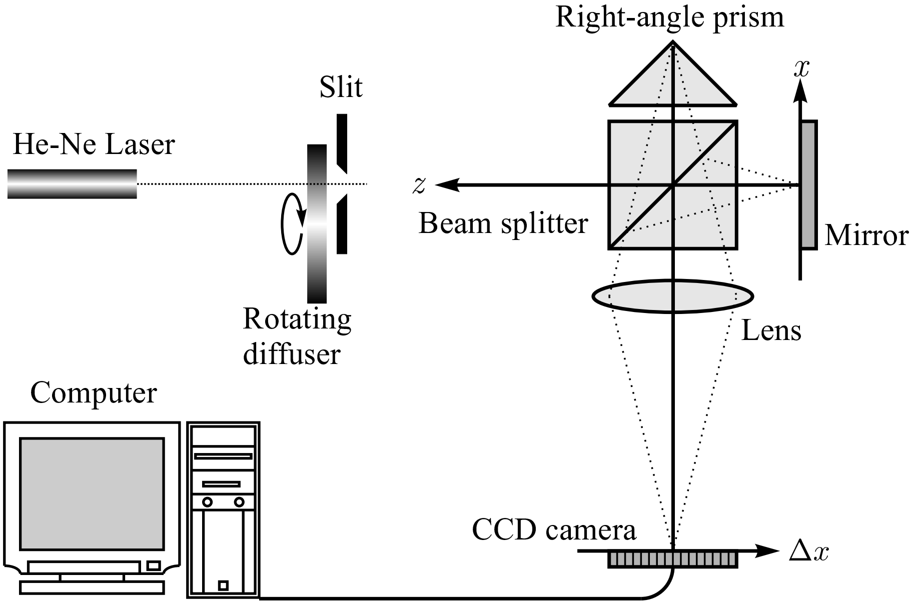

Fig. 4.10. Schematic of the wavefront folding interferometer for measuring the cross-spectral density.

placing at an appropriate distance a primary one-dimensional source such as a slit. The optical system used is shown in Fig. 4.10. The light emitted from a He-Ne laser with optical frequency $\nu = 473.8$ THz (wavelength 632.8 nm) is scattered by a rotating diffuser inserted just in front of the slit. The scattered light that simulates a spatially incoherent source is masked by a single slit. The width of the aperture is 100 μm. The beam splitter divides the propagating light. One beam reflects on a mirror; the other reflects and folds its wavefront on a right-angle glass prism. In this system, the cross-spectral density across the mirror surface (the observation plane) is measured, so that the superposed light is focused on the CCD camera by a lens with the magnification factor of 1. The distance between the source plane and the observation plane is $z_r = 75$ mm. The mirror is slightly tilted to introduce a vertical carrier frequency into the interference fringe formed on the CCD camera. The horizontal axis of the

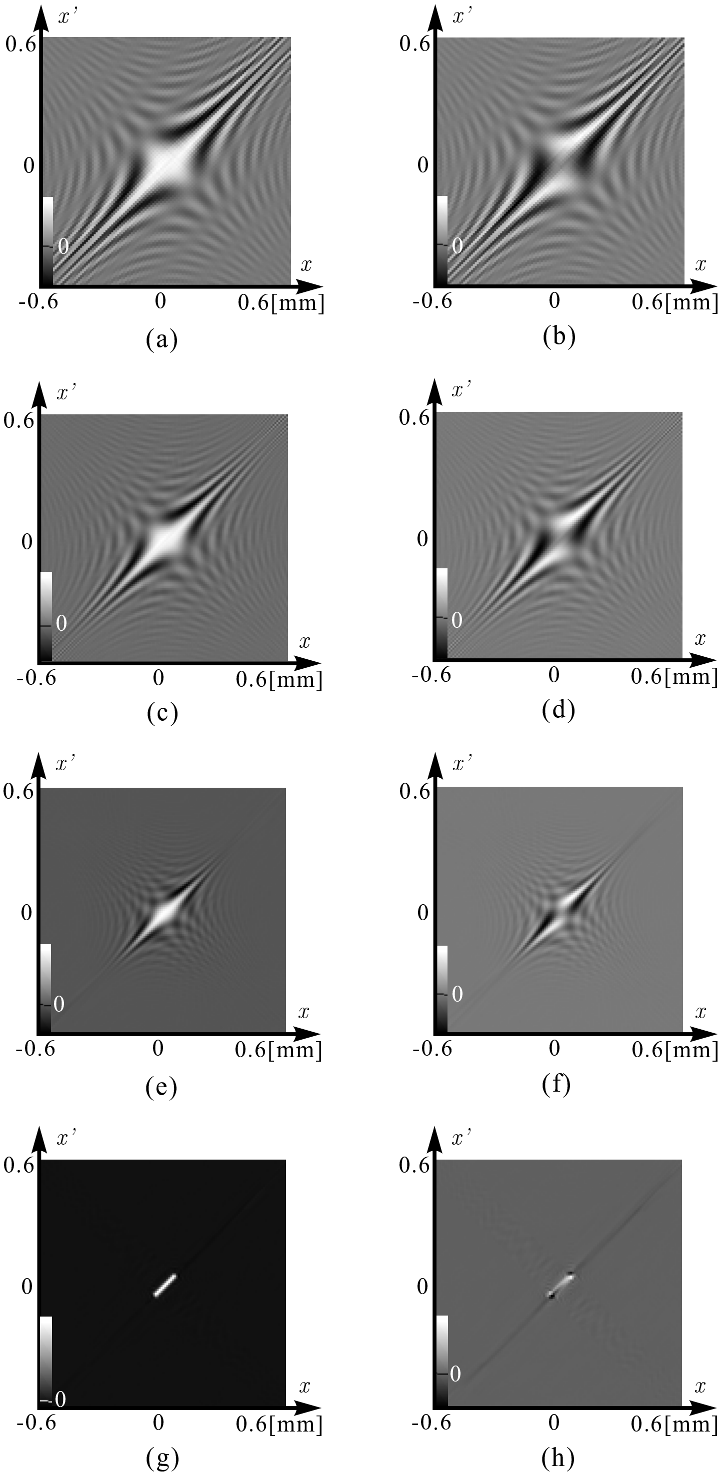

(a) (b) (c) (d) (e) (f) (g) (h)

Fig. 4.11. (a) Real and (b) imaginary parts of the measured cross-spectral density. (c), (e), and (g) are the real parts and (d), (f), and (h) are the imaginary parts of retrieved $W^{(z_r)}(x', x; \nu)$ for each z_r.

image obtained on the CCD camera represents the two-point separation $\Delta x = x - x'$ at a particular value of the average coordinate $\hat{x} = (x + x')/2$. To measure the cross-spectral density with respect to all pairs of points, it is necessary to move the entire interferometer stepwise parallel to the x axis. In the present experiment the light emitted from the laser is expanded quite uniformly, and the slit is moved instead of the interferometer. Thus $\hat{x}$ is determined by the location of the slit. Both real and imaginary parts of $W^{(0)}(\Delta x; \nu)$ for fixed $\hat{x}$ can be obtained by Fourier analysis of the carrier frequency component (see Chapter 7 in detail). Because of the dullness near the rectangular edge of the prism, the obtained interference fringes suddenly change phase around the point $\Delta x = 0$. Thus the phase is calibrated by measuring the interference fringes by illuminating the system coherently from a point source on the optical axis at the location of the slit and the rotating diffuser.

The measured real and imaginary parts of $W^{(z_r)}(x', x; \nu)$ are shown by gray scales in Figs. 4.11(a) and 4.11(b). The diagonal line from the top right to the bottom left of the real part represents the intensity distribution, i.e., $W^{(0)}(x, x; \nu) = S^{(0)}(x; \nu) \propto I^{(0)}(x)$ where $S^{(0)}(x; \nu)$ and $I^{(0)}(x)$ denote, respectively, the spectral density and the intensity of the actual quasi-monochromatic field at x on the observation plane. It can be seen from these figures that the wavefield over the observation plane is partially spatially correlated. The angular cross-spectral density $\tilde{W}^{(0)}(k'_x, k_x; \nu)$ is calculated by the two-dimensional FFT program, and $W^{(z_r)}(x', x; \nu)$ at $z_r = 25$, 50, and 75 mm are retrieved with Eq. (4.15) and the inverse FFT. The results are shown in Figs. 4.11(c)-4.11(h). As the reference plane approaches the source plane, the profiles of both the real and the imaginary parts of $W^{(z_r)}(x', x; \nu)$ shrink. This implies that the effective correlation distance along Δx decreases as the reference plane approaches the source plane. Finally, when the reference plane coincides with the source plane, both the real

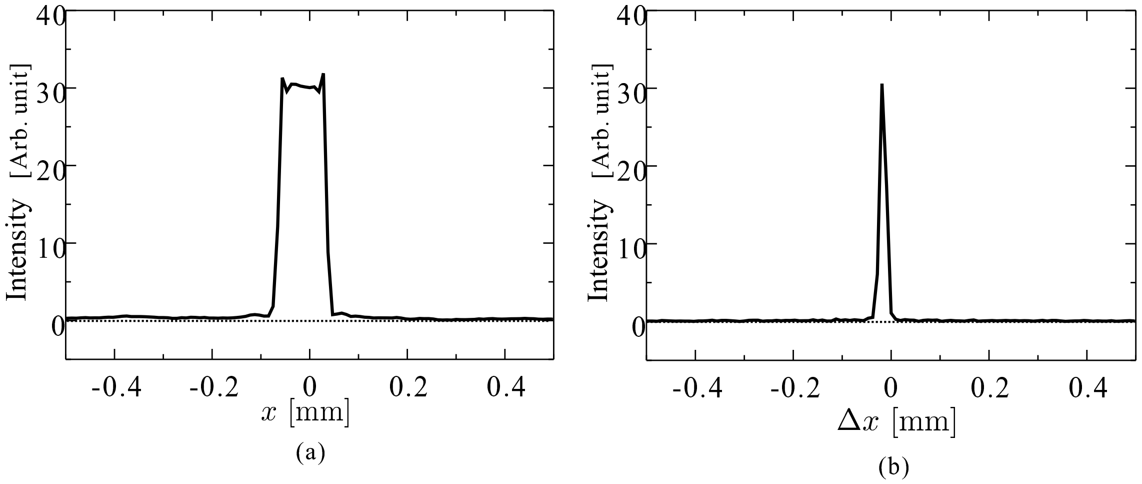

Fig. 4.12. Cross section of $|W^{(z_r)}(x', x; \nu)|$ across the source plane (a) along $\Delta x = 0$, and (b) along $x_o = 0$.

and the imaginary parts of $W^{(z_r)}(x', x; \nu)$ become almost zero except for the narrow and short area on the diagonal line of the real part. The imaginary part that appears on the diagonal line may be due to some errors in the experiment. The cross sections of the absolute value of $W^{(z_r)}(x', x; \nu)$ that is obtained from Figs. 4.11(g) and 4.11(h) are plotted in Figs. 4.12(a) and 4.12(b) ((a) represents $W^{(z_r)}(x, x; \nu) \propto I^{(z_r)}(x)$, and (b) represents $W^{(z_r)}(\Delta x; \nu)$ for $x_o = 0$). It is seen clearly from Fig. 4.12(a) that the intensity distribution across the source plane is almost rectangular, and a reasonable resolution is obtained. In contrast, Fig. 4.12(b) means that the wavefield across the source is almost spatially uncorrelated, since $W^{(z_r)}(\Delta x; \nu)$ is nearly zero unless x and x' coincide with each other. It is noteworthy that we can confirm the existence of the incoherent source across the plane by the sharp profile around $\Delta x = 0$ in Fig. 4.12(b), as pointed out in Subsection 4.3.2.

In the present demonstration, only a one-dimensional source was used, and the two-dimensional cross-spectral density was measured and retrieved to achieve the experiment simply. Measuring the four-dimensional cross-spectral density will, however, enable us to apply this method to the three-dimensional imaging. Further investigations of the relationship between the range of the coherence measurements and the resolution of the cross-spectral densities are also necessary for more quantitative discussions.

4.4 Conclusion

New methods to obtain the two-dimensional image were presented. One is based on the van Cittert-Zernike theorem for the wide spectral bandwidth. The procedure based on the Fourier transform algorithm reconstructs the spectral density distribution of the uncorrelated two point sources at a particular frequency, and the successive procedures give not only the angular separation but also the spectral profiles of the sources. The experimental results well agreed with the theoretical expectations. The other technique is based on the propagation law of the angular spectrum of the wavefield. The propagation of the cross-spectral density can be represented in a similar manner in the spatial-frequency domain, and the source image is retrieved using this propagation law inversely. The experimental demonstration was conducted by incorporating a single slit as a light source, and the intensity distribution of this source was retrieved by the inverse propagation of the cross-spectral density.

Chapter 5

Passive interferometric 3-D imaging and incoherence gating

5.1 Introduction

The two-dimensional interferometric imaging techniques have been considerably sophisticated owing to the long study and the practical applications. The recent demand for the interferometric imaging is retrieving the 3-D information. Concerned with the forward propagation of the spatial coherence, LaHaie presented the modified van Cittert-Zernike theorem that is extended to the 3-D space in 1985.[85] More recently, Rosen proposed a new principle for retrieving the 3-D image from the measured spatial coherence function across an observation area.[73 – 75] However, there still are some problems such as restrictions to the state of the coherence over the source.

From this background, a new interferometric 3-D imaging technique is presented in this chapter based on the propagation law of the angular cross-spectral density that was stated in Chapter 4. In contrast with the conventional technique in which the image is retrieved directly from the measured spatial coherence function, the present method is based on retrieving the sequential cross-spectral densities that are perpendicular to the optical axis. Since the cross-spectral density with respect to the same point represents the spectral density, a 3-D image can be obtained from a sequence of retrieved cross-spectral densities. The cross-spectral density and the intensity distribution are reconstructed from the observation plane to the arbitrary required distance.

By using the sequence of retrieved cross-spectral densities, spatially incoherent sources can be detected. Since the state of the spatial coherence around a specific point is evaluated from the retrieved cross-spectral density, we can distinguish spatially incoherent primary sources from the radiant intensity distribution based on the fact that propagating wavefields are partially correlated as described by the van Cittert-Zernike theorem. As a measure of the spatial incoherence, we use a sharpness or a narrowness of the cross-spectral density as a function of the two-point separation. Spatially incoherent sources can be clearly separated by gating the second-order differential of the sequence of retrieved cross-spectral densities with a moderate threshold. A simple experiment demonstrating the incoherence gating method is presented.

In this chapter, the general principle of retrieving the 3-D image is first given. We also estimate the point spread function in the present interferometric imaging system dependent upon the baseline length for the cross-spectral density measurements. Next, the concept of the incoherence gating technique is explained. In Section 5.3, the results of the experiment for verifying the theory is presented. Although we assume a 3-D optical system in the general theory, we retrieve the intensity distribution over the longitudinal axis and one transverse axis for simplicity. Results of an experimental demonstration for the incoherent gating is also shown.

5.2 Formulation of principle

5.2.1 Principle of 3-D imaging

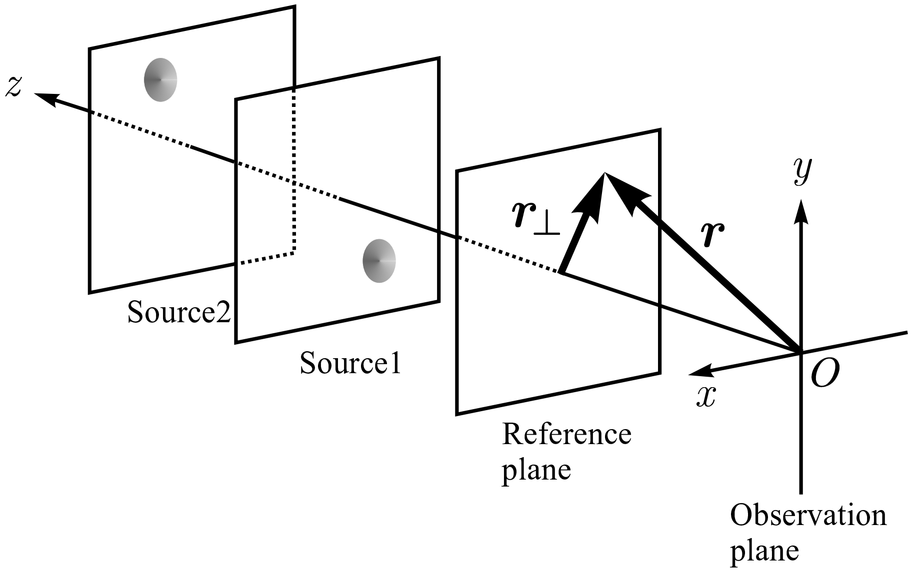

Fig. 5.1. Schematic of optical system.

In this subsection, the mathematical formulation for retrieving the 3-D intensity distribution by measuring the propagated cross-spectral density is described. With reference to Fig. 5.1, we assume quasi-monochromatic two-dimensional sources distributed longitudinally. A typical source distribution with two elements is drawn in the figure. Let a particular point on a reference plane which is perpendicular to the optical axis be specified by a three-dimensional position vector $\boldsymbol{r} = (\boldsymbol{r}_\perp, z) = (x, y, z)$. The origin of the coordinate system is on the observation plane.

The forward and the inverse propagation laws of the angular cross-spectral density are represented by

$$\tilde{W}^{(0)}(\boldsymbol{k}'_\perp, \boldsymbol{k}_\perp; \nu) = \exp\left[i(k_z - k'_z)z\right] \tilde{W}^{(z)}(\boldsymbol{k}'_\perp, \boldsymbol{k}_\perp; \nu) , \tag{5.1}$$

and

$$\tilde{W}^{(z)}(\boldsymbol{k}'_\perp, \boldsymbol{k}_\perp; \nu) = \exp\left[-i(k_z - k'_z)z\right] \tilde{W}^{(0)}(\boldsymbol{k}'_\perp, \boldsymbol{k}_\perp; \nu) \, , \tag{5.2}$$

as described in Chapter 4. To distinguish clearly from the cross-spectral density of the primary source from that of the radiated field, let us represents the cross-spectral density of the primary source by $\Omega(\boldsymbol{r}'_\perp, \boldsymbol{r}_\perp; \nu)$. The relationship between the cross-spectral density of the secondary source and that of the primary source, which is derived from the relationship between the field variable and the source variable, is represented[86] by

$$\tilde{W}(\boldsymbol{k}'_\perp, \boldsymbol{k}_\perp; \nu) = \frac{4\pi^2}{k_z k'_z} \tilde{\Omega}(\boldsymbol{k}'_\perp, \boldsymbol{k}_\perp; \nu) \, . \tag{5.3}$$

As long as sources are uncorrelated with each other and disturbances of free propagation such as diffractions or obstructions can be ignored, the angular cross-spectral density across the observation plane is represented as the summation of all contributions from each primary source:

$$\tilde{W}^{(0)}(\boldsymbol{k}'_\perp, \boldsymbol{k}_\perp; \nu) = \sum_{z_n} \exp[i(k_z - k'_z)z_n] \tilde{\Omega}^{(z_n)}(\boldsymbol{k}'_\perp, \boldsymbol{k}_\perp; \nu) \, , \tag{5.4}$$

where z_n is the distance from the observation plane to the nth source. Based on Eqs. (5.1) and (5.4), the angular cross-spectral density across a particular plane at $z = z_o$ is retrieved as

$$\begin{aligned} \tilde{W}^{(z_o)}(\boldsymbol{k}'_\perp, \boldsymbol{k}_\perp; \nu) &= \exp[-i(k_z - k'_z)z_o] \tilde{W}^{(0)}(\boldsymbol{k}'_\perp, \boldsymbol{k}_\perp; \nu) \\ &= \frac{4\pi^2 \tilde{\Omega}^{(z_o)}(\boldsymbol{k}'_\perp, \boldsymbol{k}_\perp; \nu)}{k_z k'_z} \\ &+ \sum_{z \neq z_o} \exp[i(k_z - k'_z)(z_n - z_o)] \frac{4\pi^2 \tilde{\Omega}^{(z_n)}(\boldsymbol{k}'_\perp, \boldsymbol{k}_\perp; \nu)}{k_z k'_z} \, . \end{aligned} \tag{5.5}$$

The second line of Eq. (5.5) implies that the retrieved angular cross-spectral density across the specific source plane consists of its own contribution and propagated angular cross-spectral densities from other sources. After the angular cross-spectral density across a desired plane is obtained, the four-dimensional inverse Fourier transform gives the cross-spectral density across the target plane as

$$\begin{aligned}
W^{(z_o)}(\boldsymbol{r}'_\perp, \boldsymbol{r}_\perp; \nu) &= \iiiint_{-\infty}^{\infty} \exp[-i(k_z - k'_z)z_o + i(\boldsymbol{k}_\perp \cdot \boldsymbol{r}_\perp - \boldsymbol{k}'_\perp \cdot \boldsymbol{r}'_\perp)] \\
&\quad \times \tilde{W}^{(0)}(\boldsymbol{k}'_\perp, \boldsymbol{k}_\perp; \nu) d^2k_\perp d^2k'_\perp \\
&= \frac{4\pi^2 \Omega^{(z_o)}(\boldsymbol{r}'_\perp, \boldsymbol{r}_\perp; \nu)}{k_z k'_z} \\
&\quad + \sum_{z_n \neq z_o} \iiiint_{-\infty}^{\infty} \exp[-i(k_z - k'_z) + i(\boldsymbol{k}_\perp \cdot \boldsymbol{r}_\perp - \boldsymbol{k}'_\perp \cdot \boldsymbol{r}'_\perp)] \\
&\quad \times \frac{4\pi^2 \tilde{\Omega}^{(z_n)}(\boldsymbol{k}'_\perp, \boldsymbol{k}_\perp; \nu)}{k_z k'_z} d^2k_\perp d^2k'_\perp \, . \qquad (5.6)
\end{aligned}$$

In lines 3 and 4 of Eq. (5.6), $\Omega^{(z_o)}(\boldsymbol{r}'_\perp, \boldsymbol{r}_\perp; \nu)$ represents the cross-spectral density with respect to the *focused* source, and the summation part represents contributions from *defocused* sources. Once the cross-spectral density is retrieved, the spectral density distribution $S^{(z_o)}(\boldsymbol{r}_\perp; \nu)$ of the plane concern is readily extracted by

$$S^{(z_o)}(\boldsymbol{r}_\perp; \nu) = W^{(z_o)}(\boldsymbol{r}_\perp, \boldsymbol{r}_\perp; \nu) \, . \qquad (5.7)$$

Since we assume that the source spectrum is quasi-monochromatic, the spectral density distribution is proportional to the intensity distribution. It may be easily understood that continuous procedures described above with a moderate interval of z give the 3-D intensity distribution in a slab geometry.

Next, let us confine ourselves to the influence of the limitation of the baseline length for measuring the cross-spectral density on the retrieved intensity distribution in a practical observation. As is well known, the point spread function in an ordinary imaging system is given as the Fourier transform of the complex amplitude transmittance of the pupil, and the intensity distribution across an out-of-focus plane is given by the diffraction formula. In the following, we derive formulas which correspond to the point spread function in an ordinary imaging system.

We assume a point source on the optical axis separated by distance z_s from the observation plane. For simplicity, the cross-spectral density and the intensity distribution on the x-z plane are considered. The cross-spectral density across the primary source plane is then represented by

$$\Omega^{(z_s)}(x', x; \nu) = s_o \delta(x) \delta(x') \,, \tag{5.8}$$

where s_o is a constant and $\delta(x)$ is the Dirac delta function. Substituting Eq. (5.8) into Eqs. (2.44) and (5.1) and taking the inverse Fourier transform with respect to k_x and k_x' gives the cross-spectral density across the observation plane:

$$\begin{aligned} W^{(0)}(x', x; \nu) &= 2\pi s_o \int_{-\infty}^{\infty} \frac{\exp[i(k_z z_s - k_x x)]}{k_z} dk_x \\ &\quad \times \int_{-\infty}^{\infty} \frac{\exp[-i(k_z' z_s - k_x' x')]}{k_z'} dk_x' \,. \end{aligned} \tag{5.9}$$

In a practical experiment, the baseline length for the cross-spectral density measurements is limited by such as a linear dimension of a CCD tip or a stroke length of a positioning system. The measured cross-spectral density is thus represented as a product of two rectangular functions and Eq. (5.9):

$$\begin{aligned} W_{\mathrm{m}}^{(0)}(x', x; \nu) &= 2\pi s_o \mathrm{rect}\left(\frac{x}{D}\right) \int_{-\infty}^{\infty} \frac{\exp[i(k_z z_s - k_x x)]}{k_z} dk_x \\ &\quad \times \mathrm{rect}\left(\frac{x'}{D}\right) \int_{-\infty}^{\infty} \frac{\exp[-i(k_z' z_s - k_x' x')]}{k_z'} dk_x' \,, \end{aligned} \tag{5.10}$$

where D is the baseline length, and $\mathrm{rect}(x) = 1$ for $-1/2 \leq x \leq 1/2$ and 0 otherwise. Let us consider the inverse propagation of the measured cross-spectral density $W_{\mathrm{m}}^{(0)}(x', x; \nu)$ to a specific reference plane separated by z from the observation plane. By substituting the angular cross-spectral density, which is given by the two-dimensional Fourier transform of Eq. (5.10), into Eq. (5.6), we can obtain the cross-spectral density across the reference plane as

$$\begin{aligned} W_{\mathrm{m}}^{(z)}(x', x; \nu) & \\ = \; & 2\pi s_o \int_{-\infty}^{\infty} \exp[-i(k_z z + k_x x)] dk_x \otimes \mathrm{rect}\left(\frac{x}{D}\right) \int_{-\infty}^{\infty} \frac{\exp[i(k_z z_s - k_x x)]}{k_z} dk_x \\ \times \; & \int_{-\infty}^{\infty} \exp[i(k_z' z + k_x' x')] dk_x' \otimes \mathrm{rect}\left(\frac{x'}{D}\right) \int_{-\infty}^{\infty} \frac{\exp[-i(k_z' z_s - k_x' x')]}{k_z'} dk_x' \, , \end{aligned} \tag{5.11}$$

where $\otimes$ denotes the convolution integral. Equation (5.11) is an exact formula which represents the cross-spectral density retrieved from the measurements within the area of D on the observation plane. To calculate the cross-spectral density analytically, we adopt the paraxial approximation:

$$k_z = \sqrt{k^2 - k_x^2} \approx k - \frac{k_x^2}{2k} \, . \tag{5.12}$$

Equation (5.11) then reduces to

$$\begin{aligned} W_{\mathrm{m}}^{(z)}(x', x; \nu) \; = \; & \frac{8\pi^3 s_o}{z z_s} \int_{-\infty}^{\infty} \mathrm{rect}\left(\frac{\xi}{D}\right) \exp\left[\frac{ik}{2z}(x-\xi)^2\right] \exp\left(-\frac{ik}{2z_s}\xi^2\right) d\xi \\ \times \; & \int_{-\infty}^{\infty} \mathrm{rect}\left(\frac{\xi}{D}\right) \exp\left[-\frac{ik}{2z}(x'-\xi)^2\right] \exp\left(\frac{ik}{2z_s}\xi^2\right) d\xi \, . \end{aligned} \tag{5.13}$$

Substituting $z = z_s$ gives the retrieved cross-spectral density across the source plane:

$$W_{\mathrm{m}}^{(z_s)}(x', x; \nu) = \frac{8\pi^3 s_o D^2}{z_s^2} \exp\left[\frac{ik}{2z_s}(x^2 - x'^2)\right] \mathrm{sinc}\left(\frac{Dkx}{z_s}\right) \mathrm{sinc}\left(\frac{Dkx'}{z_s}\right) \, , \tag{5.14}$$

and obviously the spectral density distribution is

$$S^{(z_s)}(x; \nu) = W_{\mathrm{m}}^{(z_s)}(x', x; \nu) = \frac{8\pi^3 s_o D^2}{z_s^2} \left[\mathrm{sinc}\left(\frac{Dkx}{z_s}\right)\right]^2 \, . \tag{5.15}$$

The spectral density distribution at $z \neq z_s$ can be derived from Eq. (5.13) by a variable transform of $X = (z_s - z)\xi / z_s$ as

$$S^{(z)}(x; \nu) \; = \; \frac{8\pi^3 s_o z_s}{z(z_s - z)^2} \int_{-\infty}^{\infty} \exp\left[\frac{ikz_s}{2z(z_s - z)}(X - x)^2\right] \mathrm{rect}\left[\frac{z_s X}{(z_s - z)D}\right] dX$$

$$\times \int_{-\infty}^{\infty} \exp\left[-\frac{ikz_s}{2z(z_s - z)}(X - x)^2\right] \mathrm{rect}\left[\frac{z_s X}{(z_s - z)D}\right] dX \, . \tag{5.16}$$

We considered the two-dimensional cross-spectral density (as a function of x and x') along the x axis. However, the two-dimensional cross-spectral density (as a function of x, x', y, and y') can be treated in the same manner. As seen from Eqs. (5.15) and (5.16), the spectral density distribution retrieved by the present interferometric imaging is the same functional form as the intensity distribution obtained by an ordinary imaging system. The area of the cross-spectral density measurements and the distance between the source and the observation plane correspond to the aperture and $2f$ of the lens respectively. Namely, the same intensity distribution can be obtained behind the observation plane by setting a cylindrical lens with a focal length $f = z_s/2$ and width of D on the observation plane. In interferometric imaging based on the van Cittert-Zernike theorem, the point spread function is a sinc function because the retrieved intensity distribution is given as the Fourier transform of the mutual intensity across the observation plane. The retrieved function can thus take a negative value. In contrast, the intensity distribution retrieved by the present method is always positive, as is obvious from the above results.

5.2.2 Incoherence gating in interferometric imaging

We can retrieve the 3-D intensity distribution of a spatially, partially coherent source in a slab geometry because the propagation law of the angular cross-spectral density can be derived without any requirements for the spatial coherence. However, confirming the existence and determining the location of the spatially, partially coherent source, particularly the source with a fuzzy outline, are difficult using the present method. In contrast, detecting the spatially incoherent sources can be effectively processed from the retrieved sequential cross-spectral densities. In this subsection, a novel method to detect spatially incoherent sources based on the retrieval of the cross-spectral density described in Subsection 5.2.1 is presented. To reconstruct the intensity distribution in the 3-D space, we need only $W(\boldsymbol{r}_\perp, \boldsymbol{r}_\perp; \nu)$ components of a sequence of retrieved cross-spectral densities. However, components of the cross-spectral density with $\boldsymbol{r}_\perp \neq \boldsymbol{r}'_\perp$ designate the state of the spatial coherence across an arbitrary transverse plane. Let us assume a spatially incoherent planar source. If the magnitude of the retrieved cross-spectral density, as a function of a two-point separation $\Delta\boldsymbol{r}_\perp = \boldsymbol{r} - \boldsymbol{r}'_\perp$ for a specific average coordinate $\hat{\boldsymbol{r}}_\perp = (\boldsymbol{r}_\perp + \boldsymbol{r}'_\perp)/2$ across a particular transverse plane, varies smoothly around $\Delta\boldsymbol{r}_\perp = 0$, it implies that the incoherent source does not exist at $\hat{\boldsymbol{r}}_\perp$. In contrast, a sharp or narrow peak at $\Delta\boldsymbol{r}_\perp = 0$ implies the possible existence of the incoherent source at $\hat{\boldsymbol{r}}_\perp$.

In order to evaluate the sharpness or the narrowness of the magnitude of the cross-spectral density at $\Delta\boldsymbol{r}_\perp = 0$, we use the second-order differential of the magnitude of the cross-spectral density with respect to $\Delta\boldsymbol{r}_\perp$:

$$D^{(z)}(\Delta\boldsymbol{r}_\perp, \hat{\boldsymbol{r}}_\perp; \nu) \equiv -\frac{\partial^2 |W^{(z)}(\Delta\boldsymbol{r}_\perp, \hat{\boldsymbol{r}}_\perp; \nu)|}{\partial(\Delta\boldsymbol{r}_\perp)^2} \,. \tag{5.17}$$

For evaluating the state of the spatial coherence of the wavefields, a full width at half the maximum (FWHM) of the cross-spectral density or the spectral degree of coherence is used in many cases. The reason that we use the second order differential of the cross-spectral density is to make it possible to detect spatially incoherent sources even if the sources are illuminated by other bright sources. When there is only one spatially incoherent source, the magnitude of the cross-spectral density across the source plane is equal to the spectral density of the source at $\Delta\boldsymbol{r}_\perp = 0$, but 0 at $\Delta\boldsymbol{r}_\perp \neq 0$. In this case, of course, the source can be detected using both the FWHM and the second-order differential of the cross-spectral density. However, in case that the source is illuminated brightly by other sources, the cross-spectral density across the source plane is not 0 at $\Delta\boldsymbol{r}_\perp \neq 0$ because the propagated wavefields are partially correlated and the cross-spectral density is represented as a summation of these contributions (see Eq. (5.4)). Namely, the FWHM of the cross-spectral density with respect to $\Delta\boldsymbol{r}_\perp$ depends on the illumination by other sources. On the other hand, the second order differential of the cross-spectral density at $\Delta\boldsymbol{r}_\perp = 0$ is independent of such a illumination since the second-order differential designates the sharpness. Thus the spatial distribution of the second-order differential at $\boldsymbol{r}_\perp = 0$ with respect to $\Delta\boldsymbol{r}_\perp$ shows a measure of the incoherence over the x-y-z space, and a moderate gate will be enable us to detect the spatially incoherent sources.

5.3 Experimental demonstrations

5.3.1 Experiment of 3-D imaging

To verify the theory stated in the previous section, experiments for retrieving the 3-D intensity distribution over a diffraction field incorporating the uncorrelated two point sources were demonstrated. The schematic of the experimental setup is shown in Fig. 5.2. Two single-mode optical fibers (core diameters 8 μm) and individual He-Ne lasers (wavelength 632.8 nm) simulate the uncorrelated two point sources. Tips of fibers are separated by 0.8 mm along the x axis and 20 mm along the z axis. The wavefront folding interferometer used in the experiment is same as that presented in Chapter 4. For simplicity, only the cross-spectral density along the x axis was measured. The principle and the procedure of the measurements are also same as that in Chapter 4, and details are omitted here. In the present experiment, the ends

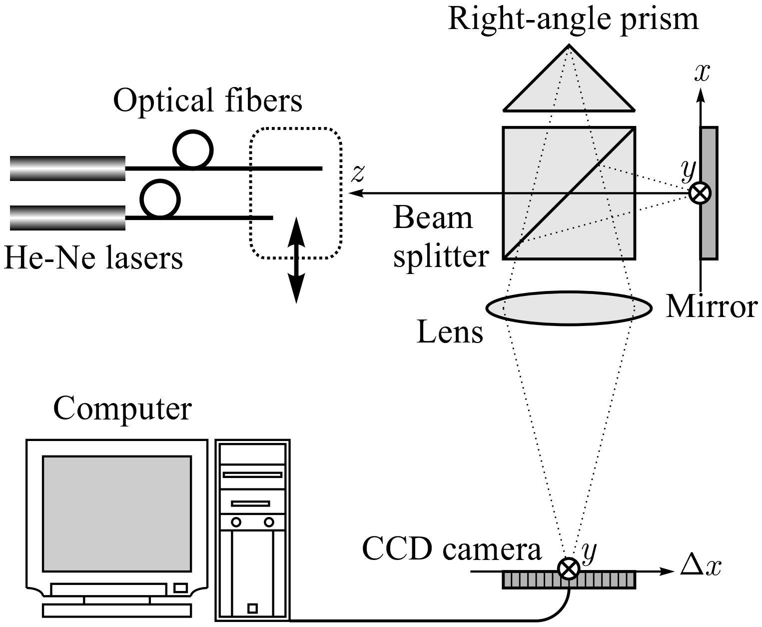

Fig. 5.2. Experimental setup for measuring the cross-spectral density.

of fibers were also moved along the x axis by using a micropositioner instead of moving the entire interferometer. Five hundred and twelve frames of fringe images were taken by the camera while fiber tips were moved 2.4 mm. The real and the imaginary parts of the cross-spectral density across the observation plane are shown in (a) and (b) of Fig. 5.3 as gray-level images. Whiter levels indicate higher values. The origin of the coordinate system is at the center of each figure, and the cross section along the diagonal line from the top right to the bottom left of the real part represents the spectral density distribution across the observation plane.

To retrieve the cross-spectral density across an arbitrary transverse plane, the two-dimensional Fourier transform of the measured cross-spectral density with respect to x and x' is calculated by a FFT program. Substituting the distance to the target plane into Eq. (5.5) and taking the inverse Fourier transform give the required cross-

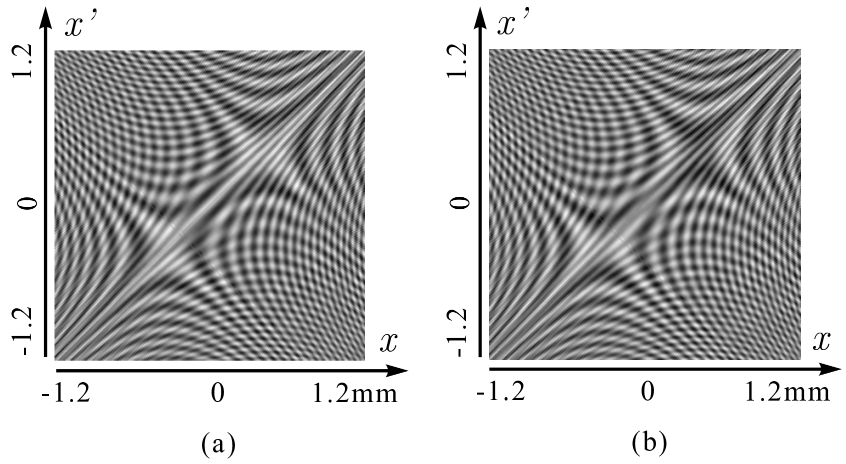

Fig. 5.3. (a) Real and (b) imaginary parts of the measured cross-spectral density across the observation plane expressed by gray-level images.

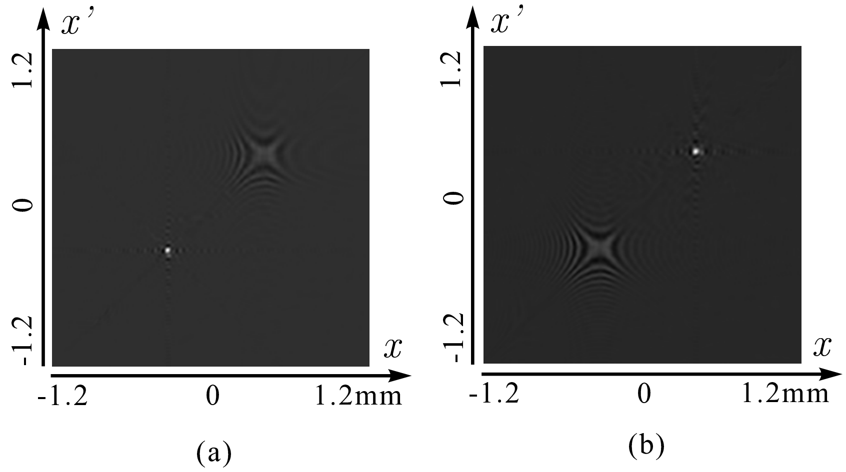

Fig. 5.4. Real parts of retrieved cross-spectral densities across (a) source 1 plane at $z = 110$ mm and (b) source 2 plane at $z = 130$ mm.

spectral density. The real parts of cross-spectral densities across two source planes at $z = 110$ and 130 mm are shown in (a) and (b) of Fig. 5.4. Since each gray-level image is normalized by its maximum and minimum, zero-levels differ from each other. As seen from the two figures, the cross-spectral density of the *focused* source appears as a

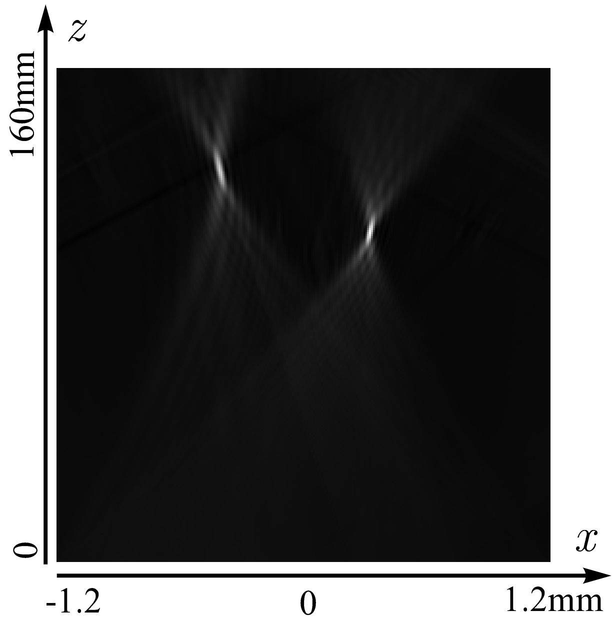

Fig. 5.5. Gray-level image of the retrieved intensity distribution on the x-z plane.

point while that of the *defocused* source is stretched in the x-x' plane. The extension of the defocused cross-spectral density along the $\Delta x = x - x'$ direction means that the field that propagated from the source at the other plane is spatially correlated. Repeating the same procedures while varying the distance of a target plane, we can reconstruct a sequence of cross-spectral densities over the x-z plane and retrieve the x-z intensity distribution by extracting components of $x = x'$. The result is shown in Fig. 5.5. The bottom of the figure is the observation plane. The separations along both the x axis and the z axis are retrieved almost exactly. Although the light is emitted toward the negative direction of z, the intensity distribution appears not only in the negative direction of z but also almost symmetrically in the positive direction from sources. In addition, the narrow rod-like part around the near source is longer than that of the far source because the intensity distribution retrieved by the present interferometric imaging system is equivalent to that obtained by an ideal imaging system using a lens as shown in the previous section.

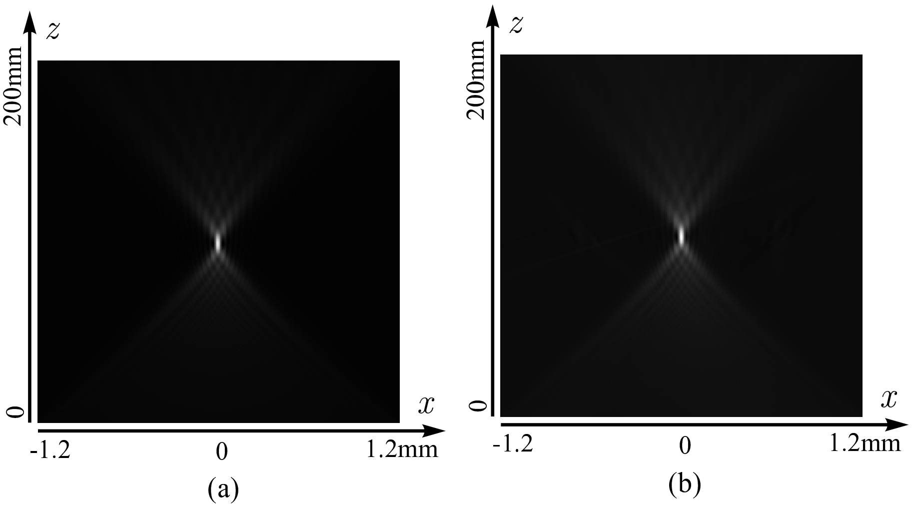

Fig. 5.6. Intensity distributions on the x-z plane for a point source. (a) Theoretically calculated and (b) experimental results.

Next, we retrieved the x-z intensity distribution using one point source located on the optical axis is order to evaluate the point spread function discussed in Section 5.2. Since Eq. (5.16) is derived by using paraxial approximations, it does not represent the exact intensity distribution on the x-z plane. Therefore, numerical calculation was performed by a computer without the paraxial approximation. Fig. 5.6 (a) is a result of the calculation for a point source. A distance between the source and the observation plane is 100 mm, and the baseline length for measuring the cross-spectral density is 2.4 mm. Fig. 5.6 (b) is an experimental results under the same condition as the numerical computation. As seen from two figures, the experimental results almost agree with the theory though a contrast of the experimental result is a little worse than that of the theoretical result.

5.3.2 Experiment of incoherence gating

The incoherence gating technique explained in Section 5.2 was demonstrated by using the sequence of retrieved cross-spectral densities which was reported in Subsection 5.3.1. The intensity distribution on the x-z plane is shown in Fig. 5.7 (a). Note that the sequence of cross-spectral densities was retrieved using the measured cross-spectral density whose range differs from the results shown in Subsection 5.3.1, i.e., $-2.4 \leq \Delta x \leq 2.4$ mm and $-1.2 \leq \hat{x} \leq 1.2$ mm. Therefore, the profile of the intensity distribution over the x-z plane is somewhat different from Fig. 5.5. Although only $W^{(z)}(x, x; \nu)$ components of the sequence of cross-spectral densities are plotted, we have $W^{(z)}(x', x; \nu)$ for all z's in the slab geometry of Fig. 5.7 (a). By taking the second-order differential of the cross-spectral density with respect to Δx, $D^{(z)}(\Delta x, \hat{x}; \nu)$'s for each z are obtained. The spatial distribution of $D^{(z)}(\Delta x, \hat{x}; \nu)$ in the same slab geometry as Fig. 5.7 (a) is shown in Fig. 5.7 (b) as a gray-level image. This image can be regarded as a measure of spatial incoherence over the x-z plane. Radiations from two primary sources seen in Fig. 5.7 (a) thus disappear in (b) because propagated wavefields are partially correlated. A triangular area appears slightly in $-0.3 \leq x \leq 0.4$ mm, $60 \leq z \leq 90$ mm. This means that the superposition of wavefields reduce the spatial coherence of the field. This fact is very important and represents the difference between the intensity distribution and the $D^{(z)}(\Delta x, \hat{x}; \nu)$ distribution. A dark primary source may thus be detected under bright illumination. To distinguish primary sources from the radiation clearly, a gate with a moderate threshold is adopted to $D^{(z)}(\Delta x, \hat{x}; \nu)$. In the present demonstration, the threshold was set to 50% of the maximum of $D^{(z)}(\Delta x, \hat{x}; \nu)$. The result is shown in Fig. 5.7 (c). As seen from the figure, primary sources alone are plotted as small spots and correlated radiations

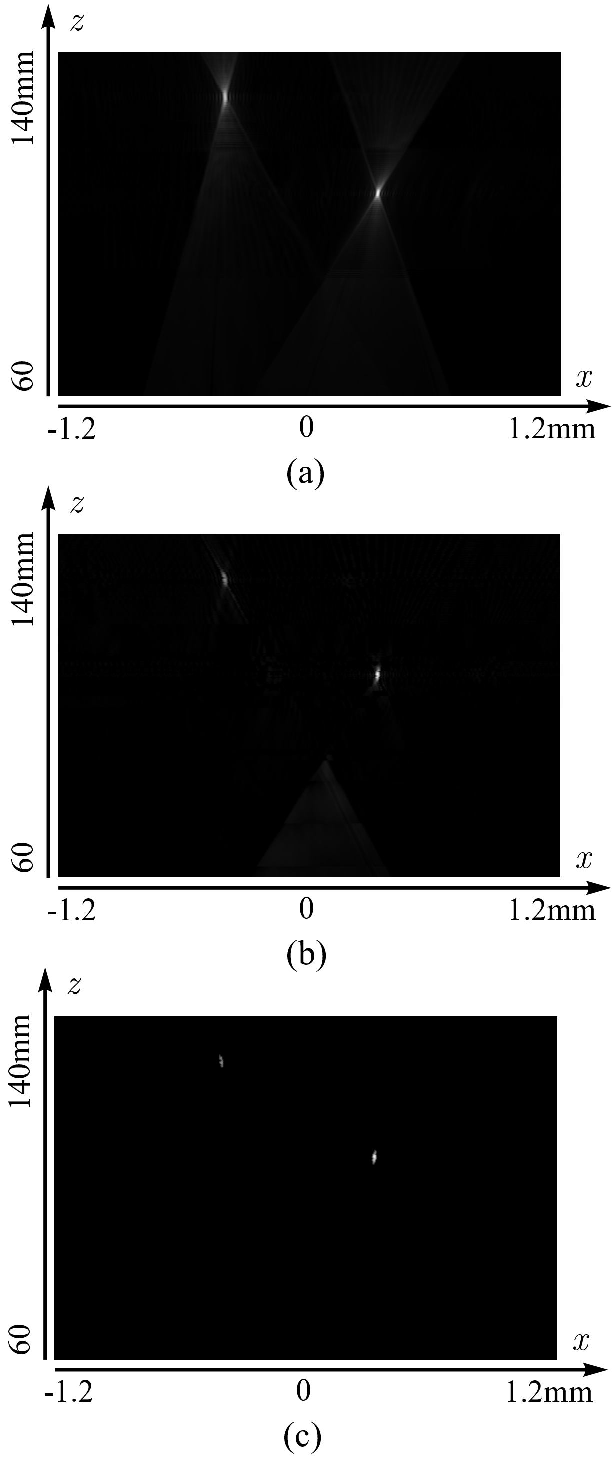

Fig. 5.7. (a) Intensity distributions on the x-z plane for two point sources. (b) $D^{(z)}(\Delta x, \hat{x}; \nu)$ on the x-z plane. (c) $D^{(z)}(\Delta x, \hat{x}; \nu)$ after the gating.

disappear.

In this simple demonstration, almost the same result as Fig. 5.7 (c) may be obtained by adjusting the contrast or gating of the intensity distribution shown in Fig. 5.7 (a). However, as pointed out above, the $D^{(z)}(\Delta x, \hat{x}; \nu)$ distribution is quite different from the intensity distribution because the $D^{(z)}(\Delta x, \hat{x}; \nu)$ distribution is a measure of the field correlation around a specific point $\hat{x}$. Therefore, this technique will enable us to detect primary sources such as spatially incoherent planar sources not only point sources.

5.4 Conclusion

A new interferometric 3-D imaging method based on retrieving the sequential cross-spectral densities was proposed. The cross-spectral density across an arbitrary transverse plane can be retrieved by using the propagation law described in the spatial-frequency domain. Details of an experiment that incorporated two point sources were also presented. Results of the experiment agreed well with the theoretical expectations. The point spread function of the proposed interferometric imaging system and its similarity to an ordinary imaging system were discussed. It was proven that the retrieved intensity distribution coincides with that measured by a image forming lens whose linear dimension is the same as the baseline length. To detect spatially incoherent sources, an incoherent gating technique which estimates field correlations from the sequence of retrieved cross-spectral densities was proposed. By taking the second-order differential of the cross-spectral density with respect to the two-point separation, primary sources were separated from partially correlated field.

Chapter 6

Interferometric 3-D imaging and generalized radiance distribution

6.1 Introduction

Using the propagation law of the cross-spectral density described in the spatial-frequency domain, a new technique for retrieving the 3-D intensity distribution was proposed in Chapter 5.[87, 88] However, this principle requires a high computational load because of the successive Fourier transform of the four-dimensional cross-spectral density.

On the other hand, problems in the relationship between the spatial coherence and radiometry have been investigated for the last three decades.[89 – 104] Various definitions of the generalized radiance function (GRF) have been proposed, and theoretical investigations of propagating properties of the radiance dependent upon the source correlation have also been made since Walther first generalized this concept.[105] Walther defined two types of GRFs in his pioneering publications.[105, 106]

From this background, another new interferometric 3-D imaging technique based on retrieving the spatial distributions of Walther's GRF is presented in this chapter.

Both the first and the second GRF distributions are retrieved from the measured cross-spectral density across the observation plane that is perpendicular to the optical axis. It is known that Walther's first GRF well conserves along rays particularly in the paraxial resume. Therefore, the first GRF is useful in such as a tomography rather than for 3-D imaging. In contrast, conservation of the second GRF is much worse than that of the first except for the limit of short wavelength. The second GRF is thus useful for 3-D imaging. One advantage of this method is the rapidity of required processing. Retrieving the 3-D image by this method is completed much faster than the method based on retrieving sequential cross-spectral densities.

The principle of the 3-D imaging technique is given by summarizing the relation between Walther's first and second definitions of GRF and the cross-spectral density in Section 6.2. The point spread functions (PSFs) of the proposed imaging technique are also derived. Next, numerically calculated examples of GRF images are presented, and differences between the first and second GRFs are discussed in Section 6.3. The results of experimental demonstrations conducted by incorporating uncorrelated two point sources are shown in Section 6.4. Although the Walther's second GRF is originally defined as a real part of the complex radiance function,[78] we also deal with the magnitude of the complex radiance function. The retrieved 3-D image displayed by the magnitude of the complex radiance function clearly designates the source location compared with that displayed by the real part of the complex radiance function.

6.2 Formulation of principle

The principle of the present imaging technique is based on the propagation law of cross-spectral density in the four-dimensional spatial-frequency domain and the relationship between the cross-spectral density and Walther's radiance functions. These materials are common in literature on radiometry and coherence, so we quickly summarize the relevant part of the theory, which we use to describe the optical system in the geometry illustrated in Fig. 6.1. We assume planar, quasi-monochromatic light sources in a source plane located at $z = z_s > 0$ and an observation plane at $z = 0$ which is parallel to the source plane. The origin of the coordinate system is on the observation plane. The forward and the inverse propagation laws of the angular cross-spectral density are then represented by

$$\tilde{W}^{(0)}(\boldsymbol{k}'_\perp, \boldsymbol{k}_\perp; \nu) = \exp\left[i(k_z - k'_z)z\right] \tilde{W}^{(z)}(\boldsymbol{k}'_\perp, \boldsymbol{k}_\perp; \nu)\,, \tag{6.1}$$

and

$$\tilde{W}^{(z)}(\boldsymbol{k}'_\perp, \boldsymbol{k}_\perp; \nu) = \exp\left[-i(k_z - k'_z)z\right] \tilde{W}^{(0)}(\boldsymbol{k}'_\perp, \boldsymbol{k}_\perp; \nu)\,, \tag{6.2}$$

as described in Section 4.2. Next, we introduce GRF over the reference plane at z. Walther's first GRF[105] is defined by

$$B^{(z)}_{\mathrm{1st}}(\boldsymbol{r}_\perp, \boldsymbol{s}; \nu)$$

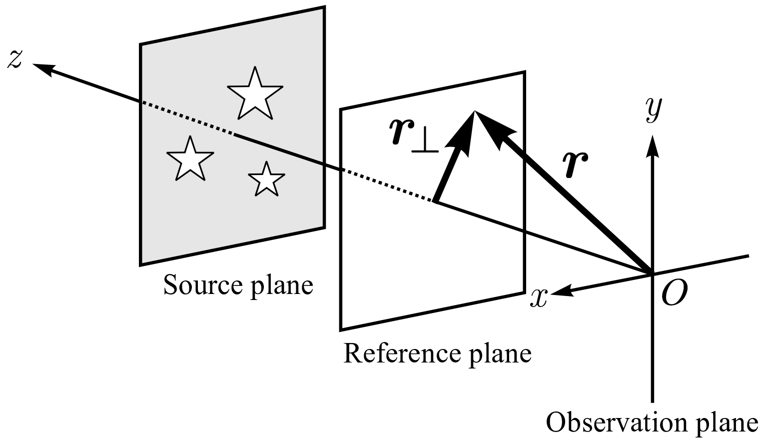

Fig. 6.1. Geometry of optical system considered.

$$
\begin{aligned}
&= |s_z| \left(\frac{k}{2\pi}\right)^2 \iint_{-\infty}^{\infty} W^{(z)}(\boldsymbol{r}_\perp - \boldsymbol{\rho}_\perp/2, \boldsymbol{r}_\perp + \boldsymbol{\rho}_\perp/2; \nu) \exp(-i\boldsymbol{k}_\perp \cdot \boldsymbol{\rho}_\perp) d^2\rho_\perp \\
&= |s_z| \left(\frac{k}{2\pi}\right)^2 \iint_{-\infty}^{\infty} \tilde{W}^{(z)}(\boldsymbol{k}_\perp - \boldsymbol{q}_\perp/2, \boldsymbol{k}_\perp + \boldsymbol{q}_\perp/2; \nu) \exp(i\boldsymbol{q}_\perp \cdot \boldsymbol{r}_\perp) d^2q_\perp, \quad (6.3)
\end{aligned}
$$

where $\boldsymbol{s} = (\boldsymbol{s}_\perp, s_z) = (s_x, s_y, s_z) = \boldsymbol{k}/|\boldsymbol{k}|$. The complex radiance function is defined by

$$
\begin{aligned}
B_{\mathrm{c}}^{(z)}(\boldsymbol{r}_\perp, \boldsymbol{s}; \nu) &= |s_z| \left(\frac{k}{2\pi}\right)^2 \iint_{-\infty}^{\infty} W^{(z)}(\boldsymbol{r}_\perp, \boldsymbol{r}_\perp + \boldsymbol{\rho}_\perp; \nu) \exp(-i\boldsymbol{k}_\perp \cdot \boldsymbol{\rho}_\perp) d^2\rho_\perp \\
&= |s_z| \left(\frac{k}{2\pi}\right)^2 \iint_{-\infty}^{\infty} \tilde{W}^{(z)}(\boldsymbol{k}_\perp - \boldsymbol{q}_\perp, \boldsymbol{k}_\perp; \nu) \exp(i\boldsymbol{q}_\perp \cdot \boldsymbol{r}_\perp) d^2q_\perp \ . \quad (6.4)
\end{aligned}
$$

The real part of the complex radiance function coincide with the Walther's original definition of the second GRF.[106] Using Eqs. (2.44) and (6.1), the cross-spectral density across an arbitrary transverse plane is retrieved using the measured cross-spectral density across the observation plane, and both the first GRF and the complex radiance function across the arbitrary transverse plane can finally be obtained directly from the measured cross-spectral density:

$$
\begin{aligned}
B_{\mathrm{1st}}^{(z)}(\boldsymbol{r}_\perp, \boldsymbol{s}; \nu) \;=\; & |s_z| \left(\frac{k}{2\pi}\right)^2 \iint_{-\infty}^{\infty} \tilde{W}^{(0)}(\boldsymbol{k}_\perp - \boldsymbol{q}_\perp/2, \boldsymbol{k}_\perp + \boldsymbol{q}_\perp/2; \nu) \\
& \times \exp\left[i\boldsymbol{q}_\perp \cdot \boldsymbol{r}_\perp - i(\kappa_{\mathrm{1st}}^{(+)} - \kappa_{\mathrm{1st}}^{(-)})z\right] d^2q_\perp \ , \quad (6.5)
\end{aligned}
$$

and

$$
\begin{aligned}
B_{\mathrm{c}}^{(z)}(\boldsymbol{r}_\perp, \boldsymbol{s}; \nu) \;=\; & |s_z| \left(\frac{k}{2\pi}\right)^2 \iint_{-\infty}^{\infty} \tilde{W}^{(0)}(\boldsymbol{k}_\perp - \boldsymbol{q}_\perp, \boldsymbol{k}_\perp; \nu) \\
& \times \exp\left[i\boldsymbol{q}_\perp \cdot \boldsymbol{r}_\perp - i(k_z - \kappa_{\mathrm{c}})z\right] d^2q_\perp \ , \quad (6.6)
\end{aligned}
$$

where

$$
\kappa_{\mathrm{1st}}^{(\pm)} = -[k^2 - (\boldsymbol{k}_\perp \pm \boldsymbol{q}_\perp/2)^2]^{1/2} \ , \quad (6.7)
$$

and

$$
\kappa_{\mathrm{c}} = -\left[k^2 - (\boldsymbol{k}_\perp - \boldsymbol{q})^2\right]^{1/2} \ . \quad (6.8)
$$

Retrieved radiance functions reflect the intensity distribution. Let us consider radiance functions for the quasi-homogeneous source. The assumption of quasi-homogeneity implies that the spectral density $S^{(z_s)}(\boldsymbol{r}_\perp;\nu)$ varies much more slowly than the effective correlation length which is characterized by the spectral degree of coherence $\mu^{(z_s)}(\boldsymbol{r}_\perp;\nu)$, and the first GRF at z can be then written by

$$B^{(z)}_{\mathrm{1st}}(\boldsymbol{r}_\perp,\boldsymbol{s}) = |s_z|\left(\frac{k}{2\pi}\right)^2 S^{(z)}(\boldsymbol{r}_\perp;\nu)\tilde{\mu}^{(z)}(\boldsymbol{k};\nu)\,, \tag{6.9}$$

and the complex radiance function can be written by

$$\begin{aligned} &B^{(z)}_{\mathrm{c}}(\boldsymbol{r}_\perp,\boldsymbol{s}) \\ &\quad= |s_z|\left(\frac{k}{2\pi}\right)^2 \iint_{-\infty}^{\infty} S^{(z)}(\boldsymbol{r}_\perp+\boldsymbol{\rho}_\perp/2;\nu)\mu^{(z)}(\boldsymbol{\rho}_\perp;\nu)\exp(-i\boldsymbol{k}_\perp\cdot\boldsymbol{\rho}_\perp;\nu)d^2\rho_\perp\,, \end{aligned} \tag{6.10}$$

where $\tilde{\mu}(\boldsymbol{k};\nu)$ is the two-dimensional Fourier transform of the spectral degree of coherence. In a special case where the source field is spatially incoherent, both radiance functions across the source plane are proportional to the intensity distribution as follows:

$$B^{(z)}_{\mathrm{1st}}(\boldsymbol{r}_\perp,\boldsymbol{s}) = B^{(z)}_{\mathrm{c}}(\boldsymbol{r}_\perp,\boldsymbol{s}) = |s_z|\frac{k^2}{(2\pi)^3}S^{(z_s)}(\boldsymbol{r}_\perp;\nu)\,. \tag{6.11}$$

Both the first GRF and the complex radiance function are obtained by taking the two-dimensional Fourier transform of the product of the propagation kernel and the angular cross-spectral density of the observation plane. In a practical experiment, the cross-spectral density with respect to all pairs of points $(\boldsymbol{r}'_\perp,\boldsymbol{r}_\perp)$ within the observation area may be measured using a rotational-share interferometer or a wavefront folding interferometer. Therefore, the four-dimensional Fourier transform of the measured cross-spectral density with respect to $\boldsymbol{r}_\perp$ and $\boldsymbol{r}'_\perp$ must be taken. After taking the Fourier transform, successive applications of Eq. (6.5) or Eq. (6.6) by changing z give sequential distributions of the first GRF or the complex radiance function over the

x-y-z space. It should be noted that the selected direction of $\boldsymbol{s}$ in Eq. (6.5) must not be $(0,0,-1)$ for 3-D imaging because the first GRF is independent of the propagation distance z when $\boldsymbol{s}_\perp = (0,0)$. This implies that the first GRF with respect to a direction parallel to the optical axis is completely conserved as propagating in free space.

Next, we derive PSFs of the retrieved first GRF and the complex radiance function. Let us assume a primary point source at $\boldsymbol{r}_s = (\boldsymbol{r}_{s\perp}, z_s) = (x_s, y_s, z_s)$. The cross-spectral density across the primary source plane is then represented by

$$\Omega^{(z_s)}(\boldsymbol{r}'_\perp, \boldsymbol{r}_\perp; \nu) = \Omega_o \delta^2\left(\frac{\boldsymbol{r}_\perp + \boldsymbol{r}'_\perp}{2} - \boldsymbol{r}_{s\perp}\right)\delta^2(\boldsymbol{r}_\perp - \boldsymbol{r}'_\perp)\ , \tag{6.12}$$

where $\delta^2(\boldsymbol{r}_\perp)$ is the Dirac delta function and Ω_o is a positive constant. The angular cross-spectral density across the source plane is obtained by taking the four-dimensional Fourier transform of $\Omega^{(z_s)}(\boldsymbol{r}'_\perp, \boldsymbol{r}_\perp; \nu)$:

$$\tilde{\Omega}^{(z_s)}(\boldsymbol{k}'_\perp, \boldsymbol{k}_\perp; \nu) = \frac{\Omega_o}{(2\pi)^2}\exp\left[-i(\boldsymbol{k}_\perp - \boldsymbol{k}'_\perp)\cdot \boldsymbol{r}_{s\perp}\right]\ . \tag{6.13}$$

Hence, the angular cross-spectral density of the source field is represented as[86]

$$\tilde{W}^{(z_s)}(\boldsymbol{k}'_\perp, \boldsymbol{k}_\perp; \nu) = \frac{(2\pi)^2}{k_z k'_z}\tilde{\Omega}^{(z_s)}(\boldsymbol{k}'_\perp, \boldsymbol{k}_\perp; \nu) = \frac{\Omega_o}{k_z k'_z}\exp\left[-i(\boldsymbol{k}_\perp - \boldsymbol{k}'_\perp)\cdot \boldsymbol{r}_{s\perp}\right]\ . \tag{6.14}$$

The angular cross-spectral density across the observation plane can be written as a product of $\tilde{W}^{(z_s)}(\boldsymbol{k}'_\perp, \boldsymbol{k}_\perp; \nu)$ and the propagation kernel based on Eq. (6.1) as

$$\begin{aligned}\tilde{W}^{(0)}(\boldsymbol{k}'_\perp, \boldsymbol{k}_\perp; \nu) &= \exp\left[i(k_z - k'_z)z_s\right]\tilde{W}^{(z_s)}(\boldsymbol{k}'_\perp, \boldsymbol{k}_\perp; \nu) \\ &= \frac{\Omega_o}{k_z k'_z}\exp\left[i(k_z z_s - \boldsymbol{k}_\perp\cdot \boldsymbol{r}_{s\perp}) - i(k'_z z_s - \boldsymbol{k}'_\perp\cdot \boldsymbol{r}_{s\perp})\right]\ . \end{aligned}\tag{6.15}$$

Taking the four-dimensional inverse Fourier transform of $\tilde{W}^{(0)}(\boldsymbol{k}'_\perp, \boldsymbol{k}_\perp; \nu)$ yields the cross-spectral density across the observation plane:

$$\begin{aligned}W^{(0)}(\boldsymbol{r}'_\perp, \boldsymbol{r}_\perp; \nu) &= \frac{1}{(2\pi)^2}\iiiint_{-\infty}^{\infty}\tilde{W}^{(0)}(\boldsymbol{k}'_\perp, \boldsymbol{k}_\perp; \nu)\exp\left[i(\boldsymbol{k}_\perp\cdot \boldsymbol{r}_\perp - \boldsymbol{k}'_\perp\cdot \boldsymbol{r}'_\perp)\right]d^2k_\perp d^2k'_\perp \\ &= \Omega_o f^*(\boldsymbol{r}'_\perp - \boldsymbol{r}_{s\perp})f(\boldsymbol{r}_\perp - \boldsymbol{r}_{s\perp})\ ,\end{aligned}\tag{6.16}$$

where

$$f(\boldsymbol{r}_\perp) = \iint_{-\infty}^{\infty} \frac{1}{2\pi|k_z|} \exp\left[i(k_z z_s + \boldsymbol{k}_\perp \cdot \boldsymbol{r}_\perp)\right] d^2k_\perp \, . \tag{6.17}$$

Let us now use a paraxial approximation with respect to k_z and k'_z derived by the Tailor series:

$$k_z \simeq -k + \frac{\boldsymbol{k}_\perp^2}{2k} \, , \tag{6.18}$$

then $f(\boldsymbol{r}_\perp)$ is written as

$$f(\boldsymbol{r}_\perp) \simeq \frac{i}{z_s} \exp(-ikz_s) \exp\left(-\frac{ik}{2z_s}\boldsymbol{r}_\perp^2\right) \, . \tag{6.19}$$

On substituting Eq. (6.19) into Eq. (6.16), the cross-spectral density across the observation plane is rewritten as

$$W^{(0)}(\boldsymbol{r}'_\perp, \boldsymbol{r}_\perp; \nu) = \frac{\Omega_o}{z_s^2} \exp\left\{\frac{ik}{2z_s}\left[(\boldsymbol{r}'_\perp - \boldsymbol{r}_{s\perp})^2 - (\boldsymbol{r}_\perp - \boldsymbol{r}_{s\perp})^2\right]\right\} \, . \tag{6.20}$$

In a practical measurement of the cross-spectral density, the range of $\boldsymbol{r}_\perp$ and $\boldsymbol{r}'_\perp$ is limited by the linear dimension of a photodetector array. Therefore, the measured cross-spectral density is represented by a product of $W^{(0)}(\boldsymbol{r}'_\perp, \boldsymbol{r}_\perp; \nu)$ and the transmission function $A(\boldsymbol{r}_\perp)$ as

$$W_{\mathrm{m}}^{(0)}(\boldsymbol{r}'_\perp, \boldsymbol{r}_\perp; \nu) = A(\boldsymbol{r}'_\perp) W^{(0)}(\boldsymbol{r}'_\perp, \boldsymbol{r}_\perp; \nu) A(\boldsymbol{r}_\perp) \, . \tag{6.21}$$

Note that $A(\boldsymbol{r}_\perp)$ is a real function and takes 1 in the measurement area and 0 outside. The four-dimensional Fourier transform of the measured cross-spectral density is then represented by

$$\begin{aligned} \tilde{W}_{\mathrm{m}}^{(0)}(\boldsymbol{k}'_\perp, \boldsymbol{k}_\perp; \nu) &= \frac{\Omega_o}{(2\pi z_s)^2} \iiiint_{-\infty}^{\infty} A(\boldsymbol{r}_\perp) A(\boldsymbol{r}'_\perp) \\ &\quad \times \exp\left\{\frac{ik}{2z_s}\left[(\boldsymbol{r}'_\perp - \boldsymbol{r}_{s\perp})^2 - (\boldsymbol{r}_\perp - \boldsymbol{r}_{s\perp})^2\right]\right\} \\ &\quad \times \exp[-i(\boldsymbol{k}_\perp \cdot \boldsymbol{r}_\perp - \boldsymbol{k}'_\perp \cdot \boldsymbol{r}'_\perp)] d^2r_\perp d^2r'_\perp \, . \end{aligned} \tag{6.22}$$

Making the paraxial approximation shown in Eq. (6.18), the first GRF and the complex radiance function are represented by

$$\begin{aligned} B_{\text{1st}}^{(z)}(\boldsymbol{r}_\perp, \boldsymbol{s}; \nu) &= |s_z| \left(\frac{k}{2\pi}\right)^2 \iint_{-\infty}^{\infty} \tilde{W}^{(0)}(\boldsymbol{k}_\perp - \boldsymbol{q}_\perp/2, \boldsymbol{k}_\perp + \boldsymbol{q}_\perp/2; \nu) \\ &\qquad \times \exp\left[i\boldsymbol{q}_\perp \cdot (\boldsymbol{r}_\perp - \boldsymbol{s}_\perp z)\right] d^2 q_\perp \, , \end{aligned} \tag{6.23}$$

and

$$\begin{aligned} B_{\text{c}}^{(z)}(\boldsymbol{r}_\perp, \boldsymbol{s}; \nu) &= |s_z| \left(\frac{k}{2\pi}\right)^2 \iint_{-\infty}^{\infty} \tilde{W}^{(0)}(\boldsymbol{k}_\perp - \boldsymbol{q}_\perp, \boldsymbol{k}_\perp; \nu) \exp\left[i\boldsymbol{q}_\perp \cdot (\boldsymbol{r}_\perp - \boldsymbol{s}_\perp z)\right] \\ &\qquad \times \exp\left\{\frac{iz}{2k}\left[\boldsymbol{q}_\perp^2 + (\boldsymbol{s}_\perp \cdot \boldsymbol{q}_\perp)^2\right]\right\} d^2 q_\perp \, . \end{aligned} \tag{6.24}$$

As a simple example, let us assume that the source is located at $(x_s, 0, z_s)$ and that the cross-spectral density along only the x axis is measured within a baseline length of D. The transmission function is then represented by

$$A(\boldsymbol{r}_\perp) = \text{rect}\left(\frac{x}{D}\right)\delta(y) \, . \tag{6.25}$$

To derive PSFs of the first GRF and the complex radiance function, we set $z = z_s$ in Eqs. (6.23) and (6.24). Moreover, we consider the first GRF and the complex radiance function with respect to the fixed direction $\boldsymbol{s} = (0, 0, -1)$ for simplicity. Under these circumstances, we obtain the PSF of the first GRF over the x-z plane by substituting Eqs. (6.22) and (6.25) into Eq. (6.23) as follows:

$$B_{\text{1st,m}}^{(z_s)}(x, 0) = \frac{\Omega_o D}{2}\left(\frac{k}{\pi z_s}\right)^2 \text{rect}\left(\frac{x}{D}\right) \frac{\sin\left\{\dfrac{k}{z_s}(D - 2|x|)[x - x_s]\right\}}{\dfrac{kD}{z_s}[x - x_s]} \, , \tag{6.26}$$

and the PSF of the complex radiance function is similarly derived by substituting Eqs. (6.22) and (6.25) into Eq. (6.24) as

$$\begin{aligned} B_{\text{c,m}}^{(z_s)}(x, 0) &= \Omega_o \left(\frac{k}{2\pi z_s}\right)^{5/2} \exp\left(\frac{i\pi}{4}\right)\left[F(\alpha^{(+)}) - F(\alpha^{(-)})\right] \\ &\qquad \times \exp\left[-\frac{ik}{2z_s}\left(x^2 - x_s^2\right)\right] \text{sinc}\left[\frac{kD}{2z_s}(x - x_s)\right] \end{aligned} \tag{6.27}$$

where

$$F(\alpha) = \frac{1}{1-i}\int_{-\infty}^{\alpha} \exp\left(-\frac{i\pi\tau^2}{2}\right) d\tau \,, \tag{6.28}$$

and

$$\alpha^{(\pm)} = \sqrt{\frac{k}{\pi z_s}}\left(\pm\frac{D}{2} - x_s\right) \,. \tag{6.29}$$

Based on the results expressed in Eqs. (6.26) and (6.27), profiles of PSFs of the first GRF, the real part, and the magnitude of the complex radiance function are plotted in Fig. 6.2 (a), (b), and (c), respectively, for source locations of $x_s = 0$ mm, 0.3 mm, and 0.6 mm. Other parameters used are $k = 9,929$ rad/mm, $D = 2.4$ mm, and $z_s = 110$ mm. Each power is normalized by the peak of the first PSF for $x_s = 0$, namely, in the case that the point source is located on the optical axis. As seen from Fig. 6.2 (a), the peak of the PSF of the first GRF becomes lower and the width broadens as the source location moves away from the optical axis. When the point source is located apart form the optical axis, the period of oscillation is asymmetric to the peak of the PSF, and oscillation of the left side of the peak is faster than that of the right side. Since the first GRF with $\boldsymbol{s} = (0, 0, -1)$ is independent of z, the same profile as Fig. 6.2 (a) is exhibited by the retrieved first GRF across any plane perpendicular to the optical axis. In contrast, widths of PSFs of the real part and the magnitude of the complex radiance function are almost unchanged when the source moves. Height differences of PSFs shown in Figs. 6.2 (b) and (c) are caused by the Fresnel integral term $F(\alpha^{(+)}) - F(\alpha^{(-)})$.

Next, let us confine ourselves to the resolving power along the x axis. The FWHM of PSFs of the first GRF, the real part, and the magnitude of the complex radiance function for $x_s = 0$ mm are, respectively, 0.0175 mm, 0.035 mm, and 0.035 mm under the same conditions as Fig. 6.2. This means that the resolving power of the first

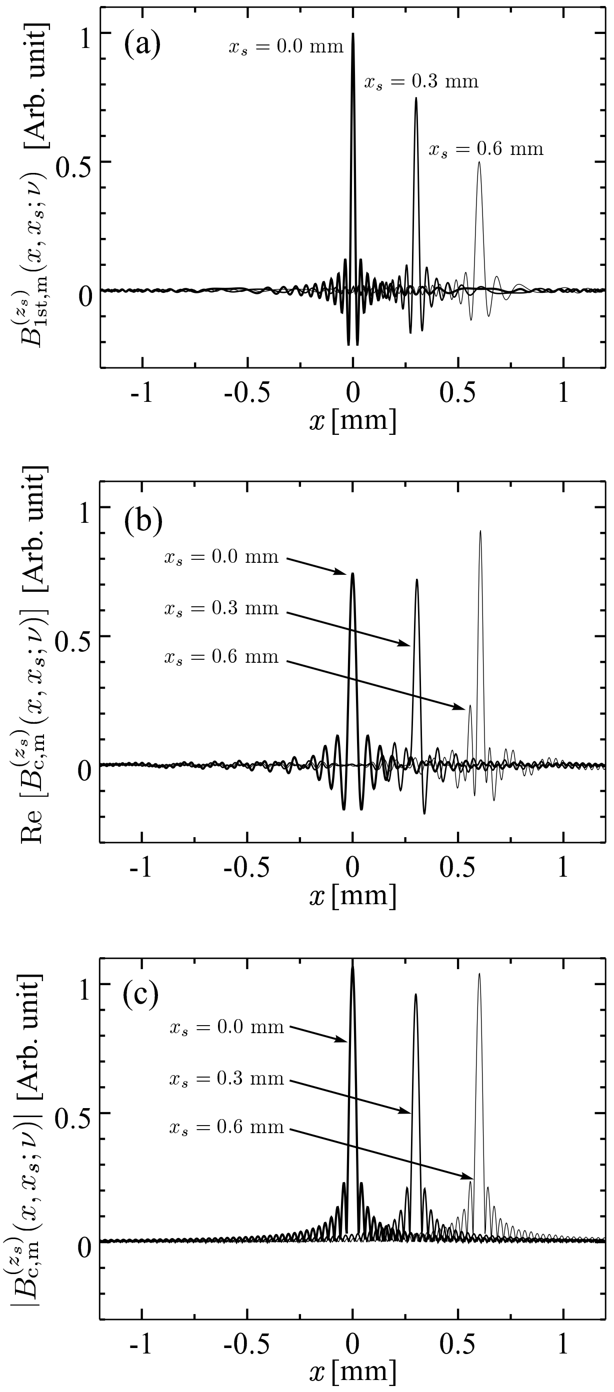

Fig. 6.2. PSFs of (a) the first GRF, (b) the real part of the complex radiance function for the source location $s_x = 0$ mm, 0.3 mm, and 0.6 mm, and (c) the magnitude of the complex radiance function for the same s_x's as (b).

GRF along the x axis is the highest in those of three radiance functions for an object on the optical axis. However, PSF of the first GRF broadens as the source location shifts away from the optical axis as stated above, whereas the width of PSF of the magnitude of the complex radiance function is invariant within the paraxial area. The width in the PSF of the real part of the complex radiance function changes somewhat owing to the quadratic phase term.

6.3 Numerical calculation

Based on the mathematical formulation stated in Section 6.2, we will show the numerical examples of the retrieved radiance functions for a particular case. Assumed coordinate system and geometry are the same as those shown in Fig. 6.1. We assume monochromatic, spatially incoherent planar sources in a source plane located at $z = z_s = 100,000$ mm (100 m). The intensity distribution across the source plane is binary as shown in Fig. 6.3 (a). A region 2.4 mm square within the source plane is considered, and radiance distributions are calculated over the same area. The wavelength of light is assumed to be 632.8 nm.

As a beginning, the first GRF and the real part of the complex radiance function for fixed $\boldsymbol{s}$'s across the observation plane are calculated under these circumstances, and the results are shown in Figs. 6.3 (b) and (c). Since gray-levels are normalized by each maximum and minimum of the calculated radiance functions, the zero-levels differ. The direction $\boldsymbol{s}$ for the first GRF is set to $(1/2, 0, -\sqrt{3}/2)$, namely, the angle between $\boldsymbol{s}$ and the optical axis is 30° on the x-z plane. Remember that the first GRF for $\boldsymbol{s} = (0, 0, -1)$ is independent of the propagation distance, and the same image as the original source intensity will be obtained across any transverse planes. The direction of $\boldsymbol{s}$ for the complex radiance function is set to $(0, 0, -1)$. It is seen from Fig. 6.3 (b) that the image retrieved as the first GRF exhibits shapes of three starred source with periodic oscillation that appears toward $\boldsymbol{s}_\perp$. In contrast, the complex radiance function expands to the entire image.

Next, we inversely propagate the first GRF and the complex radiance function across the reference plane that is separated from the observation plane by 99,900 mm (99.9 m), that is, 100 mm from the source plane. The retrieved images are shown in Figs. 6.3 (d), (e), and (f). Figures 6.3 (e) and (f) are, respectively, the real part and the magnitude of the complex radiance function. As seen from Fig. 6.3 (d), the image retrieved as the first GRF almost coincides with the original source intensity though the contrast is lower than that of Fig. 6.3 (a) because of minute oscillation around the edge of the sources. The complex radiance functions shown in Figs. 6.3 (e) and (f) barely exhibited the three starred sources, but, images are much blurred compared with the first GRF. The calculated results of radiance functions across the source plane are omitted because they are simply proportional to the source intensity as obvious from Eq. (6.11).

Differences between the first GRF and the complex radiance function imply the conservation characteristics of the radiance functions. As obvious from simulation results shown in this section, the conservation of the complex radiance function along $\boldsymbol{s}$ is much worse than that of the first GRF. In other words, the retrieved image as the complex radiance function is considerably blurred when $z \neq z_s$. The large angle between $\boldsymbol{s}$ and the optical axis makes the first GRF more blurred, but it may be impracticable to measure the cross-spectral density to retrieve the first GRF with an extremely large angle. For this reason, the complex radiance function is more useful than the first GRF for 3-D imaging.

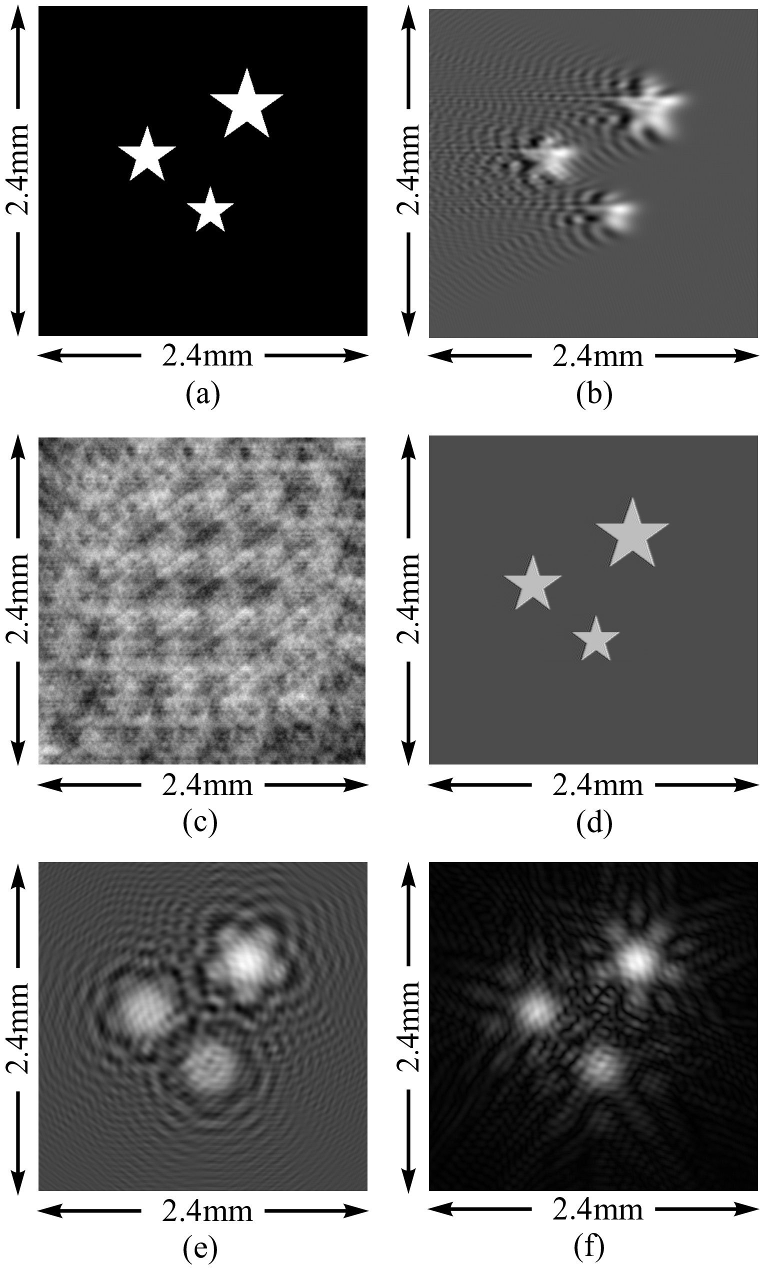

Fig. 6.3. (a) Intensity distribution of primary sources assumed for the computer simulation. (b) Spatial distribution of Walther's first definition of GRF 100,000 mm from the source plane and (c) the real part of the complex radiance function at the same distance as (b). (d) The first GRF 100 mm from the source plane, (e) the real part, and (f) the magnitude of the complex radiance function at the same distance as (d).

6.4 Experimental demonstration

In this section, we report the results of an experimental demonstration for retrieving the spatial distribution of the first GRF and the complex radiance function. The experimental system and parameters were same as that presented in Chapter 5, namely the cross-spectral density across the observation plane which is illuminated by mutually uncorrelated two optical fibers was measured by the wavefront folding interferometer. Taking the two-dimensional Fourier transform of the measured cross-spectral density with respect to x and x' gives the angular cross-spectral density as a function of k_x and k'_x. Using this angular cross-spectral density, we retrieve Walther's first GRF and the complex radiance function with respect to the fixed direction $\boldsymbol{s} = (0, 0, -1)$. The retrieved first GRF is plotted in Fig. 6.4 as a function of x. As pointed out in Section 6.2, the first GRF with $\boldsymbol{s}_\perp = (0, 0)$ is independent of the propagating distance z. Thus, two sharp peaks appear in Fig. 6.4 though the sources are located in different distances from the observation plane. In other words, the first GRF with $\boldsymbol{s}_\perp = (0, 0)$ is conserved completely as it is propagating. It should be noted that the intensity distribution retrieved based on the van Cittert-Zernike theorem is given as a function of an angle seen from the observation point unless the source distance is known in advance, however, the two-point separation (0.8 mm, in this case) is obtained by the first GRF without the source distance.

Next, the retrieved complex radiance function is shown. Unlike the first GRF, the complex radiance function depends on the propagating distance z. A sequence of spatial distributions of the complex radiance function along the x axis from $z = 0$ mm to $z = 200$ mm is calculated based on Eq. (6.6). The real part and the magnitude of the complex radiance function are shown in Figs. 6.5 (a) and (b). Locations of two

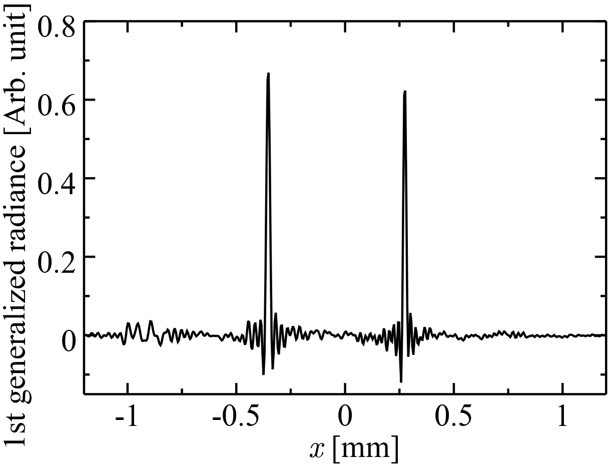

Fig. 6.4. Retrieved first GRF as a function of x.

tips of optical fibers are retrieved almost exactly as higher values (white regions) in both figures. The cross sections of Figs. 6.5 (a) and (b) at $z = 110$ mm and 130 mm, in which two point sources are located, are shown in Figs. 6.6 (a), (b), (c), and (d). Sharp peaks in each graph represent focused sources. The oscillation appearing in Fig. 6.5 (a) is reduced in Fig. 6.5 (b), and it is also seen from Figs. 6.6 (a), (b), (c), and (d). Although we suggested that 3-D imaging is possible by using the first GRF with respect to the direction $\boldsymbol{s}_\perp \neq (0, 0)$, the first GRF and the complex radiance function with $\boldsymbol{s}_\perp = (0, 0)$ were shown as experimental results. As seen from Eqs. (6.5) and (6.7), the first GRF is well conserved in the direction of $\boldsymbol{s}$. However retrieving the first GRF with large $|\boldsymbol{s}_\perp|$ requires measuring the cross-spectral density with an extremely high spatial resolution.

In Chapter 5, a new interferometric 3-D imaging technique based on retrieving sequential cross-spectral densities within the considered slab geometry was proposed. The processing time required for calculating the intensity distribution by this method and the distribution of the complex radiance function over the x-z plane was com-

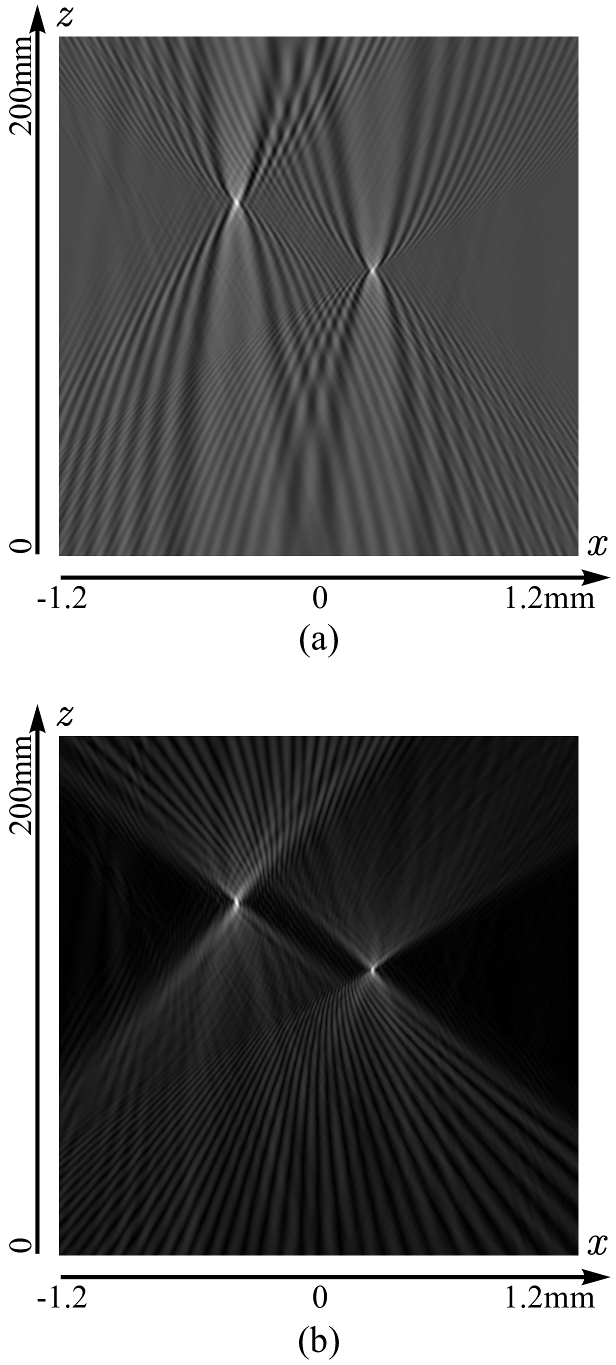

Fig. 6.5. (a) Retrieved real part of the complex radiance function and (b) the magnitude of the complex radiance function on the x-z plane

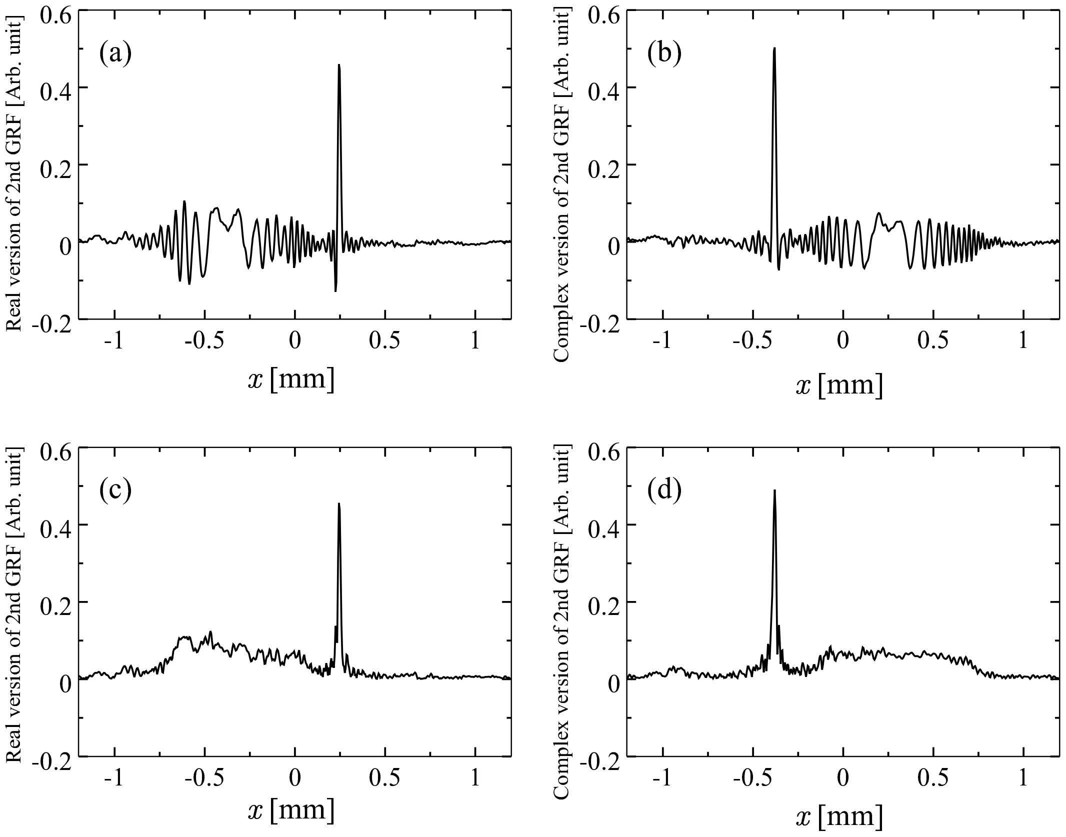

Fig. 6.6. Cross sections of the complex radiance function across source planes. (a) The real part at $z = 110$ mm and (b) $z = 130$ mm, and (c) the magnitude at $z = 110$ mm and (d) $z = 130$ mm.

pared. It took 3,483 seconds to calculate the sequential cross-spectral density and the intensity distribution, in contrast the distributions of the complex radiance function shown in Figs. 6.5 (a) and (b) were calculated 8 seconds over the same slab geometry using a personal computer (CPU: Intel PentiumII 450MHz, OS: FreeBSD 2.2.8RELEASE). To retrieve sequential cross-spectral densities over the x-z space, two-dimensional FFT and two-dimensional inverse FFT must be performed at every z coordinate successively. In the present method, however, the two-dimensional

FFT is required only once, and a radiance distribution at a particular z-coordinate is given by one-dimensional FFT. Hence the processing time for these two methods much differs.

6.5 Conclusion

A new three-dimensional imaging technique based on retrieving Walther's first and second definitions of the generalized radiance function was presented. The spatial distributions of these two types of generalized radiances can be calculated from the cross-spectral density propagated from primary sources in free space using the propagation law of the cross-spectral density described in the spatial-frequency domain. An experimental demonstration of this imaging method was conducted by incorporating uncorrelated two point sources. The three-dimensional locations of sources were retrieved almost exactly as a spatial distribution of Walther's second definition of the generalized radiance. Walther's first definition of the generalized radiance showed the two point separation along the direction perpendicular to the optical axis. However, the longitudinal resolution is much worse than that of the second generalized radiance under the same conditions. Mathematical formulations of the proposed method were given and the point spread functions were also derived.

Chapter 7

Noise-limitations of interferometric imaging

7.1 Introduction

We studied new interferometric imaging methods that are based on the inverse propagation law of the angular cross-spectral density in Chapters 4,5 and 6. It is essential to evaluate the signal-to-noise ratio (SNR) of this 3-D imaging system. In this chapter, we first estimate SNR theoretically in two noise-limiting cases, that is, the photon-noise-limit and the detector-noise-limit.[107, 108] As is well known, the photon-noise that is generated in the photodetector depends on the input optical intensity and, on the other hand, the detector-noise is independent of the input intensity. We will derive SNR in these two cases for the wavefront folding interferometer which enables us to measure the cross-spectral density propagating from the source. After measuring images of the interference fringe, the cross-spectral density is obtained by using the FFT algorithm. The source image is then retrieved by applying the inverse propagation law of the angular cross-spectral density. We will investigate how the noise component propagate through these procedures. To verify the theoretical estimation of SNRs, experiments were conducted and the results are given.

7.2 Theoretical estimation for two noise-limitation cases

In this section, we derive the noise-limitations of the present interferometric imaging system. First, let us review briefly the principle for retrieving the source image with the wavefront folding interferometer.[87, 88] Geometry of the optical system is shown in Fig. 7.1. The observation plane is located at $z = 0$ and the origin of the coordinate system is set on the center of the observation plane. The reference plane and the source plane are located at $z = z_r$ and $z = z_s$, respectively, parallel to the observation plane. The source is assumed to be quasi-monochromatic but there is no requirements for the property of the source correlation.

In a practical experiment, we measure the cross-spectral density across the observation plane by using the wavefront folding interferometer that is illustrated in Fig. 7.2 as presented in Chapters 4, 5, and 6. The mirror is slightly tilted in order to introduce the carrier frequency α into the interference fringe toward the y direction. The

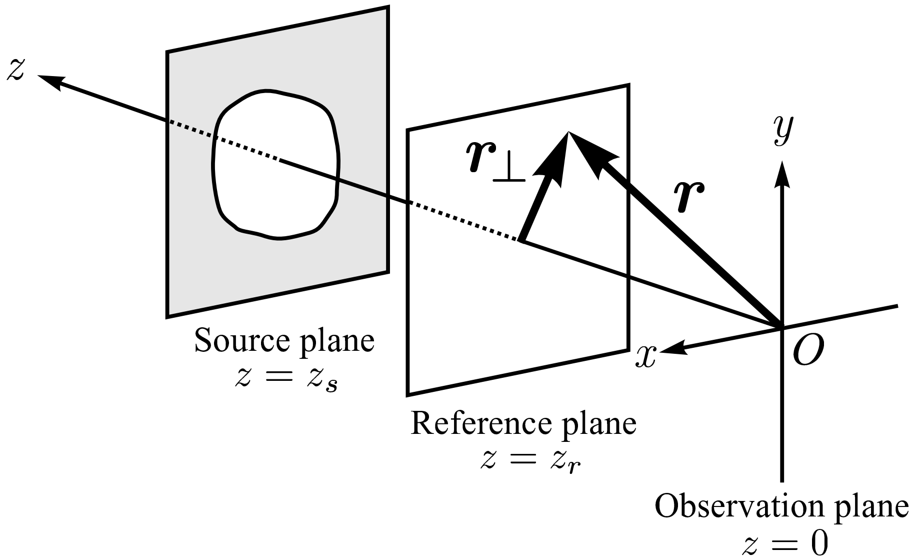

Fig. 7.1. Geometry of the optical system.

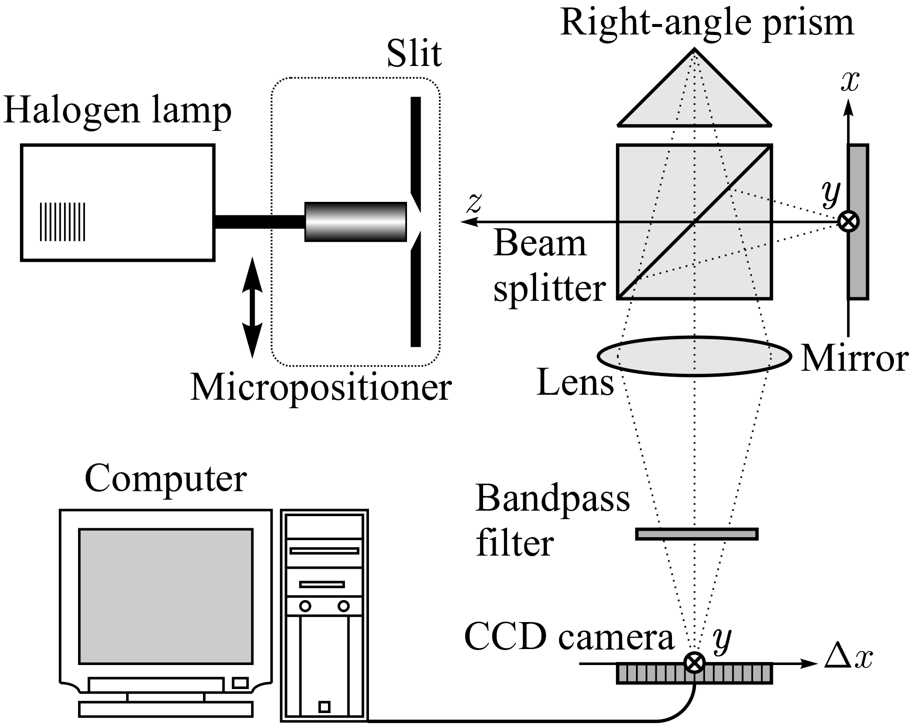

Fig. 7.2. Experimental setup for the interferometric imaging.

coordinate along the CCD camera is $\Delta x = x_1 - x_2$ for a particular average coordinate $\hat{x} = (x_1 + x_2)/2$. The procedure of the experiment for measuring the cross-spectral density was stated in Chapter 4 in detail. Under these circumstances, let us derive the noise-limitation of this system. The intensity distribution on the CCD camera is represented by

$$I_o(\Delta x, \hat{x}, y) = I_N(\Delta x, \hat{x}, y) + I_1(x_1, y) + I_2(x_2, y) + W^{(0)}(\Delta x, \hat{x}; \nu) \exp(i\alpha y) + \text{c.c.}, \quad (7.1)$$

where $I_N(\Delta x, \hat{x}, y)$ is the noise component, $I_1(x_1, y)$ and $I_2(x_2, y)$ are intensity distributions that are measured by stopping one of the beams from the mirror and the prism, and c.c. denotes the complex conjugate. Note that Δx, $\hat{x}$, and y are integer variables. Since we assume that the source spectrum is quasi-monochromatic, the spectral densities that appear in the spectral interference law[1] is replaced by the intensities. To obtain the cross-spectral density from the interference fringe, we extract the carrier frequency component in the spatial-frequency domain. We use the discrete Fourier transform in the following derivation because the practical procedures are performed with the FFT algorithm. The Fourier transform of Eq. (7.1) with respect to y is

$$\begin{aligned}\tilde{I}_o(\Delta x, \hat{x}, f) &= \sum_{y=0}^{Y-1} I_o(\Delta x, \hat{x}, y) \exp\left(\frac{2\pi i f y}{Y}\right) \\ &= \tilde{I}_N(\Delta x, \hat{x}, f) + \tilde{I}_1(x_1, f) + \tilde{I}_2(x_2, f) \\ &\quad + W^{(0)}(\Delta x, \hat{x}; \nu)\delta(f-\alpha) + W^{(0)*}(\Delta x, \hat{x}; \nu)\delta(f+\alpha)\,, \qquad (7.2)\end{aligned}$$

where the tilde denotes the discrete Fourier transform. $\tilde{I}_1(x_1, f)$ and $\tilde{I}_2(x_2, f)$ appear around $f = 0$ because $I_1(x_1, y)$ and $I_2(x_2, y)$ are almost uniform over the observation plane. The carrier frequency component $\tilde{I}_o(\Delta x, \hat{x}, \alpha)$ in the spatial-frequency domain can be expressed by

$$\tilde{I}_o(\Delta x, \hat{x}, \alpha) = \tilde{I}_N(\Delta x, \hat{x}, \alpha) + W^{(0)}(\Delta x, \hat{x}; \nu)\,. \qquad (7.3)$$

Here, we rewrite $\tilde{I}_o(\Delta x, \hat{x}, \alpha)$ by $W^{(0)}_{\mathrm{m}}(\Delta x, \hat{x}; \nu)$ and $\tilde{I}_N(\Delta x, \hat{x}, \alpha)$ by $N_\alpha(\Delta x, \hat{x})$. Equation (7.3) is then rewritten as

$$W^{(0)}_{\mathrm{m}}(\Delta x, \hat{x}; \nu) = N_\alpha(\Delta x, \hat{x}) + W^{(0)}(\Delta x, \hat{x}; \nu)\,. \qquad (7.4)$$

The suffix m of W means the measured quantity. Equation (7.4) implies that the cross-spectral density obtained by the above Fourier procedure is represented simply by a summation of the noise component and the original cross-spectral density. To apply the inverse propagation law of the cross-spectral density described by Eq. (4.14), let the measured cross-spectral density be represented in the spatial-frequency domain:

$$\tilde{W}^{(0)}_{\mathrm{m}}(\Delta k_x, \tilde{k}_x; \nu) = \sum_{\Delta x=0}^{M-1} \sum_{\hat{x}=0}^{N-1} W^{(0)}_{\mathrm{m}}(\Delta x, \hat{x}; \nu) \exp\left[-2\pi i \left(\frac{\Delta x \Delta k_x}{M} + \frac{\hat{x}\hat{k}_x}{N}\right)\right]$$

$$= \tilde{N}_\alpha(\Delta k_x, \hat{k}_x) + \tilde{W}^{(0)}(\Delta k_x, \hat{k}_x) \,, \tag{7.5}$$

where $\Delta k_x = k_{1x} - k_{2x}$ and $\hat{k}_x = (k_{1x} + k_{2x})/2$. The Fourier transform of the cross-spectral density across the source plane can be obtained by applying the inverse propagation law with the distance between the observation plane and the source plane:

$$\begin{aligned}
\tilde{W}_{\mathrm{m}}^{(z_s)}(\Delta k_x, \tilde{k}_x; \nu) &= \exp\left[-i(k_{1z} - k_{2z})z_s\right] \tilde{W}_{\mathrm{m}}^{(0)}(\Delta k_x, \tilde{k}_x; \nu) \\
&= \exp\left[-i(k_{1z} - k_{2z})z_s\right] \tilde{N}_\alpha(\Delta k_x, \widetilde{k_x}) + \tilde{W}^{(z_s)}(\Delta k_x, \tilde{k}_x; \nu)
\end{aligned} \tag{7.6}$$

By using the Fourier inverse, the cross-spectral density across the source plane is given as

$$\begin{aligned}
W_{\mathrm{m}}^{(z_s)}(\Delta x, \hat{x}; \nu) &= \frac{1}{MN} \sum_{\Delta k_x = 0}^{M-1} \sum_{\hat{k}_x = 0}^{N-1} \tilde{W}_{\mathrm{m}}^{(z_s)}(\Delta k_x, \tilde{k}_x; \nu) \exp\left[2\pi i \left(\frac{\Delta x \Delta k_x}{M} + \frac{\hat{x}\hat{k}_x}{N}\right)\right] \\
&= \frac{1}{MN} \sum_{\Delta k_x = 0}^{M-1} \sum_{\hat{k}_x = 0}^{N-1} \exp\left[-i(k_{1z} - k_{2z})z_s + 2\pi i \left(\frac{\Delta x \Delta k_x}{M} + \frac{\hat{x}\hat{k}_x}{N}\right)\right] \\
&\quad + W^{(z_s)}(\Delta x, \hat{x}; \nu) \,.
\end{aligned} \tag{7.7}$$

We finally obtain the general formulation of the variance of the retrieved cross-spectral density across the source plane:

$$\begin{aligned}
&\langle |W_{\mathrm{m}}^{(z_s)}(\Delta x, \hat{x}; \nu) - W^{(z)}(\Delta x, \hat{x}; \nu)|^2 \rangle \\
&= \left(\frac{1}{MN}\right)^2 \sum_{\Delta k_x = 0}^{M-1} \sum_{\Delta k'_x = 0}^{M-1} \sum_{\hat{k}_x = 0}^{N-1} \sum_{\hat{k}'_x = 0}^{N-1} \langle \tilde{N}^*_\alpha(\Delta k'_x, \hat{k}'_x) \tilde{N}_\alpha(\Delta k_x, \hat{k}_x) \rangle \\
&\times \exp\left\{-i\left[(k_{1z} - k'_{1z}) - (k_{2z} - k'_{2z})\right] + 2\pi i \left[\frac{\Delta x(\Delta k_x - \Delta k'_x)}{M} + \frac{\hat{x}(\hat{k}_x - \hat{k}'_x)}{N}\right]\right\}.
\end{aligned} \tag{7.8}$$

Next, let us derive the correlation function of the noise component. In case of the detector-noise-limit, the variance of the noise is independent of the input optical intensity. On the other hand, in case of the photon-noise-limit, the variance of the noise is proportional to the input optical intensity. Moreover, in both cases, the noise component is temporally, spatially uncorrelated. Therefore, the correlation function of the noise component can be represented by

$$\langle N_\alpha^*(\Delta x', \hat{x}') N_\alpha(\Delta x, \hat{x})\rangle = \begin{cases} \sigma^2 \delta(\Delta x - \Delta x')\delta(\hat{x} - \hat{x}') & \text{(Detector-noise-limit)} \\ \bar{I}_o \delta(\Delta x - \Delta x')\delta(\hat{x} - \hat{x}') & \text{(Photon-noise-limit)} \end{cases} \tag{7.9}$$

where σ is a constant, and $\bar{I}_o$ is the average intensity over the CCD camera. Since the noise intensity depends on the input optical intensity in the photon-noise-limit, the correlation function also depends on the cross-spectral density across the observation plane in the strict sense. However, the bias intensity $I_1(x_1, y)$ and $I_2(x_2, y)$ is considerably higher because the interference efficiency is reduced by the intensity difference between $I_1(x_1, y)$ and $I_2(x_2, y)$, and the noise intensity is determined mainly by the average intensity over the CCD camera.

The four-dimensional Fourier transform of the correlation function described by Eq. (7.9) with respect to Δx, $\Delta x'$, $\hat{x}$, and $\hat{x}'$ is

$$\begin{aligned} \langle \tilde{N}_\alpha(\Delta k_x', \hat{k}_x') \tilde{N}_\alpha(\Delta k_x, \hat{x})\rangle &= \sum_{\Delta x=0}^{M-1} \sum_{\hat{x}=0}^{N-1} \langle N_\alpha^*(\Delta x', \hat{x}') N_\alpha(\Delta x, \hat{x})\rangle \\ &\times \exp\left[-2\pi i \left(\frac{\Delta x(\Delta k_x - \Delta k_x')}{M} + \frac{\hat{x}(\hat{k}_x - \hat{k}_x')}{N}\right)\right] \\ &= \begin{cases} \sigma^2 \delta(\Delta k_x - \Delta k_x')\delta(\hat{k}_x - \hat{k}_x') & \text{(Detector-noise-limit)} \\ \bar{I}_o \delta(\Delta k_x - \Delta k_x')\delta(\hat{k}_x - \hat{k}_x') & \text{(Photon-noise-limit)} \end{cases} . \end{aligned} \tag{7.10}$$

On substituting from Eq. (7.10) into Eq.(7.8), we finally obtain the variances in the noise-limitations:

$$\langle |W_{\mathrm{m}}^{(z_s)}(\Delta x, \hat{x}; \nu) - W^{(z)}(\Delta x, \hat{x}; \nu)|^2\rangle = \begin{cases} \sigma^2 & \text{(Detector-noise-limit)} \\ \bar{I}_o & \text{(Photon-noise-limit)} \end{cases} . \tag{7.11}$$

According to the above result, SNR is readily written by

$$\mathrm{SNR} = \begin{cases} \dfrac{W^{(z_s)}(\Delta x, \hat{x}; \nu)}{\sigma} & \text{(Detector-noise-limit)} \\ \dfrac{W^{(z_s)}(\Delta x, \hat{x}; \nu)}{\sqrt{\bar{I}_o}} & \text{(Photon-noise-limit)} \end{cases} . \tag{7.12}$$

This result imply that SNR in the detector-noise-limit is proportional to the cross-spectral density across the source plane and that in the photon-noise-limit is proportional to the square root of the cross-spectral density (because $\bar{I}_o$ is proportional to $W^{(z_s)}$). In addition, it should be noted that SNRs in both cases are independent of the number of the sampling points M and N that may be determined by the number of CCD pixels.

7.3 Experiments

To verify the theoretical evaluation derived in the previous section, a simple experiment was conducted. The experimental setup is shown in Fig. 7.2. The fundamental structure was stated in the previous section. A Halogen lamp (HAYASHI WATCH-WORKS, LA-150 SAE) was used as a primary source. A single slit whose width is 0.6 mm masked the output light of the Halogen lamp, and this works as a secondary source. The distance between the observation plane (the mirror surface) and the source plane (the slit) is 155 mm. The spectrum of the superposed light from the wavefront folding interferometer becomes quasi-monochromatic after passing through the interference filter with the spectral bandwidth (FWHM) of 10 nm. The interference fringe is measured by the CCD camera (SONY, XC-73) that is linked to a flame grabber (CYBERTEK, CT-3000A) on a personal computer. Ten images are taken at every step of the positioning stage (MELLES GRIOT, NANOMOVER) for calculating the variances and SNR. Remember that $\hat{x}$ is varied by moving the source fixed on the positioning stage instead of the entire interferometer as explained in Chapter 4. In this experiment, the number of steps for $\hat{x}$ was 512. Consequently, 512×10 flames were taken while the stage moves 2.4 mm, and each image was saved as 8 bit data on the computer. A sample of the image taken by the CCD camera is shown in Fig. 7.3. The horizontal axis denotes Δx and the vertical axis denotes the y axis. The intensity drops suddenly at $\Delta x = 0$ owing to the edge of the right-angled prism. This drop was corrected by using the interference fringe which is measured in the same way for a point source. From the images taken for all $\hat{x}$'s, the cross-spectral density across the observation plane is obtained as shown in Figs. 7.4 (a) and (b). Figure 7.4 (a) represents the real part and (b) the imaginary part. The cross section on the straight line of $\Delta x = 0$ in Fig. 7.4 (a) means the intensity distribution across the observation plane. Applying the inverse propagation law of the cross-spectral density with $z_s = 155$ mm gives the cross-spectral density across the source plane as in Figs. 7.4 (c)

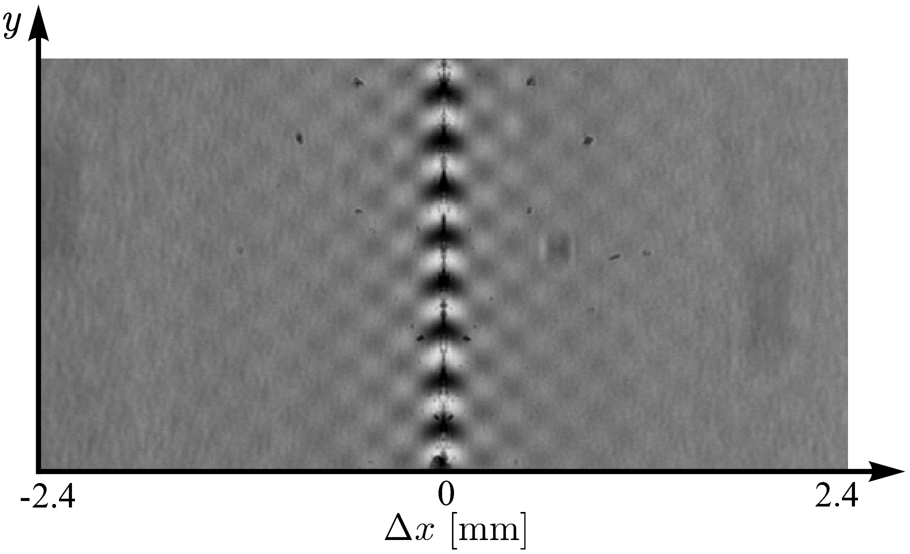

Fig. 7.3. Sample of the interference fringe obtained on the CCD camera.

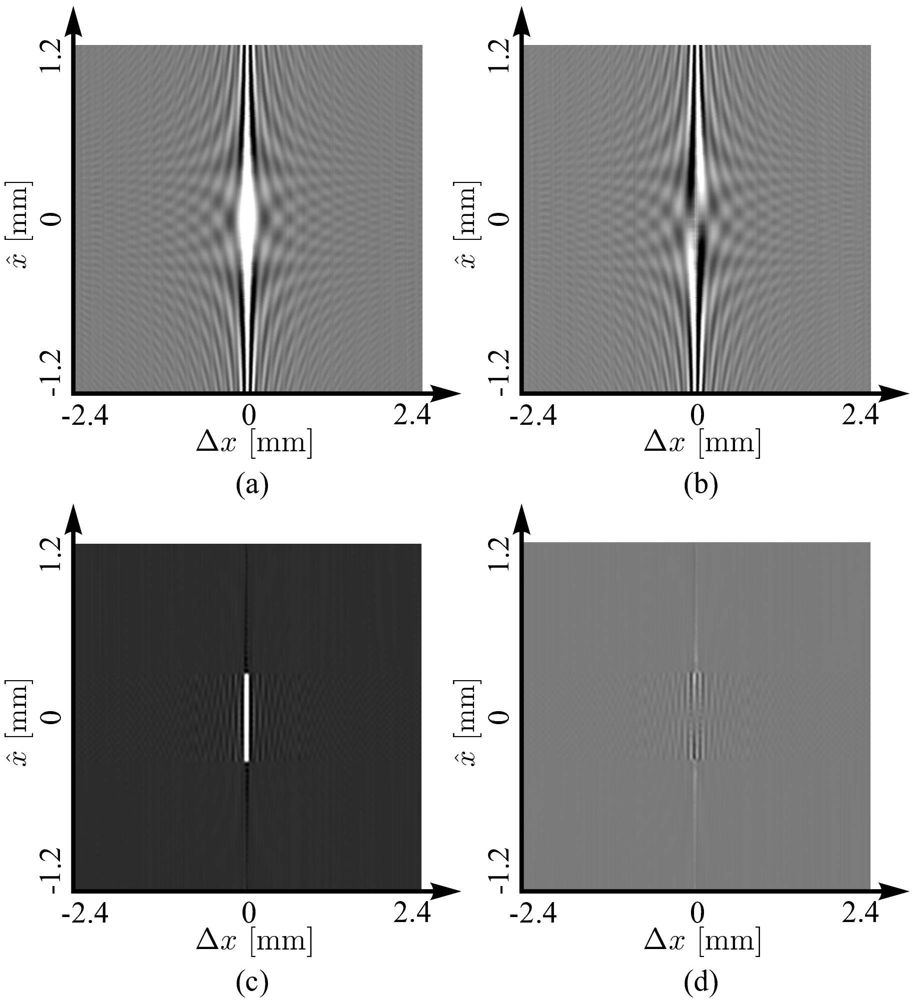

Fig. 7.4. Measured (a) real and (b) imaginary parts of the cross-spectral density across the observation plane. Retrieved (c) real and (d) imaginary of the cross-spectral density across the source plane.

and (d). Figures 7.4 (c) and (d) also show the real and imaginary parts respectively. The cross section at $\Delta x = 0$ of the real part represents the intensity distribution across the source plane, namely, the rectangular profile resulting from the slit. In contrast, narrowness of the horizontal cross section of the real part implies the spatial incoherence of the source fields.

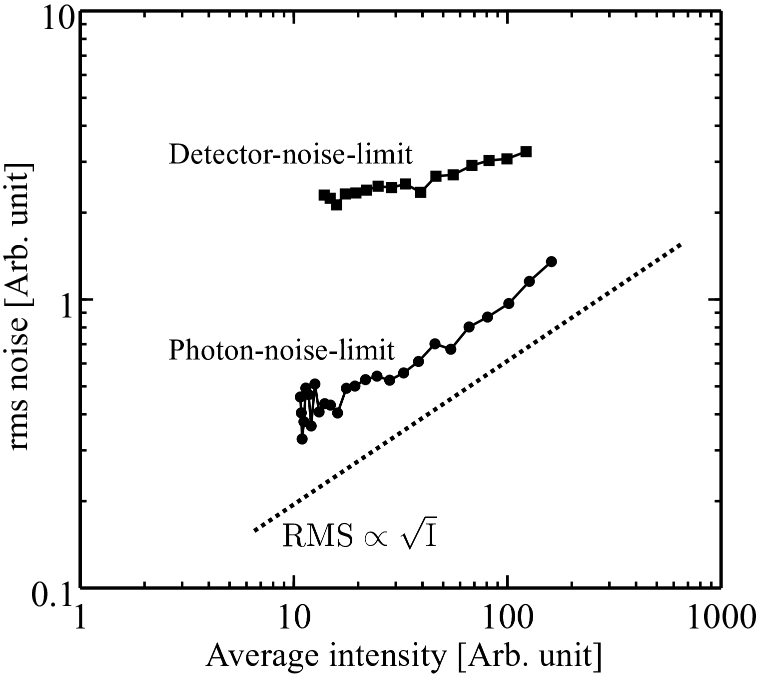

Fig. 7.5. Standard deviation versus the pixel value of the CCD camera used in the experiment.

The two limiting cases were realized by tuning the manual gain control of the CCD camera. The gain level of the CCD camera used in this experiment can be tuned from 0 dB to 18 dB. The relationship between the rms noise and the average intensity over the CCD camera was investigated, and the result is shown in Fig. 7.5. The circular dots represent the rms noise with the gain level of 0 dB and the square dots represent the rms noise with the gain level of 18 dB. The linear line with small dots expresses the inclination of rms $\propto$ average intensity. From this result, it can be seen that the photon-noise is dominant when the gain level is set to 0 dB and that the detector-noise is dominant at the gain level of 18 dB.

To evaluate the dependence of SNR on the cross-spectral density across the source plane, source images for two levels of the source intensity were retrieved. The average

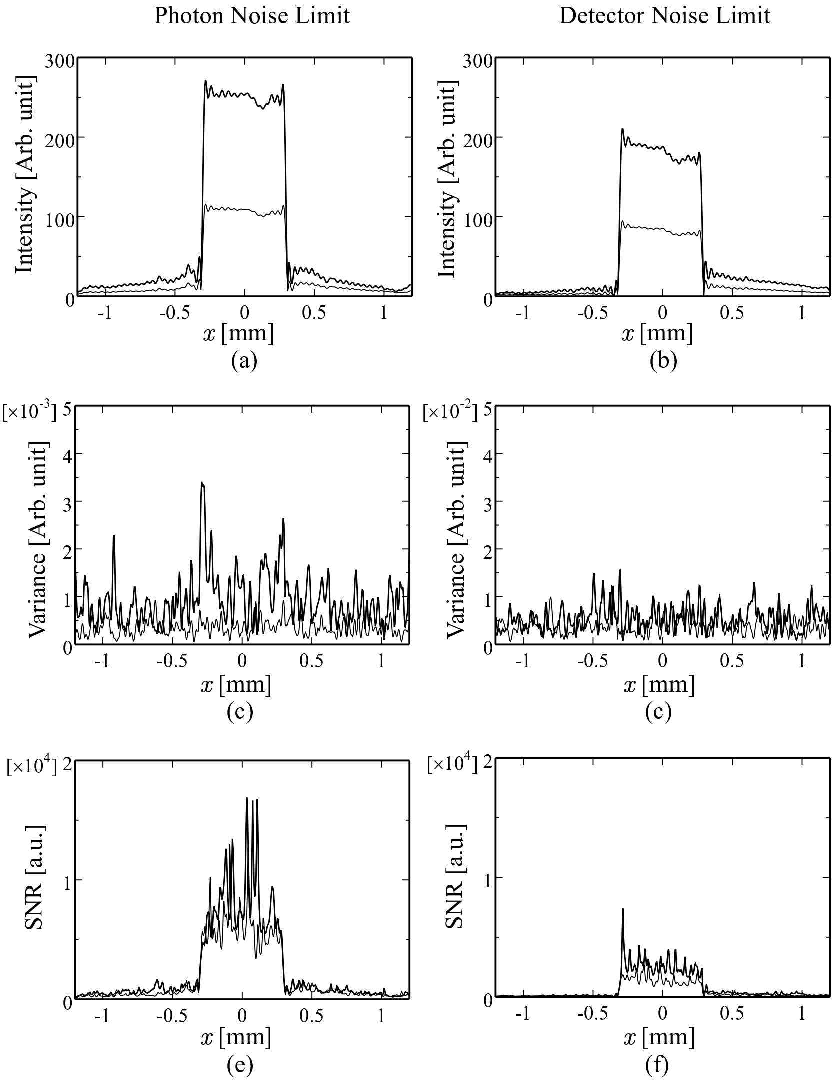

Fig. 7.6. (a)(b) Ensemble averages of the retrieved source intensity distributions. (c)(d) Variances of the retrieved intensity distributions. (e)(f) SNRs of retrieved images. Left side and right side are in the case of photon-noise-limit and detector-noise-limit respectively.

of 10 retrieved intensity distribution across the source plane, the variance, and SNR for two noise limiting cases were calculated for each of the two levels of the source intensity. The results are shown in Figs. 7.6 (a)-(f). Figure 7.6 (a) is the averaged intensity distribution for the photon-noise-limiting case. Two levels of the source intensity are plotted by a bold and a thin lines respectively. The rugged structures appeared in the top of the intensity profiles reflect the nonuniformity of the intensity distribution over the end of fiber bandle linked to the Halogen lamp. The average intensities within the slit region ($-0.3 \leq x \leq 0.3$) are 250 and 107, respectively. Figure 7.6 (b) is, on the other hand, the averaged intensity distribution for the detector-noise-limiting case. The averages over the slit region are 184 and 84, respectively. Figures 7.6 (c) and (d) are the variances of retrieved intensity distributions for two noise limiting cases. The averages of the variances plotted in Fig. 7.6 are 9.27×10^{-4} and 3.53×10^{-4}, and their ratio is 2.63. This ratio is approximately close to the intensity ratio of 2.34 as expected from Eq. (7.11). In contrast, the difference of the variances for the detector-noise-limiting case plotted in Fig. 7.6 (d) is small compared to that of in Fig. 7.6 (c). The averages are 5.43×10^{-3} and 3.87^{-3}, and their ratio is 1.40. Figures 7.6 (e) and (f) represent SNRs. The averages of SNRs in the photon-noise-limiting case are, respectively, 8,047 and 6,010, and their ratio is 1.34. This value is also close to the theoretical expectation $\sqrt{2.34} = 1.53$. In the detector-noise-limiting case of Fig. 7.6 (f), the averages of SNRs are 2,678 and 1,477, and their ratio is 1.81 while the theoretically expected value is 2.19. Next, dependence of SNRs on the number of sampling points are investigated. According to the theoretical estimation, SNR does not depend on M or N (see Eq. (7.12)). In the above calculation, M and N are both 512. By using the same sampling interval, SNR was calculated with $M = N = 256$, namely, regions of Δx and $\hat{x}$ were reduced to half. The measured cross-spectral density that corresponds to the higher intensity in Fig. 7.6 (a) was truncated, and SNR was calculated. SNR with $M = N = 512$, average of SNR over the source region was 8,047 as stated above, and average of SNR with $M = N = 256$ was 7,989. This result clearly verify the independence of SNR from the number of sampling points.

From these experimental results, it can be concluded that the theoretical estimation derived in the previous section is reasonable. Differences between the theoretical values and the experimental values that are seen especially in the detector-noise-limiting case may be owing to the slight dependence of the rms noise of the CCD camera on the input optical intensity as seen from Fig. 7.5. This means that the gain level of 18 dB of the CCD camera used in the experiment makes the detector-noise almost dominant but there still is a small influence of the photon-noise.

7.4 Conclusion

The SNRs of the coherence imaging system based on the wavefront folding interferometer were studied. The theoretically estimated SNRs in the two limiting cases, the photon-noise-limit and the detector-noise-limit, were compared with the experimental results. In the photon-noise-limiting case, the variance of the measured image was mainly determined by the average intensity over the CCD camera and, in contrast, that in the detector-noise-limiting case was constant. In both cases, SNRs was independent of the number of sampling points. Experimental demonstrations were conducted by using the single slit that worked as the source and the wavefront folding interferometer. Ten sets of the data were measured under the same condition and the statistics of the retrieved images were computed. Experimental results almost agreed with the theoretical expectations, and the theoretical estimated SNRs were confirmed.

Chapter 8

Concluding remarks

In this dissertation, novel theoretical analyses and experimental results about the propagation of spatial coherence function and new principles of interferometric imaging techniques are proposed. Followings are the summaries presented in the sequence of chapters:

In Chapter 1, the background of this dissertation was stated. The history of studies on the spatial coherence, the correlation-induced spectral changes, and the interferometric imaging techniques were briefly reviewed.

In Chapter 2, the fundamental concepts of the spatial coherence function described in both the space-time domain and the space-frequency domain were reviewed. The introduction to the correlation-induced spectral changes and the propagation of the spatial coherence function was also given.

In Chapter 3, the correlation-induced spectral changes were studied theoretically and experimentally. The spectral changes in a Gaussian-like spectrum caused by the effects of spatial coherence and dispersive diffraction were investigated. It was shown that the spectral changes depend on the ratio of the coherence area A_c to the area $\pi\rho^2$ of a circular aperture in the secondary source plane. The measured results were in good agreement with the numerical results. The correlation-induced spectral changes that are caused by only the source correlation were also studied. The two point sources with the wide spectral bandwidth realized the variety of the spectral degree of coherence across the secondary source plane. The change in spectrum was observed by the wavefront folding image-forming system. It was verified quantitatively that the peak frequency of the observed spectrum changed toward higher or lower depending on the spectral degree of coherence across the secondary source plane and the observing location.

In Chapter 4, new interferometric imaging techniques for two-dimensional intensity distribution were presented. One enables us to determine the angular separation of two point sources and each spectral profile. A simple simulation experiment was conducted by incorporating two point sources with different spectra, and the experimental results verified the validity of the theoretical prediction. The other was a technique for retrieving the cross-spectral density propagating in free space across an arbitrary plane. Theoretical descriptions are based on the propagation law of the cross-spectral density described in the spatial-frequency domain. Results of an experiment demonstrating retrieval of the cross-spectral density across an arbitrary reference plane were also presented. The cross-spectral density in the observation area was measured by use of a wavefront folding interferometer, and the retrieved cross-spectral densities and the intensity distribution agreed well with the theoretical expectations.

In Chapter 5, a novel technique of interferometric 3-D imaging based on retrieving the sequential cross-spectral densities was presented. The cross-spectral density across an arbitrary transverse plane can be retrieved by using the propagation law described in the spatial-frequency domain in a same manner as that described in Chapter 4.

The 3-D intensity distribution was reconstructed from a sequence of the cross-spectral densities across planes within the slab geometry. Results of an experiment conducted by incorporating two point sources were also presented. The point spread function of the presented interferometric imaging system and its similarity to an ordinary imaging system were discussed. To detect spatially incoherent sources, a novel incoherence gating method based on the present interferometric imaging technique was presented. The differential of the sequence of retrieved cross-spectral densities with respect to a two-point separation enabled us to estimate field correlations over the 3-D field, and the incoherent primary sources were clearly detected at the original positions.

In Chapter 6, another novel 3-D imaging technique that reduces the computational load was proposed. The images are obtained as spatial distributions of Walther's first or second definitions of the generalized radiance function for a particular angular component. The generalized radiance function could be retrieved from the cross-spectral density measured across an observation plane using a propagation law. It was shown that the longitudinal resolution of the second generalized radiance function was much higher than that of the first definition. The second generalized radiance function was thus useful for the 3-D imaging. Results of experimental demonstrations conducted by incorporating uncorrelated two point sources were also reported.

In Chapter 7, noise-limitations of the interferometric imaging system based on the wavefront folding interferometer were studied. The signal-to-noise ratio in the two kinds of noise-limiting cases, namely the photon-noise-limit and the detector-noise-limit, were derived and compared with the experimental results. The experiment was conducted by using the wavefront folding interferometer and a single slit that formed the light source. An ensemble of ten sets of the data were measured under the same condition and the statistics of the noise components were evaluated. It was verified that the experimental results almost agree with the theoretical expectations.

As is summarized here, several important knowledges and solutions concerned with the correlation-induced spectral changes and the interferometric imaging techniques were obtained in this work. However, we still have some problems. Regarding the correlation-induced spectral changes, investigations that takes the real source correlation into account will be necessary for establishing the reliability of the practical astronomical observations. Future developments in both astrophysics and measurement techniques may solve this problem. In respect of the interferometric 3-D imaging, there are still many possibilities for the further advancement. One of possible advancement may be simplification or reduction of the required measurements. Some new principles for 3-D imaging presented in this dissertation need the measurement of the cross-spectral density with respect to all pairs of points in the observation area. In principle, the four-dimensional Fourier transform must be taken in the procedure to retrieve the 3-D image. The procedure of 3-D imaging by retrieving the generalized radiance function is much faster than that of retrieving the sequential cross-spectral densities. However, measurement in real time is still quite difficult, because this technique require four-dimensional data for retrieving the 3-D information of the source. The establishment of the reliable optical arrangement for measure the four-dimensional cross-spectral density may be one solution of this problem. The advancement in hardware and software that make the FFT-based-algorithm to be performed much faster is also expected.

Acknowledgments

I am grateful to Professor K. Itoh at Graduate School of Engineering, Osaka University, for his invaluable guidance and continuous encouragement through the present work, for his giving me the chance to work in this stimulating and excellent place. I would like to express my sincere appreciations to Professor Y. Ichioka, Professor N. Kawakami, Professor M. Hangyo, Professor Y. Takai and Associate Professor Z. Sekkat for their valuable suggestions and comments on this dissertation. I am also grateful to Dr. W. Watanabe for his helpful and supportive advice in my daily works. My sincere appreciation is extended to Dr. K. Yoshimori at Earth Observation Research Center, National Space Development Agency of Japan for his invaluable encouragement, suggestions, and many constructive discussions. My hearty thanks are also extended to Dr. Y. Ohtsuka at Moritex Co., Ltd. for his invaluable guidance and encouragement at the early part of the series of my works. My sincere appreciation is also extended to Associate Professor K. Oka at Faculty of Engineering, Hokkaido University and Dr. S. Tanaka at Department of Communication Engineering, National Defense Academy for their helpful guidance and discussions. Thanks are due to many staffs, my colleagues and friends for their kind supports and encouragements through this work.

References

[1] L. Mandel and E. Wolf, *Optical Coherence and Quantum Optics* (Cambridge University Press, New York, 1995).

[2] L. Mandel and E. Wolf, "Spectral coherence and the concept of cross-spectral purity," J. Opt. Soc. Am. **66,** 529–535 (1976).

[3] E. Wolf, "Invariance of spectrum of light on propagation," Phys. Rev. Lett. **56,** 1370–1372 (1986).

[4] P. W. Milonni and S. Singh, *Source correlations and optical spectra* (Academic Press, New York, 1991), Vol. 28, Chap. 8, pp. 127–137.

[5] E. Wolf, *Influence of source-correlations on spectra of radiated fields* (Academic Press, New York, 1991), pp. 221–232.

[6] H. C. Kandpal, J. S. Vaishya, and K. C. Joshi, "Wolf effect and spectroradiometry," Technical report, The National Physical Laboratory, New Delhi (India) (1990) .

[7] in *Some recent research on optical coherence*, Proc. Symp. Huygens's Principle 1690-1990, H. Blok, H. A. Ferwerda, and H. K. Kuiken, eds., (Noth Holland, Amsterdam, 1992), pp. 113–127.

[8] E. Wolf, *Towards spectroscopy of partially coherent sources* (Plenum, New York, 1993), pp. 369–382.

[9] H. C. Kandpal, J. S. Vaishya, and K. C. Joshi, "Correlation-induced spectral shifts in optical measurements," Opt. Eng. **33,** 1996–2012 (1994).

[10] E. Wolf, “Non-cosmological redshifts of spectral lines,” Nature **326,** 363–365 (1987).

[11] E. Wolf, “Redshifts and blueshifts of spectral lines caused by source correlations,” Opt. Commun. **62,** 12–16 (1987).

[12] E. Wolf, “Red shifts and blue shifts of spectral lines emitted by two correlated sources,” Phys. Rev. Lett. **58,** 2646–2648 (1987).

[13] Z. Dacic and E. Wolf, “Changes in the spectrum of a partially coherent light beam propagation in free space,” J. Opt. Soc. Am. A **5,** 1118–1126 (1988).

[14] A. Gamliel and E. Wolf, “Spectral modulation by control of source correlations,” Opt. Commun. **65,** 91–96 (1988).

[15] J. T. Foley and E. Wolf, “Partially coherent sources which generate the same far field spectra as completely incoherent sources,” J. Opt. Soc. Am. A **5,** 1683–1687 (1988).

[16] D. F. V. James and E. Wolf, “A spectral equivalence theorem,” Opt. Commun. **72,** 1–6 (1989).

[17] A. Gamliel and N. George, “Radiated spectrum from two partially correlated dipoles,” J. Opt. Soc. Am. A **6,** 1150–1155 (1989).

[18] A. Gamliel, “Mode analysis of spectral changes in light propagation from sources of any state of coherence,” J. Opt. Soc. Am. A **7,** 1591–1597 (1990).

[19] A. Gamliel and G. P. Agrawal, “Wolf effect in homogeneous and inhomogeneous media,” J. Opt. Soc. Am. A **7,** 2184–2192 (1990).

[20] G. Agrawal and A. Gamliel, “Spectrum of partially coherent light: transmission from near to far zone,” Opt. Commun. **78,** 1–6 (1990).

[21] R. Martinez-Herrero and P. M. Mejias, “Characterization of polychromatic planar sources that generate the same power spectrum,” J. Opt. Soc. Am. A **7,** 940–942 (1990).

[22] A. Gamliel and G. Agrawal, “Spectrum-enhanced spreading of partially coherent beams,” Opt. Commun. **78,** 203–207 (1990).

[23] J. T. Foley, “The effect of an aperture on the spectrum of partially coherent light,” Opt. Commun. **75,** 347–352 (1990).

[24] J. T. Foley, “Effect of an aperture on the spectrum of partially coherent light,” J. Opt. Soc. Am. A **8,** 1099–1105 (1991).

[25] E. Wolf and J. R. Fienup, “Change in the spectrum of light arising on propagation through a linear, time-invariant system,” Opt. Commun. **82,** 209–212 (1991).

[26] D. F. V. J. an E. Wolf, “Spectral changes produced in Young’s interference experiment,” Opt. Commun. **81,** 150–154 (1991).

[27] D. F. V. James and E. Wolf, “Determination of field correlations from spectral measurements with application to synthetic aperture imaging,” Radio Science **26,** 1239–1243 (1991).

[28] D. F. V. James and E. Wolf, “Some new aspects of Young’s interference experiment,” Phys. Lett. **157,** 6–10 (1991).

[29] F. Gori, G. L. Marcopoli, and M. Santarsiero, “Spectrum invariance on paraxial propagation,” Opt. Commun. **81,** 123–129 (1991).

[30] E. Wolf, “Two inverse problems in spectroscopy with partially coherent sources and the scaling law,” J. Mod. Opt. **39,** 9–20 (1992).

[31] G. V. Varada and G. S. Agrawal, “Microscopic approach to correlation-induced frequency shifts,” Phys. Rev. A **44,** 7626–7634 (1992).

[32] E. Wolf and A. Gamliel, “Energy conservation with partially coherent sources which induce spectral changes in emitted radiation,” J. Mod. Opt. **39,** 927–940 (1992).

[33] D. F. V. James, “Frequency shifts in spontaneous emission from two interacting atoms,” Phys. Rev. A **47,** 1336–1346 (1993).

[34] K. A. Nugent, “Coherence induced spectral changes and generalized radians,” Opt. Commun. **91,** 13–17 (1992).

[35] M. Dusek, “Changes in the spectrum of radiation arising on propagation in case of spherical symmetry,” Opt. Commun. **95,** 189–191 (1993).

[36] G. Hazak and O. Zahavi, “Behavior of spectral lines and degree of spatial coherence in the presence of refraction,” Phys. Rev. A **46,** 4167–4171 (1992).

[37] G. S. Agrawal and D. F. V. James, “Spectral changes in the Mach Zehnder interferometer,” J. Mod. Opt. **40,** 1431–1436 (1993).

[38] M. Dusek, “Wolf effect in fields of spherical symmetry-energy conservation,” Opt. Commun. **100,** 24–30 (1993).

[39] T. Shirai and T. Asakura, “Spectral changes of light radiated by three-dimensional anisotropic Gaussian Schell-model sources,” Opt. Commun. **105,** 22–28 (1994).

[40] G. V. Varada, “A microscopic approach to Wolf effect,” Recent Developments in Quantum Optics pp. 383–386 (1993).

[41] Y. E. D’yakov, “Diffractive changes in the frequency spectrum of propagating radiation (the Wolf effect),” Quantum Electr. **23,** 931–938 (1993).

[42] M. Dusek, “Spectral properties of stochastic electromagnetic fields with spherical symmetry,” Phys. Rev. E **49,** 1671–1676 (1994).

[43] T. Shirai and T. Asakura, “Spectral modification of partially coherent light passing through a periodic sequences of lenses,” J. Opt. Soc. Am. A **11,** 1141–1149 (1994).

[44] G. Hazak and R. Zamir, “The Wolf effect in spherically symmetric systems,” J. Mod. Opt. **41,** 1653–1657 (1994).

[45] E. Wolf, “Spectral invariance and non-invariance of light generated by partially coherent sources,” Appl. Phys. B **60,** 303–308 (1995).

[46] K. Yoshimori, A. Hirai, T. Inoue, K. Itoh, and Y. Ichioka, “Effects of linear edge on optical imaging,” J. Opt. Soc. Am. A **12,** 981–990 (1995).

[47] T. Shirai and T. Asakura, “Multiple light scattering from spatially random media under the second-order Born approximation,” Opt. Commun. **105,** 22 (1994).

[48] H. Arimoto and Y. Ohtsuka, "Effects of spatial coherence and dispersive diffraction on spectral changes," Opt. Rev. **3,** 501–504 (1996).

[49] G. M. Morris and D. Faklis, "Effects of source correlations on the spectrum of light," Opt. Commun. **62,** 5–11 (1987).

[50] M. F. Bocko, D. H. Douglass, and R. S. Knox, "Observation of frequency shifts of spectral lines due to source correlations," Phys. Rev. Lett. **58,** 2649–2651 (1987).

[51] W. H. Knox and R. S. Knox, "Direct observation of the optical Wolf shift using white-light interferometry," J. Opt. Soc. Am. A **4,** 131 (1987), abstract of postdeadline paper PD21, Annual Meeting of the Optical Society of America (Rochester, NY).

[52] D. Faklis and G. M. Morris, "Spectral shifts produced by source correlations," Opt. Lett. **13,** 4–6 (1988).

[53] F. Gori, G. Guattari, C. Palma, and C. Padovani, "Observation of optical redshifts and blueshifts produced by source correlations," Opt. Commun. **67,** 1–4 (1988).

[54] G. Indebetouw, "Synthesis of polychromatic light source with arbitrary degrees of coherence: some experiments," J. Mod. Opt. **36,** 251–259 (1989).

[55] H. C. Kandpal, J. S. Vaishya, and K. C. Joshi, "Wolf shifts and its application in spectroradiometry," Opt. Commun. **73,** 169–172 (1989).

[56] H. C. Kandpal, J. S. Vaishya, and K. C. Joshi, "Simple experimental arrange-

ment for observing spectral shifts due to source correlation," Phys. Rev. A **41,** 4541–4542 (1990).

[57] H. C. Kandpal, J. S. Vaishya, and K. C. Joshi, "Generation of sharp spectral lines under controlled source correlation," Opt. Commun. **77,** 1–3 (1990).

[58] H. C. Kandpal, J. S. Vaishya, and K. C. Joshi, "Spectral shift due to source correlation for paraxial rays," Opt. Commun. **79,** 270–272 (1990).

[59] H. K. E. Drabe, G. Cnossen, D. A. Wiersma, and H. A. Ferwerda, "Reflection-induced source correlation in spontaneous emission," Phys. Rev. Lett. **65,** 1427–1430 (1990).

[60] D. F. V. James, "Comment on reflection-induced source correlation in spontaneous emission," Phys. Rev. Lett. **66,** 675 (1991).

[61] K. C. Joshi, H. C. Kandpal, and J. S. Vaishya, "Spectral shift due to source correlation in conventional spectroradiometric measurements," Appl. Opt. **30,** 1471–1474 (1991).

[62] H. C. Kandpal, J. S. Vaishya, and K. C. Joshi, "Source correlation and its relevance in optical measurements," Current Science **60,** 152–157 (1991).

[63] H. C. Kandpal, J. S. Vaishya, M. Chander, and K. C. Joshi, "Spectral shift in multimode laser due to source correlation," Opt. Commun. **87,** 147–149 (1992).

[64] D. Faklis and G. M. Morris, "Generation of a class of partially coherent sources with controlled correlation," J. Mod. Opt. **39,** 941–948 (1992).

[65] H. C. Kandpal, J. S. Vaishya, and K. C. Joshi, "Changes in the spectra of radiated field as influenced by source correlation," Phys. News. **21,** 86–88 (1990).

[66] A. W. Lohmann, D. Mendlovic, and G. Shabtay, “Coherence waves,” J. Opt. Soc. Am. A **16,** 359–363 (1999).

[67] D. Mendlovic, G. Shabtay, and A. W. Lohmann, “Synthesis of spatial coherence,” Opt. Lett. **24,** 361–363 (1999).

[68] D. Mendlovic, G. Shabtay, and A. W. Lohmann, “Display of spatial coherence,” Opt. Lett. **23,** 1084–1086 (1998).

[69] M. F. Erden, H. M. Ozaktas, and D. Mendlovic, “Propagation of mutual intensity expressed in terms of the fractional Fourier transform,” J. Opt. Soc. Am. A **13,** 1068–1071 (1996).

[70] F. Roddier, “Interferometric imaging in optical astronomy,” Phys. Rep. **170,** 92–166 (1988).

[71] D. F. V. James, H. C. Kandpal, and E. Wolf, “A new method for determining the angular separation of double stars,” Astrophys. J. **445,** 406–410 (1995).

[72] H. C. Kandpal, J. S. Vaishya, K. Saxena, D. S. Mehta, and K. C. Joshi, “Intensity distribution across a source from spectral measurements,” J. Mod. Opt. **42,** 455–464 (1995).

[73] J. Rosen and A. Yariv, “Three-dimensional imaging of random radiation sources,” Opt. Lett. **21,** 1011–1013 (1996).

[74] J. Rosen and A. Yariv, “General theorem of spatial coherence: application to three-dimensional imaging,” J. Opt. Soc. Am. A **13,** 2091–2095 (1996).

[75] J. Rosen and A. Yariv, “Reconstruction of longitudinal distributed incoherent sources,” Opt. Lett. **21,** 1803–1805 (1996).

[76] D. L. Marks, R. A. Stack, and D. J. Brady, “Three-dimensional coherence imaging in the Fresnel domain,” Appl. Opt. **38,** 1332–1342 (1999).

[77] Y. Ohtsuka, “Is the Van Cittert-Zernike theorem applicable to spatially incoherent spectral source?,” Opt. Rev. (to be published 1998).

[78] R. G. Littlejohn and R. Winston, “Correction to classical radiometry,” J. Opt. Soc. Am. A **10,** 2024–2037 (1993).

[79] K. Yoshimori and K. Itoh, “Interferometry and radiometry,” J. Opt. Soc. Am. A **14,** 3379–3387 (1997).

[80] E. Wolf, T. Shirai, H. Chen, and W. Wang, “Coherence filters and their uses,” J. Mod. Opt. **44,** 1345–1353 (1997).

[81] H. Arimoto and Y. Ohtsuka, “Measurements of the complex degree of spectral coherence by use of a wave-front-folded interferometer,” Opt. Lett. **22,** 958–960 (1997).

[82] J. W. Goodman, *Statistical Optics* (John Wiley & Sons, New York, 1985).

[83] Y. Ohtsuka, “Spectrum invariance for a particular class of optical fields propagated in far zone,” Opt. Rev. **2,** 347–351 (1995).

[84] J. W. Goodman, *Introduction to Fourier Optics* (MacGraw-Hill, New York, 1968).

[85] I. J. LaHaie, “Inverse source problem for three-dimensional partially coherent sources and fields,” J. Opt. Soc. Am. A **2,** 35–42 (1985).

[86] E. Wolf and H. W. Carter, "Coherence and radiant intensity in scalar wave fields generated by fluctuating primary planar sources," J. Opt. Soc. Am. **68,** 953–964 (1978).

[87] H. Arimoto, K. Yoshimori, and K. Itoh, "Retrieval of cross-spectral density propagating in free space," J. Opt. Soc. Am. A **16,** 2447–2452 (1999).

[88] H. Arimoto, K. Yoshimori, and K. Itoh, "Interferometric 3-D imaging and incoherence gating," Opt. Commun. **170,** 319–329 (1999).

[89] *Summary of Research*, *SPIE Milestone Series, MS69*, A. Friberg and B. Thompson, eds., (SPIE, Washington, 1993), pp. xv–xxxi.

[90] E. W. Marchand and E. Wolf, "Angular correlation and the far-zone behavior of partially coherent fields," J. Opt. Soc. Am. **62,** 379–385 (1972).

[91] E. W. Marchand and E. Wolf, "Generalized radiometry for radiation from partially coherent sources," Opt. Commun. **6,** 305–308 (1972).

[92] E. W. Marchand and E. Wolf, "Walther's definitions of generalized radiance," J. Opt. Soc. Am. **64,** 1273–1274 (1974).

[93] A. Walther, "Reply to Marchand and Wolf," J. Opt. Soc. Am. **64,** 1275 (1974).

[94] R. L. Fante, "Relationship between radiative-transport theory and Maxwell's equations in dielectric media," J. Opt. Soc. Am. **71,** 460–468 (1981).

[95] H. M. Pedersen, "Geometrical theoryof fields radiated from three-dimensional, quasi-homogeneous sources," J. Opt. Soc. Am. A **9,** 1626–1632 (1992).

[96] H. M. Pedersen, "Propagation of generalized specific intensity in refracting media," J. Opt. Soc. Am. A **9,** 1623–1625 (1992).

[97] M. S. Zubairy, "Radiative energy transfer in a randomly fluctuating medium," Opt. Commun. **37,** 315–320 (1981).

[98] T. Jannson and R. Janicki, "An eigenvalue formulation of inverse theory of scalar diffraction," Optik **56,** 429–441 (1980).

[99] T. Jannson, "Radiance transfer function," J. Opt. Soc. Am. **70,** 1544–1549 (1980).

[100] M. J. Bastiaans, "The Wigner distribution function applied to optical signals and systems," Opt. Commun. **25,** 26–30 (1978).

[101] G. S. Agarwal, J. T. Foley, and E. Wolf, "The radiance and phase-space representations of the corss-spectral density operator," Opt. Commun. **62,** 67–72 (1987).

[102] H. W. Carter and E. Wolf, "Coherence and radiometry with quasihomogeneous planar sources," J. Opt. Soc. Am. **31,** 785–796 (1977).

[103] J. T. Foley and E. Wolf, "Radiometry as a short-wavelength limit of statistical wave theory with globally incoherent sources," Opt. Commun. **55,** 236–241 (1985).

[104] M. N. Vesperinas, "Classical radiometry and radiative transfer theory: a short-wavelength limit of a general mapping of cross-spectral densities in second-order coherence theory," J. Opt. Soc. Am. A **3,** 1354–1359 (1986).

[105] A. Walther, “Radiometry and coherence,” J. Opt. Soc. Am. **58,** 1256–1259 (1968).

[106] A. Walther, “Radiometry and coherence,” J. Opt. Soc. Am. **63,** 1622–1623 (1973).

[107] A. Hirai, M. Hashimoto, K. Itoh, and Y. Ichioka, “Multichannel spectral imaging system for measurements with the highest signal-to-noise ratio,” Opt. Rev. **4,** 334–341 (1997).

[108] T. Inoue, K. Itoh, and Y. Ichioka, “Signal-to-noise ratios of Fourier-transform spectral-imaging in the image plane and pupil plane,” Optik **98,** 175–180 (1995).

List of Publications

[1] H. Arimoto and Y. Ohtsuka, "Effects of spatial coherence and dispersive diffraction on spectral changes," Opt. Rev. **3,** 501–504 (1996).

[2] H. Arimoto and Y. Ohtsuka, "Measurements of the complex degree of spectral coherence by use of a wave-front-folded interferometer," Opt. Lett. **22,** 958–960 (1997).

[3] H. Arimoto and Y. Ohtsuka, "Complex degree of spectral coherence and spectral changes measured by two-beam interference experiments in the space-frequency domain," J. Opt. Soc. Am. A **15,** 914–923 (1997).

[4] H. Arimoto and Y. Ohtsuka, "Determination of the angular separation and the spectra of two-point sources from spectral coherence measurements," Opt. Lett. **23,** 724–726 (1998).

[5] H. Arimoto and Y. Ohtsuka, "Angular separation and spectral of two point sources determined from measured spectral coherence," Pure Appl. Opt **7,** 971–979 (1998).

[6] H. Arimoto, K. Yoshimori, and K. Itoh, "Retrieval of cross-spectral density propagating in free space," J. Opt. Soc. Am. A **16,** 2447–2452 (1999).

[7] H. Arimoto, K. Yoshimori, and K. Itoh, "Interferometric 3-D imaging and incoherence gating," Opt. Commun. **170,** 319–329 (1999).

[8] H. Arimoto, K. Yoshimori, and K. Itoh, "Interferometric Three-Dimensional imaging based on retrieval of generalized radiance distribution," Opt. Rev. **7,** in press (2000).

[9] H. Arimoto, K. Yoshimori, and K. Itoh, “Noise limitations of coherence imaging based on the wavefront folding interferometry,” Opt. Rev. submitted.

List of Proceedings of International Conferences

[1] H. Arimoto, S. Tanaka, and Y. Ohtsuka, “Dependence of spectrum changes on the ratio of coherence area to source area,” in *Optics for Science and New Technology*, J. -S. Chang, J. -H. Lee, S. -Y. Lee, and C. H. Nam eds., Proc. SPIE, **2778,** 349–350 (1996).

[2] H. Arimoto and K. Itoh, “Passive interferometric 3D imaging on the basis of a propagation law of the cross-spectral density,” in *Optical Engineering for Science and Nanotechnology*, I. Yamaguchi ed., Proc. SPIE, **3740,** 622–625 (1999).

[3] H. Arimoto and K. Itoh, “Propagation of angular cross-spectral density and 3D imaging, (*invited paper*)” *The International Symposium on Optical Science, Engineering, and Instrumentation*, B. Javidi and D. Psaltis eds., Proc. SPIE, **3804,** 51–59 (1999).

[4] H. Arimoto and K. Itoh, “Interferometric imaging by inverse propagation of cross-spectral density,” in *Optics for the Next Millennium*, Proc. SPIE, **3749,** 134–135 (1999).